Applied Computational Electromagnetics Society

Journal

June 2011 Vol. 26 No. 6

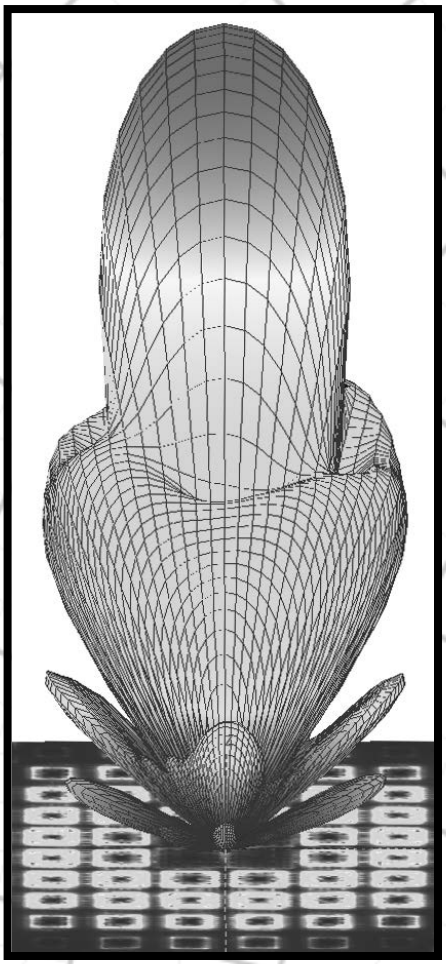

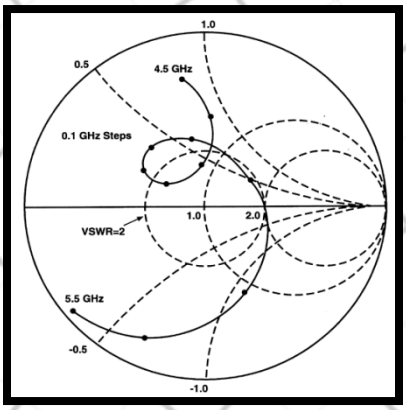

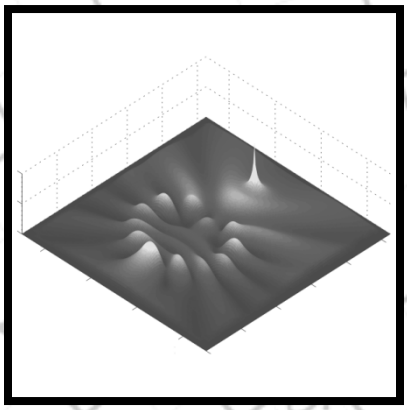

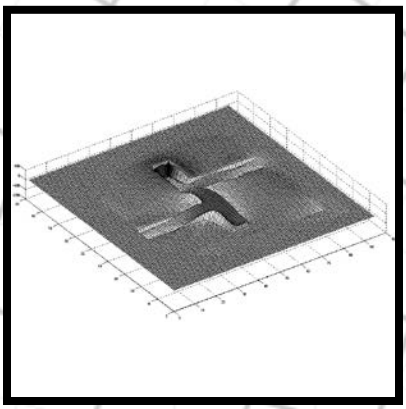

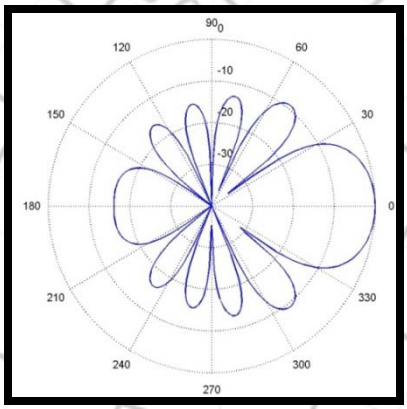

ISSN 1054-4887

GENERAL PURPOSE AND SCOPE: The Applied Computational Electromagnetics Society ***(ACES)*** Journal hereinafter known as the ***ACES Journal*** is devoted to the exchange of information in computational electromagnetics, to the advancement of the state-of-the art, and the promotion of related technical activities. The primary objective of the information exchange is to inform the scientific community on the developments of new computational electromagnetics tools and their use in electrical engineering, physics, or related areas. The technical activities promoted by this publication include code validation, performance analysis, and input/output standardization; code or technique optimization and error minimization; innovations in solution technique or in data input/output; identification of new applications for electromagnetics modeling codes and techniques; integration of computational electromagnetics techniques with new computer architectures; and correlation of computational parameters with physical mechanisms.

SUBMISSIONS: The ***ACES Journal*** welcomes original, previously unpublished papers, relating to applied computational electromagnetics. Typical papers will represent the computational electromagnetics aspects of research in electrical engineering, physics, or related disciplines. However, papers which represent research in applied computational electromagnetics itself are equally acceptable.

Manuscripts are to be submitted through the upload system of ***ACES*** web site http://aces.ee.olemiss.edu See "Information for Authors" on inside of back cover and at ***ACES*** web site. For additional information contact the Editor-in-Chief:

Dr. Atef Elsherbeni
Department of Electrical Engineering
The University of Mississippi
University, MS 386377 USA
Phone: 662-915-5382
Email: atef@olemiss.edu

SUBSCRIPTIONS: All members of the Applied Computational Electromagnetics Society are entitled to access and download the ***ACES Journal*** any published journal article available at http://aces.ee.olemiss.edu. Printed issues of the ***ACES Journal*** are delivered to institutional members. Each author of published papers receives a printed issue of the ***ACES Journal*** in which the paper is published.

Back issues, when available, are $50 each. Subscription to ***ACES*** is through the web site. Orders for back issues of the ***ACES Journal*** and change of address requests should be sent directly to ***ACES*** office at:

Department of Electrical Engineering
The University of Mississippi
University, MS 386377 USA
Phone: 662-915-7231
Email: aglisson@olemiss.edu

Allow four weeks advance notice for change of address. Claims for missing issues will not be honored because of insufficient notice, or address change, or loss in the mail unless the ***ACES*** office is notified within 60 days for USA and Canadian subscribers, or 90 days for subscribers in other countries, from the last day of the month of publication. For information regarding reprints of individual papers or other materials, see "Information for Authors".

LIABILITY. Neither ***ACES***, nor the ***ACES Journal*** editors, are responsible for any consequence of misinformation or claims, express or implied, in any published material in an ***ACES Journal*** issue. This also applies to advertising, for which only camera-ready copies are accepted. Authors are responsible for information contained in their papers. If any material submitted for publication includes material which has already been published elsewhere, it is the author's responsibility to obtain written permission to reproduce such material.

APPLIED COMPUTATIONAL ELECTROMAGNETICS SOCIETY JOURNAL

June 2011
Vol. 26 No. 6
ISSN 1054-4887

The ACES Journal is abstracted in INSPEC, in Engineering Index, DTIC, Science Citation Index Expanded, the Research Alert, and to Current Contents/Engineering, Computing & Technology.

The illustrations on the front cover have been obtained from the research groups at the Department of Electrical Engineering, The University of Mississippi.

JUNE 2011 REVIEWERS

Ahmed Abdelrahman
Guido Ala
Rodolfo Araneo
Mohamed Bakr
Jian Bao
Hamid Reza Behjoo
Jiefu Chen
Michael Chryssomallis
Nicolas Cinosi
Jorge Costa
Said El-Khamy
Khaled ElMahgoub
Naftali Herscovici
Julie Huffman
Darko Kajfez
Haider Khaleel
Jafar Khalilpour
Rakhesh Singh Kshetrimayum
Nathan Ida
Hai Jiang
Fernando Las-Heras
Zhong-Xin Li
Angelo Liseno
Hend Malhat
Chen Ming
Claudio Montiel
Antonino Musolino
Burak Polat
Rui Qiang
Mehdi Salehi
Abhishek Shrivastava
Kathering Siakavara
Jerry Smith
Hossein Torkaman
Christopher Trueman
Chardrasekar Viswam
Rui Wang
Shaoqiu Xiao
Fan Yang
Ozan Yurduseven
Li Zhang

THE APPLIED COMPUTATIONAL ELECTROMAGNETICS SOCIETY

JOURNAL

Vol. 26 No. 6 June 2011

TABLE OF CONTENTS

Miniaturization of Conical Helical Antenna via Optimized Coiling

Tao Peng [1], Stavros Koulouridis [2], and John L. Volakis[1]

[1] ElectroScience Laboratory, Department of Electrical and Computer Engineering
The Ohio State University, Columbus, OH, 43212, U.S.A.
peng.75@osu.edu, volakis.1@osu.edu

[2] Laboratory of Electrotechnics, Department of Electrical & Computer Engineering
University of Patras, Patras, 26500, Greece
koulouridis@ece.upatras.gr

Abstract ─ Conical helices are extensively used in multifunctional antenna platforms for UHF and VHF frequencies because of their broadband characteristics. Therefore, there is strong interest to reduce their size as much as possible. In this paper, a conical helix with metallic ground plane is considered and reduced in size by as much as 30% via coiling (equivalent to inductive loading). The coiling is obtained via genetic algorithms subject to customized criteria for best ultra-wideband realized gain.

Index Terms ─ Antenna optimization, circular polarized antennas, equivalent circuit model, Genetic Algorithm, UWB antenna miniaturization.

I. INTRODUCTION

The benefits of ultra wideband antennas have been increasingly attractive due to their intrinsic capability to integrate multiple communication systems on a single platform. Axial mode conical helix is one of the widely used ultra wideband (UWB) circular polarized antennas for satellite communications. To integrate such an antenna for airborne, ground and sea based systems, its size and weight must be minimized. Otherwise, it can be prohibitively large for low frequency applications and too heavy for airborne systems. In this paper, inductive loadings are used to reduce the antenna aperture size as much as possible with minimal negative impact on the wideband gain. For our applications, it is desired to have total realized gain over -15 dBi at the lowest frequencies, and realized right hand circular polarized (RHCP) gain as high as possible for the ultra-wideband section.

Conical helices backed by a metallic surface are characterized by good directive circular polarized (CP) gain and over 50% bandwidth [1]. We build on the extensive background relating to the axial modes of these antennas [1-[6], with a goal to reduce their size. Specifically, we introduce inductive loading in the form of coiling to slow down wave velocity [7-9] along the helical antenna wires. We note that adding coiling increases the wire length forming the conical helix, leading to miniaturization. However, if not done optimally, antenna gain at higher frequencies would be reduced.

An important aspect of our study is the optimization methodology for the coiling. Coiling can certainly add miniaturization but if it is not optimally applied, it reduces gain and bandwidth. Here, genetic algorithm (GA) optimization [10] is employed to minimize bandwidth degradation. Indeed, GA optimization was applied to different helical antennas using moment method analysis with curved segments in [11]. In this paper, a moment method wire code was also used, namely NEC-Win [12], to carry out the optimization.

Below, we discuss the key geometric parameters of the coiled conical helix and the proposed miniaturization concept. A carefully constructed GA fitness function to generate highly customized wideband CP gain is adopted. Optimization results show a 30% to 40% size reduction, subject to the constraint set. We should note here that all simulations are carried out with

copper wires to take into consideration the resistive loss. One might think that long wiring from coiling would degrade antenna efficiency. However, ohmic loss attributes significantly to the impedance matching at lower frequencies where the small antenna tends to behave more like a resonator. In this case, ohmic loss may benefit antenna realized gain at these low frequencies because better matching from resistive loss can balance or even outweigh the gain loss.

II. ANTENNA GEOMETRY AND PARAMETRIC CHARACTERIZATION

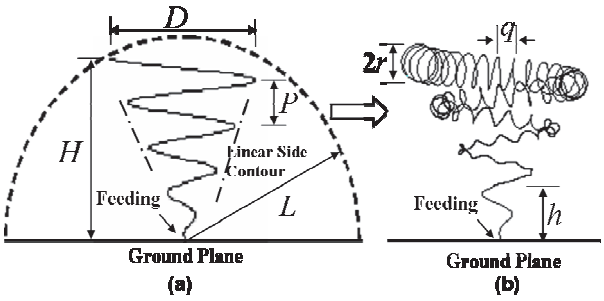

Fig. 1. (a) Geometric parameters of a conical helix antenna. The enclosing sphere of radius L defines the size restrictions for the antenna; (b) details of the coiling.

Our goal, as said, is to minimize antenna size. To do so we need to determine all the optimization parameters that we will deal with. In Fig. 1a, the geometric parameters of the conical helix are given, that is the height H, the step P and helix top diameter D. Additionally, a side contour line (Fig. 1a) determines how the helix diameter changes with the height from the feeding to the end tip of the helical wire (in Fig. 1a side contour line is linear). As for the coiling (see Fig. 1b) parameter h determines at what point from the ground the coiling starts. r and q determine the coil radius and pitch respectively. As it will be explained below, r and q variation along the helical wire is governed by a mathematical relation.

The size of an electrical small antenna is defined by its radian sphere [13], which is a hypothetical sphere whose diameter $2L$ is equal to the largest linear dimension of the antenna that it encloses (see Fig. 1a). We will keep our design restricted in such a sphere. That is, increasing top helix diameter will decrease helix's height and vice versa. The top diameter of the conical helix is limited by the radian sphere: $D = 2\sqrt{L^2 - H^2}$. Larger D leads to higher realized CP gain at lower frequencies in the $\theta = 0°$ direction. However, due to the radian sphere limitations, larger diameter D is translated to reduced antenna height H, and thus, the conical helix is more likely to be shorted by the mirror effects of the ground plane. Given this set of tradeoff, the optimal H is left for the optimizer to decide.

Another degree of freedom is the side conical contour line of the conical helix. In Fig. 1, the diameter of the conical helix increases linearly with the antenna height, so the side contour is linear. We can expand the potential antenna configurations by varying the side line of the conical helix (see Fig. 2a). In Fig. 2b, various contour lines are presented. They are divided in concave (upper left half of Fig. 2b) and convex curves (down right half of Fig. 2b). Parameters $\alpha_{1,contour}$ and $\alpha_{2,contour}$ (see Fig. 2) determine the type of concave and convex curve respectively as represented from the following line equations:

$$x^1 = R\left(1 - \alpha_{1,contour} \arctan\left(\left(1 - \frac{z}{H}\right)\tan\frac{1}{\alpha_{1,contour}}\right)\right), \quad (1)$$

$$x^2 = R\left(1 - \tan\left(\left(1 - \frac{z}{H}\right)\frac{1}{\alpha_{2,contour}}\right)/\tan\left(\frac{1}{\alpha_{2,contour}}\right)\right), \quad (2)$$

where x^1 or x^2 determines the helix radius at height z. Also R is the top helix radius (R=D/2).

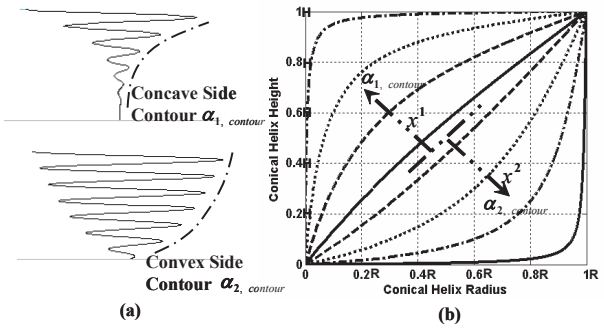

Fig. 2. The variation of helix radius x with increasing height z is defined by its contour line. The contours in the upper left half (concave curves) are determined by $\alpha_{1,contour}$ (eq. (1)); $\alpha_{2,contour}$ (eq. (2)) determines the contours in the down right half (convex curves).

Inductive loading to further slow down wave velocity is the key element for the conical helix miniaturization. Additional inductance will be introduced to the helical antenna by coiling its wire. Actually, under certain conditions, the coiling of the coiled conical helical antenna (coil radius r and coil pitch q, see Fig. 4a), can be considered as a helical waveguide. Under a dense helical coil condition $(2r >> q)$, its characteristic coil axial phase velocity is approximated by Rowe in [14]:

$$v_0 = \frac{1}{\sqrt{L_e C_e}} \approx \frac{cq}{2\pi r}\sqrt{\frac{I_0(\gamma r)K_0(\gamma r)}{I_1(\gamma r)K_1(\gamma r)}}, \quad (3)$$

where γ is the spatial frequency in the coil radial direction, and c is the speed of light. $I_{0,1}$ and $K_{0,1}$ are the zeroth/first order modified Bessel functions of the first and second kind respectively. The dispersion equation of the helical coil waveguide transmission line can be obtained as

$$\gamma^2 = k^2\left(\frac{2\pi r}{q}\right)^2 \frac{I_1(\gamma r)K_1(\gamma r)}{I_0(\gamma r)K_0(\gamma r)}, \quad (4)$$

with $k^2 = \omega^2\mu\varepsilon$. Clearly, the larger the r and the smaller the q, the slower the axial phase velocity v_0 [14] is. As the wave is slowed down more, miniaturization is achieved.

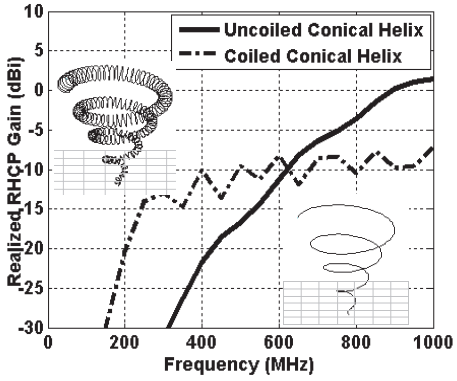

Fig. 3. Coiling should be carried out in an optimum way; otherwise it could severely damage the wideband gain of the conical helix antenna.

The main side effect of lager r and smaller q throughout conical helical wires is the severe gain degradation at higher frequency regions as shown in Fig. 3. This is partly due to the strong resonance caused by large equivalent transmission line inductance L_e and capacitance C_e of the helical coil waveguide. We refer to Rowe [14] here as well:

$$L_e = \frac{2\pi\mu_0 r^2}{q^2} I_1(\gamma r)K_1(\gamma r), \quad (5)$$

$$C_e = \frac{2\pi\varepsilon_0}{I_0(\gamma r)K_0(\gamma r)}. \quad (6)$$

Both L_e and C_e increase almost linearly with the ratio r/q as shown in Fig. 4b and 4c. Excessively large L_e and C_e from high r/q (large r, small q) transforms the conical helix antenna from a radiator into a transmission line at the UWB frequency range, which makes good impedance matching impossible and reduces the realized CP gain significantly. Hence, the proper design of the coiling is the most crucial part in miniaturizing a conical helix antenna as much as possible without reducing the wideband CP gain or degrading the bandwidth.

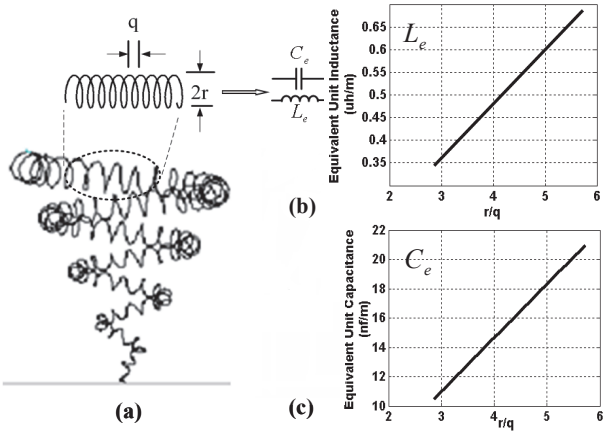

Fig. 4. The equivalent inductance and capacitance of the coiling increase almost linearly with the r/q ratio. Excessively large r and small q can change the conical helix antenna from a radiator to a resonator with large values of equivalent inductance L_e and capacitance C_e (eqs. (5) and (6)).

To keep impedance matching of the loaded coil waveguide well maintained, it is important to slowly increase inductance using, for example, a gradually increasing coil diameter of maximum value $2r$, and a gradually decreasing coil pitch from q_1 at the bottom to q_2 at top. Therefore, we will let the coil starting height h, the maximum coil radius at the top r, the coil pitch at the lower

starting position q_1 and at the top q_2 to be optimized (see Fig. 1b). It is also important to note that the performance of the coiled conical helix is significantly influenced by how the coil radius changes from 0 to r and how the coil pitch varies from q_1 to q_2. Here again, we use the same tapering coefficient formula as the conical helix side contour lines in (1), (2) to characterize the growth of coil radius and the decrease of coil pitch. Note that $t(z)$ is the length of the helical wires from the source at height z and $T = t(H)$ is the total length of the conical helix wire.

$$r^1 = r\left(1 - \alpha_r^1 \arctan\left(\left(1 - \frac{t(z)}{T}\right)\tan\frac{1}{\alpha_r^1}\right)\right),$$

$$r^2 = r\left(1 - \tan\left(\left(1 - \frac{t(z)}{T}\right)\frac{1}{\alpha_r^2}\right)/\tan\left(\frac{1}{\alpha_r^2}\right)\right),$$

$$q^1 = q_1 + (q_2 - q_1)\left(1 - \alpha_q^1 \arctan\left(\frac{T - t(z)}{T - t(h)}\tan\frac{1}{\alpha_q^1}\right)\right),$$

$$q^2 = q_1 + (q_2 - q_1)\left(1 - \tan\left(\frac{T - t(z)}{T - t(h)}\frac{1}{\alpha_q^2}\right)/\tan\left(\frac{1}{\alpha_q^2}\right)\right).$$

Again, α_r^1 or α_r^2 and α_q^1 or α_q^2 correspond to concave (α_r^1, α_q^1) or convex (α_r^2, α_q^2) curves and they allow for considerable coil radius and pitch variations. The coiling along the helical wires at location $t(z)$ has a radius r^1 or r^2, and a pitch q^1 or q^2.

In conclusion, by utilizing various geometric parameters for the helical antenna, we increase our chances of finding the best miniaturized coiled conical helix within the specific radian sphere limitation. The geometrical parameters to optimize are the height H and step P of conical helix, and the side contour line parameter $\alpha_{1,contour}$ or $\alpha_{2,contour}$. Several inductive coiling structures are then modeled by optimizing maximum coil radius at the top r, lower coil pitch q_1, top coil pitch q_2, coil starting height h, coil radius tapering parameter α_r^1 or α_r^2, and coil pitch tapering parameter α_q^1 or α_q^2. These nine optimization variables allow abundant different geometrical configurations of the coiled conical helix with enough flexibility to get optimum antenna directivity, axial ratio and radiation patterns. Further, since impedance matching or VSWR is also very important, especially at lower resonating frequencies, we add the line characteristic impedance as the tenth optimization variable for optimal antenna matching.

III. OBJECTIVE FUNCTION

For optimization, it is critical to choose an accurate problem-descriptive objective function. Such a function should seek the smallest antenna with the largest possible bandwidth and gain. In our design, we are mostly concerned for the -15dBi and 0 dBi gain points, as well as wideband axial ratio. With this in mind, we choose to maximize the following objective function,

$$\begin{aligned} F_{obj}(r,h,q) = \sum_{i=1}^{M} \min\Big\{ & \left[\max(G_i, G_i^{lower}) - G_i^{upper}\right]^3 + \\ & \left[\max\ (G_i, G_i^{lower}) - G_i^{upper}\right],\ 0\Big\}\cdot w_i + \\ \sum_{j=1}^{N} \max\Big\{ & \left[\min(AR_j, AR_j^{upper}) - AR_i^{lower}\right]^3 \\ & + \left[\min(AR_j, AR_j^{upper}) - AR_j^{lower}\right],\ 0\Big\}\cdot w_j^{AR} \end{aligned}$$

The objective function comprises two sum terms and seeks to concurrently increase realized CP gain and decrease axial ratio in the $i = 1,2,3\cdots M$ and j = $1,2,3\cdots N$ frequency regions respectively. w_i and w_j are constants (weights) that are used to regulate the contribution of the different terms.

In the first sum term (CP gain), G_i (to be maximized) is the mean value of 3 frequency samples in the i th region and is evaluated against a pre-specified lower bound G_i^{lower}. The maximum of the two, viz. $\max\left(G_i, G_i^{low}\right)$, is then contrasted with an upper pre-specified bound G_i^{upper}. The idea is to favor values of gain that lie in the $\left(G_i^{lower}, G_i^{upper}\right)$ area. Values that are below G_i^{lower} are penalized with the maximum negative penalty, equal to

$$\left(G_i^{lower} - G_i^{upper}\right)^3 + \left(G_i^{lower} - G_i^{upper}\right).$$

Values of G_i in the $\left(G_i^{lower}, G_i^{upper}\right)$ area result to a varying negative value of

$$\left(G_i - G_i^{upper}\right)^3 + \left(G_i - G_i^{upper}\right).$$

Values over G_i^{upper} are not penalized but do not get either any benefit since they result to a value equal to zero. In that way, very low values of G_i do not de-normalize the objective function. Also, very high values of G_i are unwanted since they can destroy the gain behavior at other frequency regions.

The cubic term $\left[\max\left(G_i, G_i^{low}\right) - G_i^{upper}\right]^3$ and the linear term $\left[\max\left(G_i, G_i^{low}\right) - G_i^{upper}\right]$ are employed to obtain a descriptive measure of the gain performance for the different frequency bands, that is gain differences smaller than unity are mainly controlled from the linear term, whereas gain differences larger than unity are emphasized through the cubic term.

Axial ratio minimization which is controlled from the second sum term of the objective function is carried out through a similar scheme.

IV. RESULTS AND DISCUSSION

The optimizing antenna was enclosed in a sphere with $L = \mathbf{4.5}''$ radius (see Fig. 1). As said, GA optimization was adopted. Details on the GA can be found in [10], [15]. As noted, the height H, pitch P, and the side contour curvature parameter $\alpha_{contour}$ (see Fig. 2) completely describe the shape of the conical helix. The top helix radius is determined from $R = D/\mathbf{2} = \sqrt{L^2 - H^2}$. In genetic algorithm, the height H ranged from $\mathbf{0.8}''$ to $\mathbf{4.3}''$ with 16 possible values in between. The pitch P was set as $H/\mathbf{8} \le P \le H$ with 8 possible values. The side contour parameter of the conical helix ranged $\mathbf{0.64} \le \alpha_{contour} \le \mathbf{1.44}$ with 64 potential curves. There was one extra digit to define whether $\alpha_{\mathbf{1},contour}$ or $\alpha_{\mathbf{2},contour}$ is adopted ($\alpha_{\mathbf{1},contour}$ shows concave curves and $\alpha_{\mathbf{2},contour}$ represents convex curves in Fig. 2b). The coiling configuration was determined by maximum radius r, starting and ending pitches q_1, q_2, the coiling starting height, h, and two tapering parameters α_r and α_q that describe how the coil radius and coil pitch grow from 0 to r and from q_1 to q_2. α_r and α_q were set as $\alpha_{contour}$: $\mathbf{0.64} \le \alpha_r, \alpha_q \le \mathbf{1.44}$ with 64 values and two extra digits to distinguish between α_r^1, α_q^1 and α_r^2, α_q^2 respectively. These two parameters are very crucial to characterize how fast the coil radius grows and coil pitch decreases. For optimization, we specifically allowed r to vary over $\mathbf{0}'' < r < \mathbf{0.8}''$ with 8 potential values and $\mathbf{0.1}'' < q_2 \le q_1 < \mathbf{5}''$ with 64 potential values for each. Also, the coiling starting height variation range was set to $\mathbf{0}'' \le h \le \mathbf{0.8} \times H$ and was allowed to take 8 different values. The matching impedance varied from $\mathbf{50}\Omega$ to $\mathbf{500}\Omega$ with 8 possible values to achieve the optimal matching loss. The resulting GA chromosome had 49 bits length. 50 "individuals" were sufficient to cover the design space. In addition, 70% crossover and 2% mutation rates were employed with elitism and niching adapted within the GA. We note that convergence was typically achieved after 40 to 50 generations.

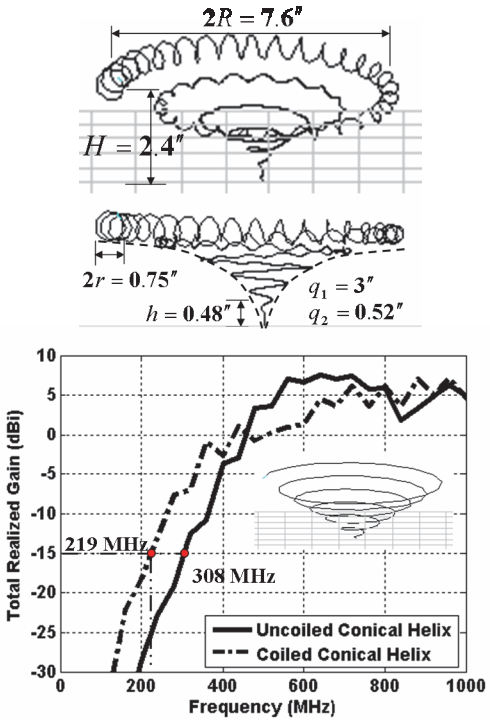

Fig. 5. Optimal coiled conical helix configuration within the $L = \mathbf{4.5}''$ radian sphere. It achieves around 30% miniaturization for the -15 dBi total gain point. ($\alpha_{\mathbf{1},contour} = \mathbf{1.44}$, $\alpha_r^2 = \mathbf{0.69}$, $\alpha_q^2 = \mathbf{0.82}$, $Z = \mathbf{150}\Omega$). The rest of the geometric parameters are given in the figure.

For this work, our goal was to achieve high wideband CP gain with the -15 dBi point as low as

possible without affecting the 0 dBi corresponding frequency. To facilitate this, we also chose an intermediate frequency control point with a target gain of -5dBi. So for the objective function, after an examination of Fig. 3, we chose 230-270MHz, 430-470MHz and 950-990MHz as our 3 frequency bands ($i = 1, 2, 3$). For 230-270MHz (the -15dBi point region), G_1 is calculated from

$$G_1 = \frac{G_{f=230MHz} + G_{f=250MHz} + G_{f=270MHz}}{3},$$

with the corresponding G_i^{lower}, G_i^{upper} values chosen as $G_1^{lower} = -20$ and $G_1^{upper} = -13$. Likewise, for the 430-470MHz band, the gain G_2 is calculated from

$$G_2 = \frac{G_{f=430MHz} + G_{f=450MHz} + G_{f=470MHz}}{3},$$

with $G_2^{lower} = -10$ and $G_2^{upper} = 0$. Finally, for the higher frequency band (the 0dBi gain region), we chose

$$G_3 = \frac{G_{f=950MHz} + G_{f=970MHz} + G_{f=990MHz}}{3},$$

with $G_3^{lower} = -3$ and $G_3^{upper} = 3$. For the axial ratio optimization (second term of the objective function), we chose one band at 950-990MHz. We set

$$AF_1 = \frac{AR_{f=950MHz} + AR_{f=970MHz} + AR_{f=990MHz}}{3}$$

and we chose $AR_1^{upper} = 10$ and $AR_1^{lower} = 1.5$. As also noted in the fitness function, each of the gain "penalty" values is multiplied by a weighting term. For this optimization, since high broadband RHCP gain was of major interest, we set the weight $w_1 = w_2 = 1.2$, $w_3 = 1.5$ and $w_1^{AR} = 1.2$

In Fig. 5, we show the final optimized case and the corresponding realized gain. The optimized coiled helix has its -15 dBi total gain point miniaturized from 308MHz down to 219 MHz implying 30% miniaturization. As seen in Fig. 6, in both UHF and VHF bands, the coiled conical helix has better gain characteristics than the simple conical helix. Also, the axial ratios of the two antennas show comparable performance. It is notable, as shown in Fig. 7, that in the higher frequency region, the main lobe of the coiled conical helix at $\theta = 0°$ direction is more stable, and thus generates higher directivity. In contrast, the radiation pattern of the simple conical helix deteriorates in higher frequencies and tilts away from the $\theta = 0°$ direction.

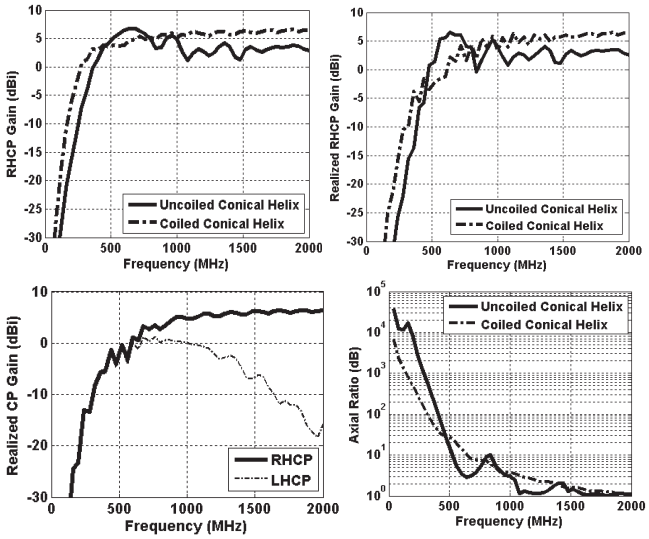

Fig. 6. The directivity and realized RHCP gains of the coiled conical helix are compared with those of the simple conical helix antenna over a broad bandwidth. Optimized coiled conical helix shows more miniaturization, higher wideband gain and comparable axial ratio.

In closing, we note that fabrication of the coiled conical helix is complex. As in [9], it can be realized using customized Beryllium copper coils. Coils with a tapered diameter and varying pitch can be manufactured by spring companies capable of making customized coils. Upright vertical boards can be employed to support the helix into specific concave contours to form the basic conical helix.

V. CONCLUSIONS

In this paper, we considered the minimization of a conical helix without appreciably compromising its broadband performance. To do so, we worked towards coiling the wire along the helical geometry. This should create an equivalent inductive loading and thus reduce the wave velocity along the spiral. The main challenge was to achieve best miniaturization without reducing high frequency gain. Hence, genetic algorithm (GA) optimization was adopted. A descriptive objective function was devised which weighted the

performance variably at 3 different frequency bands, a low, an intermediate and a high frequency regions. This was found necessary as it is allowed to control the UWB antenna performance effectively. After establishing the optimization variables and fitness function, we proceeded to demonstrate a customized design example. As shown, simple coiling achieved a 30% size reduction without severe gain degradation in the higher wide band regions.

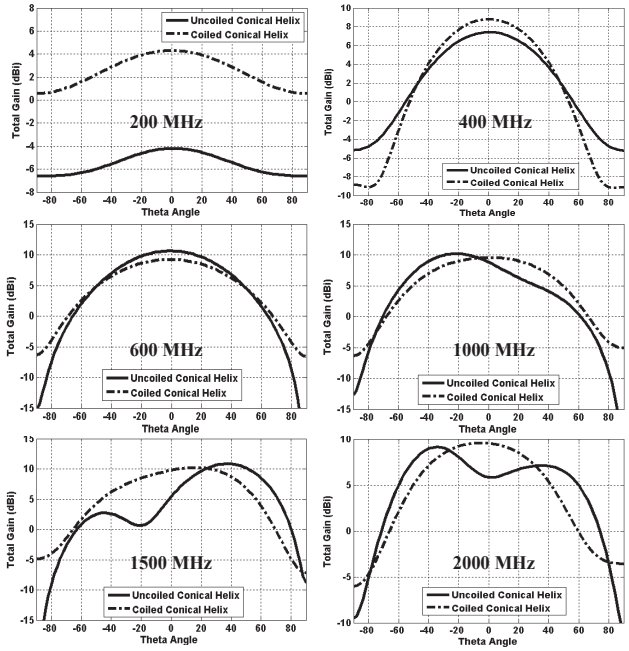

Fig. 7. Radiation patterns in the elevation plane of coiled conical helix and simple conical helix for different frequencies. At higher frequencies, coiled conical helix has more stable pattern and thus higher directivity than the simple conical helix.

REFERENCES

[1] H. E. King, J. L. Wong, and E. H. Newman, "Helical Antennas," ch. 12 in *Antenna Engineering Handbook* ed. by J. L. Volakis, McGraw-Hill, New York, 2007.

[2] J. D. Kraus and R. D. Marhefka, *Antennas*, 3rd ed., McGraw-Hill, New York, 2002.

[3] J. S. Chatterjee, "Radiation Field of a Conical Helix," *J. App. Physics*, vol. 24, no. 5, pp. 550-559, May 1953.

[4] V. H. Rumsey, "Frequency Independent Antennas," *IRE Int. Convention Record* vol. 5, pt. 1, pp. 114-118, Mar. 1957.

[5] J. D. Dyson and P. E. Mayes, "New Circularly-Polarized Frequency-Independent Antennas with Conical Beam or Omnidirectional Patterns," *IRE T. Antenna Propag.,* vol. 9, no. 4, pp. 334-342, Jul. 1961.

[6] J. L. Volakis, ed., *Antenna Engineering Handbook*, McGraw-Hill, New York, 2007.

[7] M. Lee, B. A. Kramer, C. C. Chen, and J. L. Volakis, "Distributed Lumped Loads and Lossy Transmission Line Model for Wideband Spiral Antenna Miniaturization and Characterization," *IEEE Trans. Antenna Propag.*, vol. 55, no. 10, pp. 2671-2678, Oct. 2007.

[8] B. A. Kramer, C. C. Chen, and J. L. Volakis, "Size Reduction of a Low-Profile Spiral Antenna Using Inductive and Dielectric Loading," *IEEE. Antenna Wirel. Pr.*, vol. 7, pp. 22-25, 2008.

[9] B. A. Kramer, "Size Reduction of an UWB Low-Profile Spiral Antenna," *Ph.D. Dissertation*, Ohio State University, 2007.

[10] Y. Rahmat-Samii and E. Michielssen, *Electromagnetic Optimization by Genetic Algorithms*, Wiley-Interscience, 1999.

[11] M. A. Mangoud, "Design of Circular Polarized Antennas using Genetic Algorithm based on Curved Wire Analysis," *Appl. Comput. Electrom.*, vol. 19, no. 3, pp. 177-183, Dec. 2004.

[12] G. J. Burke and A. J. Poggio, "Numerical Electromagnetic Code (NEC)--Method of Moments", Naval Ocean Systems Center, San Diego, Tech. Doc. NOSC TD 116, 1980.

[13] H. A. Wheeler, "The Radian Sphere around a Small Antenna," *Proceedings of the I.R.E.,* vol. 35, Aug. 1959.

[14] J. E. Rowe, *Nonlinear Electron-Wave Interaction Phenomena*, Academic Press, 1965.

[15] D. L. Carroll, FORTRAN Genetic Algorithm Driver, ver. 1.7, 1999. [Online]. Available: http://cuaerospace.com/carroll/ga.html

A Dual-Band Metamaterial Design using Double SRR Structures

Jian-Chao Liu, Wei Shao, and Bing-Zhong Wang

Institute of Applied Physics
University of Electronic Science and Technology of China, Chengdu, 610054, China
ljc_221@126.com, weishao@uestc.edu.cn, bzwang@uestc.edu.cn

Abstract ─ Based on a periodic array of interspaced conducting split ring resonators (SRRs) and continuous wires, a composite structure is proposed to hold a dual-band in the microwave regime. With simultaneously negative values of effective permeability and permittivity, the composite structure displays a negative refractive index characteristic in a dual-band. The location of the two resonant frequencies is investigated by adjusting the distance between the neighboring asymmetrical SRRs in a single array element. Numerical results show the impact of the distance on the resonant frequencies due to coupling effects. Different simulation softwares are adopted to verify the accuracy of our design.

Index Terms ─ Composite structure, mutual coupling effect, negative refractive index, SRRs.

I. INTRODUCTION

Negative index materials (NIMs), hypothesized by Veselago in 1968, are media in which the electric permittivity (ε_{eff}) and the magnetic permeability (μ_{eff}) are simultaneously negative over a common frequency band [1]. The interesting properties of NIMs, such as the reversal of Snell's Law, the Doppler effect, and the Vavilov-Cerenkov effect, have unique abilities to control the electromagnetic wave propagation and revolutionize the microwave component design. Up to now, an important approach to obtain negative values of effective permittivity over wide frequency bands is to use periodic thin wire arrays [2]. Negative values of effective permeability can be obtained by using special magnetic resonator structures, such as split ring resonators (SRRs) and spiral resonators [3]. Many studies have been made on NIM simulations, optimizations, and designs after the first NIM was demonstrated at microwave frequencies in 2000 [4]. For example, dual-band and multi-band metamaterials are developed for engineering applications [5-9]. Metamaterial studies on dual-band operations are reported in THz and near-infrared regions [5-6]. Those structures are composed of two individual resonators with different physical dimensions, which lead to different resonance frequencies. A metamaterial is proposed to possess three pass bands by utilizing the interactions between the ferrimagnetic host and wire array [7]. Multi-band metamaterials are obtained using micro-split SRR structures and multi-layer structures [8]. Those designs mentioned above almost ignore the effects of the mutual coupling between neighboring SRRs. In [9], two distinct resonances are achieved by using the effects of coupling between neighboring SRRs. The design chooses symmetrical structures and does not analyze the influence of the distance between neighboring SRRs.

In this paper, the effects of mutual couplings between two neighboring SRRs are utilized to obtain a dual-band characteristic. Each SRR in the asymmetrical structure responds to a resonant frequency band. How the distance between the two SRRs affecting the coupling effects is simulated and analyzed. Some parameter studies give design insights for practical applications. Finally, results with two different softwares for the dual-band structure calculation are in a good agreement.

II. CONFIGURATION AND ANALYSIS

The schematic view of the composite structure and its design parameters are given in Fig. 1. In this model, two copper SRRs and a wire are positioned on opposite sides of a substrate which

has a relative dielectric constant of $\varepsilon_r = 3.5$, a dielectric loss tangent of $\tan\delta_c = 0.003$ and a thickness of $d = 0.5$ mm. The thickness and conductivity of the copper are 0.017mm and 5.8×10^7 S/m, respectively. In Fig. 1(a), the distance h between the neighboring SRRs is a variable parameter.

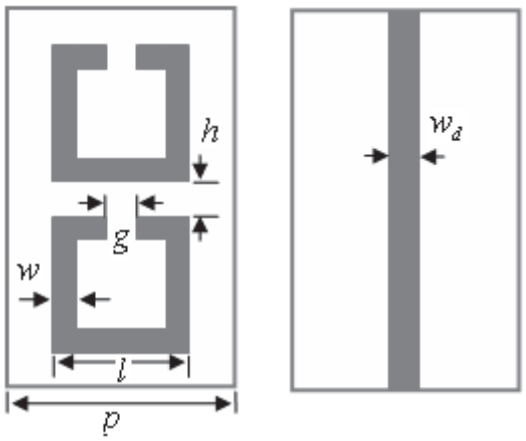

(a) Top view. (b) Bottom view.

Fig. 1. Schematic view of the composite structure. The geometry parameters are $p = 5$mm, $l = 4$mm, $w = 0.5$mm, and $g = 0.2$mm and $w_d = 0.2$mm.

It is noted that the two SRRs form two different resonant circuits (Loop1 and Loop2) are due to the asymmetry along the horizontal line. When changing the distance h between the two SRRs, the resonant frequencies will shift. Because of the existence of the slit where the electromagnetic fields concentrate, the effect of couplings between the two SRRs has a greater impact on Loop2 than Loop1. Thus, the resonance of Loop2 changes greatly when changing h. So, it is particularly important to understand the coupling between neighboring SRRs for the dual-band design of the structures. This prediction will be verified in the following section.

III. RESULTS AND DISCUSSION

The simulations are performed by using two commercial electromagnetic softwares: Ansoft HFSS and CST Microwave Studio. The investigated array composed of the composite structures shown in Fig. 1 is plotted in Fig. 2. Only an element is needed to be extracted for analysis due to the periodicity. The unit structure under investigation is excited by a plane wave from $-y$ direction with z polarization. The walls perpendicular to the z-axis are modeled to be perfect electrical conductors (PECs) while the walls perpendicular to x-axis are modeled to be perfect magnetic conductors (PMCs). The remaining walls, which are perpendicular to the y-axis, are modeled to be the input/output ports.

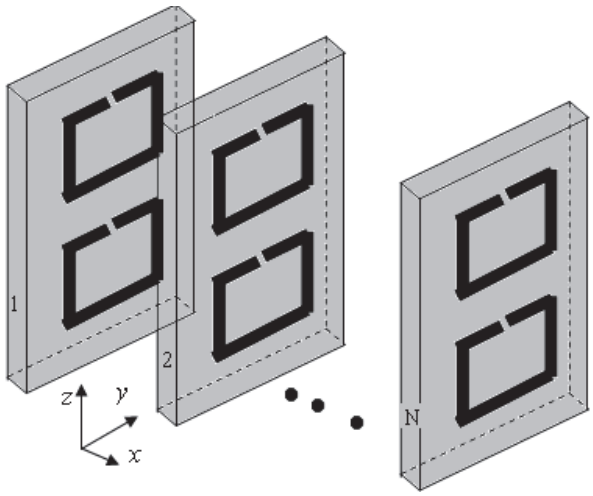

Fig. 2. Schematic three-dimensional simulation of array.

In this section, the effective medium parameters (μ_{eff}, ε_{eff} and n_{eff}) as well as the transmission characteristics are investigated for the proposed structure. Herein, the effective medium parameters of a given structure can be found by a standard retrieval algorithm [10]. In order to verify the identity of views between the artificial magnetism from electromagnetics and the negative refractive index from optics, the resonance responses of the composite structure without the wire are plotted in Fig. 3.

Compared to a single SRR structure with the same size, the interaction of the two SRRs splits the magnetic resonance into two resonances, as shown in Fig. 3(a) where the location of resonance will shift when changing the distance h between the two neighboring SRRs. When h is less than 0.2 mm, the lower resonance becomes weak and the upper resonance is closer to that of the single SRR structure. Figure 3(b) shows that there are two regions with negative permeability near the

resonance frequencies. It is also found that the regions shift when changing the distance h, similar to the results in Fig. 3(a). The dips in the phase curve of S_{21} in Fig. 3(c) indicate the presence of two negative permeability bands.

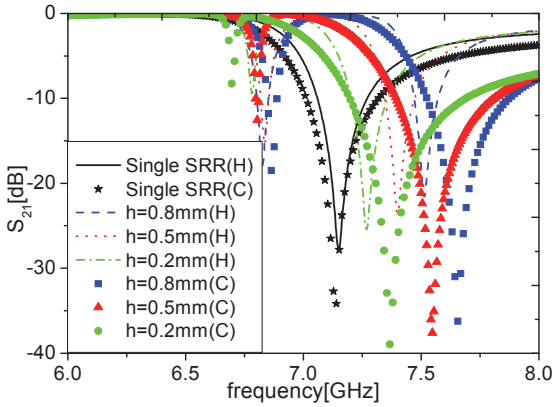

(a) S_{21} versus frequency（H-HFSS, C-CST).

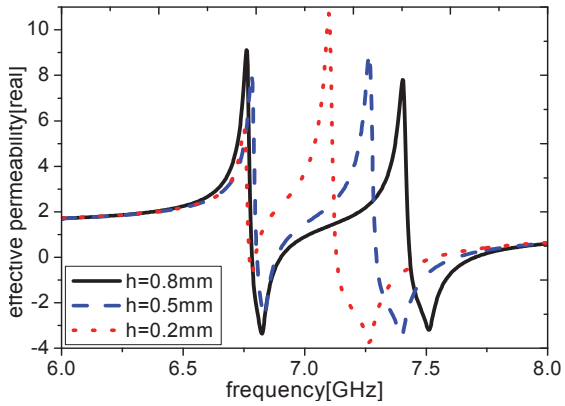

(b) Effective permeability versus frequency.

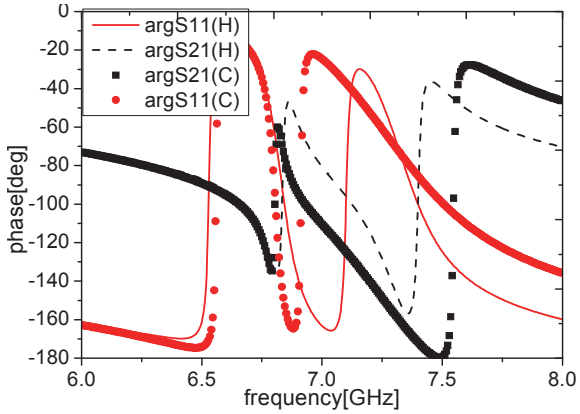

(c) T/R phase versus frequency ($h = 0.5$mm).

Fig. 3. Simulation results for the proposed structures without the wire.

In the following, the response of the structure with a metal wire is investigated. Amplitudes of the S_{21} parameters with different distance h are plotted in Fig. 4(a). Also, the effective relative permeability, effective relative permittivity and effective refractive index are given in Figs. 4(b), (c), and (d), respectively. It is found that resonant frequencies in the structure with a wire have a down shift, but the regions with negative permeability are consistent. At the same time, the value of effective permittivity is negative in the region. It can be expected that the structure will exhibit a regime of negative refractive index when the negative permeability band in Fig. 4(c) and the negative permittivity band in Fig. 4(d) overlap. Figure 4(d) shows that there are two regions exhibiting the negative refractive index. It is also noted that when changing the distance h, the negative index regions will shift, same as the previous results.

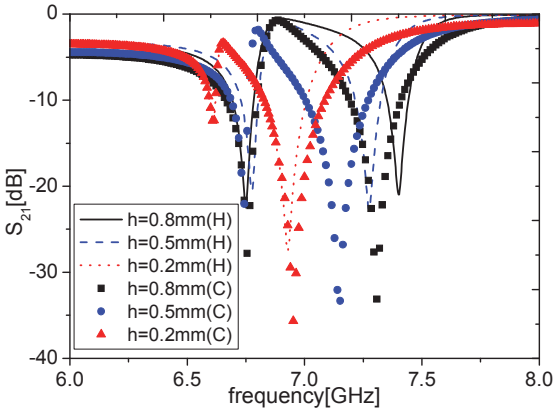

(a) S_{21} versus frequency (H-HFSS, C-CST).

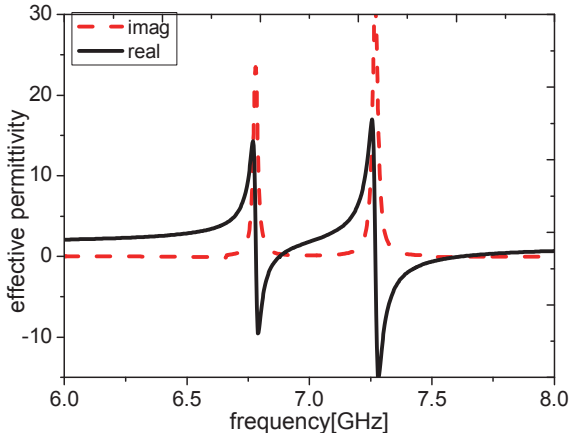

(b) Effective permeability versus frequency.

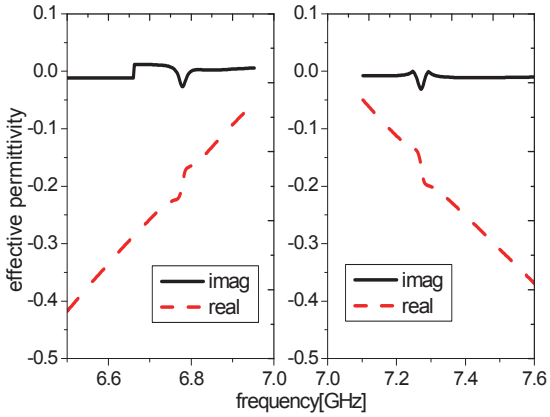

(c) Effective permittivity versus frequency.

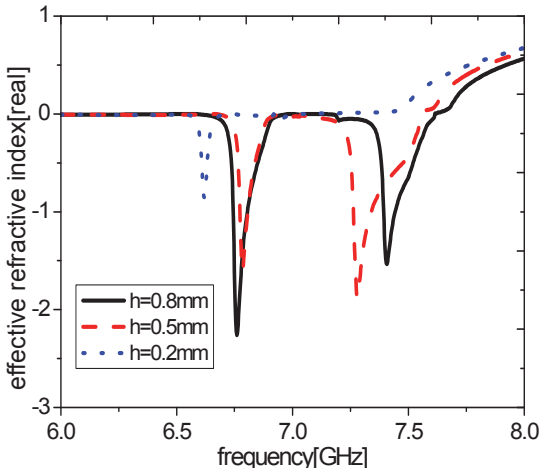

(d) Effective refractive index versus frequency.

Fig. 4. Simulation results for the proposed structures.

IV. CONCLUSION

In this paper, a composite structure composed of double SRRs is proposed to realize a dual-band characteristic. The effects of coupling between neighboring SRRs is considered as one of the major factors in this design. Numerical results show the impact of the distance between neighboring SRRs on the resonant frequencies. Our future works may be focused on how to obtain desired resonances in metamaterials by adjusting the coupling effects.

ACKNOWLEDGEMENT

This work is supported in part by the National Natural Science Foundation of China (60901023), the DPR Foundation (9140A03011210DZ02) and the Fundamental Research Funds for the Central Universities (ZYGX2010J043).

REFERENCES

[1] V. G. Veselago, "The Electrodymics of Substances with Simultaneously Negative Values of ε and μ," *Soviet. Physics. Uspekhi,* vol. 10, no. 4, pp. 509-514, 1968.

[2] J. B. Pendry, "Extremely Low Frequency Plasmons in Metallic Mesostructures," *Phy. Rev. Lett*. vol. 76, no. 25, pp. 4773-4776, 1996.

[3] J. B. Pendry, A. J. Holden, D. J. Robbins, and W. J. Stewart, "Magnetism from Conductors and Enhanced Nonlinear Phenomena," *IEEE Trans. Microw.Theory Tech*., vol. 47, no. 11, pp. 2075-2084, 1999.

[4] D. R. Smith, W. Padilla, D. C. Vier, S. C. Nemat-Nasser, and S. Schultz, "Composite Medium with Simultaneously Negative Permeability and Permittivity," *Phys. Rev. Lett*.,vol. 84, no. 18, pp. 4184-4187, 2000.

[5] D. -H. Kwon, D. H. Werner, A. V. Kildishev, and V. M. Shalaev, "Near-Infrared Metamaterials with Dual-Band Negative-Index Characteristics," *Opt. Express*, vol. 15, no. 4, pp. 1647-1652, 2007.

[6] Y. Yuan, C. Bingham, T. Tyler, S. Palit, T. H. Hand, W. J. Padilla, D. R. Smith, N. M. Jokerst, and S. A. Cummer, "Dual-Band Planar Electric Metamaterial in Terahertz Regime," *Opt. Express*, vol. 16, no. 13, pp. 9746-9752, 2008.

[7] Y. Huang, G. Wen, T. Li, K. Xie, "Positive-Negative-Positive Metamaterial Consisting of Ferrimagnetic Host and Wire Array," *Applied Computational Electromagnetic Society (ACES) Journal*, vol. 25, no. 8, pp. 696-702, August 2010.

[8] E. Ekmekci, K. Topalli, T. Akin, and G.Turhan-Sayan, "A Tunable Multi-Band Metamaterial Design Using Micro-Split SRR Structures," *Opt. Express*, vol. 17, no. 18, pp. 16046-16058, 2009.

[9] R. S. Penciu, K. Aydin, M. Kafesaki, Th. Koschny, E. Ozbay, E. N. Economou, and C. M. Soukoulis, "Multi-Gap Individual and Coupled Split-Ring Resonator Structures," *Opt. Express*, vol. 16, no. 22, pp. 18131-18144, 2008.

[10] D. R. Smith, D. C. Vier, Th. Koschny, and C. M. Soukoulis, "Electromagnetic Parameter

Retrieval from Inhomogeneous Metamaterials," *Phy. Rev. Lett*. E 71, 036617, 2005.

Jian Chao Liu received the B.E. degree in Information Engineering form Henan Institute of Science and Technology, Xinxiang, China, in 2009.

From September 2009 to now, he is pursuing the M. Sc. degree in Institute of Applied Physics in University of Electronic Science and Technology of China (UESTC), Chengdu, China. His current research interests include metamaterials and their applications.

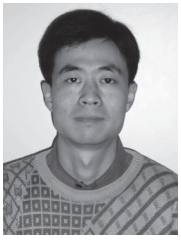

Wei Shao received the M. Sc. and Ph. D. degrees in Radio Physics from UESTC, Chengdu, China, in 2004 and 2006, respectively.

He joined the UESTC and is now an associate professor there. He has been a Visiting Scholar in the Electromagnetic Communication Laboratory, Pennsylvania State University in 2010. His research interests include the computational electromagnetics and antenna technique.

Bing-Zhong Wang received the Ph.D. degree in Electrical Engineering from UESTC, Chengdu, China, in 1988.

He joined the UESTC in 1984 and is currently a Professor there. He has been a Visiting Scholar at the University of Wisconsin-Milwaukee, a Research Fellow at the City University of Hong Kong, and a Visiting Professor in the Electromagnetic Communication Laboratory, Pennsylvania State University. His current research interests are in the areas of computational electromagnetics, antenna theory, and computer-aided design for microwave circuits.

A PML for Electroacoustic Waves in Piezoelectric Materials Using FDTD

Arthur O. Montazeri, Mohamed H. Bakr, and Yaser M. Haddara

Department of Electrical and Computer Engineering
McMaster University, Hamilton, ON, L8S 1M6, Canada
montazo@mcmaster.ca, mbakr@mail.ece.mcmaster.ca, yaser@mcmaster.ca

Abstract ─ A perfectly matched layer (PML) is introduced for elastodynamic waves in piezoelectric materials. A matching condition is derived for the PML equations to reduce spurious reflections from the boundary. The finite difference time domain (FDTD) is used to model the propagation of the wave in the piezoelectric material. The results show good performance of the proposed PML boundary.

Index Terms ─ Elastodynamic wave, FDTD, piezoelectric materials, PML, SAW.

I. INTRODUCTION

Much interest is devoted to the surface acoustic wave (SAW) devices due to the versatility of their application and their widespread use. SAW-based resonators and delays are readily used in commercial telecommunication systems [1]. This makes any error reduction method, before the onset of fabrication, an extremely powerful tool for the industry. It also highlights the use of the computer aided design software in determining the SAW device responses prior to manufacturing.

Surface acoustic wave simulators are generally categorized into two groups: behavioural models and physics-based models [2,3]. Behavioural models, also known as phenomenological models, are employed to quickly obtain the device response, typically by expanding the response in terms of certain basis functions [4]. On the other hand, physics-based models, also referred to as full-wave models, are more accurate. They directly solve the differential equations of SAW generation [3]. There is also another fundamental difference between the two: physics-based models need only be supplied with the boundary conditions of the problem, the excitation, and the initial conditions. Behavioural techniques, on the other hand, require a set of parameters describing an already-existing wave. These parameters are either extracted from experimental measurements, or from physics-based simulations. A popular behavioural modeling approach is the coupling-of-modes (COM) method explained in [3]. References describing other phenomenological models exist [3, 5-7]. As a result, the two simulation methodologies are often complementary, rather than competitive.

Frequency domain techniques are in particular powerful for determining SAW device responses at specific frequencies [6]. On the other hand, in order to obtain a wideband device response, a large number of such simulations are required. This is where time domain techniques prove their worth [8]. Most SAW device modeling has been done in the frequency domain, and so a wider selection of boundary conditions including the PML is available in the frequency domain.

At the same time, time domain techniques such as FDTD, provide a powerful tool for wideband frequency response simulation. FDTD can also incorporate anisotropic media which include all piezoelectric materials. These properties make FDTD a suitable candidate for simulating micro-acoustic devices [9].

In this paper, we develop an FDTD physics-based model through the discretization of the piezoelectric governing equations. We describe an improvement to reduce spurious reflections from the PML boundary. PML implementations for this

type of structure based on existing recipes cause instabilities for certain crystal groups [9]. Here, a PML for acoustic waves is derived by closely following Bérenger's derivation of a PML for electromagnetic waves. A new matching condition is developed to relate the velocity and stress loss-coefficients similar to the matching condition defined for electromagnetic waves.

Our paper is organized as follows: In Section II, SAW devices are introduced along with an overview of absorbing boundary conditions. In Section III, our parallel derivation of a PML for the elastodynamic wave equation is given. We present the PML time update equations based on the derived matching condition. Finally, Section IV presents the results.

II. BACKGROUND

A. SAW generation and propagation

In the SAW devices considered here, surface acoustic waves are generated by the application of an excitation to a thin metal interdigital transducer (IDT) deposited on the free surface of a piezoelectric substrate, as shown in Fig. 1.

Generally, two IDTs, separated on the surface of the piezoelectric substrate, constitute a basic two-port SAW device. One IDT acts as a transmitter and the other as a receiver. The transmitting IDT converts the electrical signal into mechanical wave vibrations, which travel through the medium to reach the receiver IDT. Through the piezoelectric effect, the mechanical SAW wave is converted back into an electrical output signal. The two-port devices considered here are compliant with the reciprocity theorem, where switching the transmitter and receiver ports will have no effect on the device functionality [1].

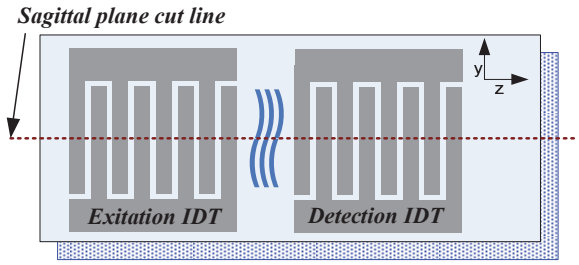

Fig. 1. A 2-port SAW device.

In the IDT region of the wave generation zone, the substrate should be piezoelectric. The region in between the IDTs needs only be elastic, as it merely acts as the transmission medium for the SAW [1]. At the receiver IDT, a piezoelectric substrate is required to convert the mechanical wave back into an electrical signal.

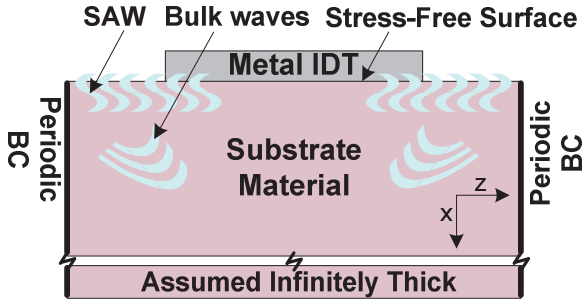

Fig. 2. One IDT finger on the sagittal plane of a SAW device.

Figure 2 shows the sagittal plane (side view) of the SAW device, indicated by the cut line in Fig. 1. SAW waves are generally confined to within one or two wavelengths from the free surface of the substrate material. However, other types of excitations, such as bulk acoustic waves (BAWs) will radiate into the substrate.

In practice, the SAW generation is often also accompanied by some small creation of BAWs, which act as parasitic waves. It is thus required to remove the reflection of these waves from the bottom of the device.

Figure 1 also shows the symmetry of the device with respect to the sagittal cut line. This, along with the assumption that the device is infinitely thick in the y direction, allows for a complete analysis of the device by only studying the sagittal plane. The problem can therefore be analyzed in the xz plane denoting the sagittal plane, thus significantly reducing the computational requirements.

B. Absorbing boundary conditions and the perfectly matched layer

Several absorbing boundary conditions (ABCs) have been suggested with progressive improvements. Most of these ABCs were originally developed for electromagnetic wave propagation [11, 12]. In his 1994 paper, Bérenger described his PML, which offered significant improvement over previous ABCs [10].

In a pioneering work in 1996, Chew and Liu developed a PML for elastodynamics [13]. In 2006, Chagla and Smith introduced a PML for piezoelectric materials by splitting the velocity components into the normal and tangential subcomponents, and only attenuating the normal velocity subcomponents. The resulting absorbing boundary condition showed instabilities for some crystal classes [9]. Here, we introduce losses, not just for the velocity components, but for the stress field subcomponents as well, thereby generalizing the loss matrix. At the same time, by preserving the matching condition throughout, the code remains stable.

C. The PML for electromagnetic wave propagation

The ABC equations for the electromagnetic waves are

$$\varepsilon_0 \frac{\partial \boldsymbol{E}}{\partial t} + \sigma \boldsymbol{E} = \nabla \times \boldsymbol{H}\,, \tag{1}$$

$$\mu_0 \frac{\partial \boldsymbol{H}}{\partial t} + \sigma^* \boldsymbol{H} = -\nabla \times \boldsymbol{E}\,, \tag{2}$$

where σ is the conductivity and σ^* is a non-physical quantity that symmetrises the absorption of the magnetic field with that of the electric field [10]. ε_o, and μ_o are the permittivity and permeability of the free space, respectively. In order to demonstrate the method, we show the case where a medium is matched to the vacuum. In general however, the computational domain can be matched to any number of media, for instance, a dielectric, an isotropic material, a non isotropic material, or in fact to another PML.

The matching condition in Bérenger's derivation is defined as [14]

$$\frac{\sigma}{\varepsilon_0} = \frac{\sigma^*}{\mu_0}\,. \tag{3}$$

This impedance matching equation ensures that the impedance of the wave travelling inside the domain matches that of the lossy ABC medium defined by equation (1) and (2). The result is a reflectionless propagation of a normally incident plane wave as it passes through the interface. This works well at normal incidences. However, the reflection becomes large at grazing angles.

Bérenger addressed this problem, by splitting the field quantities into normal and tangential components and modifying equations (1) and (2). The reflection coefficient with n=1 for vacuum, matched to this newly defined lossy medium is given by

$$r = \left(\frac{1-\cos\theta}{1+\cos\theta}\right)^n\,. \tag{4}$$

This reflection coefficient is thus zero for both normal and grazing incidence [14].

III. OUR APPROACH

Here, the PML for the elastodynamic wave propagation on piezoelectric solids is derived in exact parallelism with Bérenger's formulation of the PML for electromagnetic waves [10].

The equations describing the propagation of elastodynamic waves in piezoelectric crystals are [15]

$$\hat{\boldsymbol{s}}^{\boldsymbol{E}} \frac{\partial \boldsymbol{T}}{\partial t} = \nabla_s \boldsymbol{v}\,, \tag{5}$$

$$\rho \frac{\partial \boldsymbol{v}}{\partial t} = \nabla \boldsymbol{T}\,. \tag{6}$$

Below is a list of symbols used in the equations along with their definitions:

$\boldsymbol{T}$	stress field in abbreviated subscript form (6×1 matrix),
$\boldsymbol{d}$	piezoelectric strain coefficient (3×6 matrix),
$\boldsymbol{c}^{\boldsymbol{E}}$	stiffness matrix under constant electric field (6×6 matrix),
$\boldsymbol{s}^{\boldsymbol{E}}$	compliance coefficients matrix under constant electric field (6×6 matrix),
$\boldsymbol{d}'$	Transpose of d,
$\boldsymbol{v}$	particle velocity (3×1 matrix),
ρ	material density,
$\nabla\times$	$\begin{bmatrix} 0 & -\partial/\partial z & \partial/\partial y \\ \partial/\partial z & 0 & -\partial/\partial x \\ -\partial/\partial y & \partial/\partial x & 0 \end{bmatrix}$, and

$$\nabla_{\cdot} = \left(\nabla_{s}\cdot\right)' \begin{bmatrix} \partial/\partial x & 0 & 0 & 0 & \partial/\partial z & \partial/\partial y \\ 0 & \partial/\partial y & 0 & \partial/\partial z & 0 & \partial/\partial x \\ 0 & 0 & \partial/\partial z & \partial/\partial y & \partial/\partial x & 0 \end{bmatrix}$$

Here, prime denotes a transpose matrix and c^E is the inverse of s^E. Also,

$$\hat{\boldsymbol{s}}^E = \left(\hat{\boldsymbol{c}}^E\right)^{-1} = \boldsymbol{s}^E - \boldsymbol{d}'(\boldsymbol{\varepsilon}^T)^{-1}\boldsymbol{d}\,, \tag{7}$$

is called the stiffening equation which includes the effects of piezoelectricity at zero displacement [15]. In component-form, the first line of equation (5), for a trigonal 3m symmetry class crystal, such as lithium niobate ($LiNbO_3$) is [15]

$$s_{11}\frac{\partial}{\partial t}T_1 + s_{12}\frac{\partial}{\partial t}T_2 + s_{13}\frac{\partial}{\partial t}T_3 + s_{14}\frac{\partial}{\partial t}T_4 = \frac{\partial v_1}{\partial x}\,. \tag{8}$$

The PML is defined by introducing losses for the component field variables. The loss terms are introduced in accordance with the existing terms in equation (8).

The form of the stiffness matrix determines which components of the stress field are present, and in turn, which loss terms appear in the PML equation. Accordingly, the number of terms in this equation depends on the choice of substrate material. Similar to electromagnetics, equation (8) is used to develop a Bérenger-like boundary condition.

Equation (8) is split into the normal and tangential field subcomponents in the *xz* plane, (i.e. no *y*-dependence) to have

$$\begin{aligned} &s_{11}\frac{\partial}{\partial t}T_{1x} + s_{12}\frac{\partial}{\partial t}T_{2x} + s_{13}\frac{\partial}{\partial t}T_{3x} + s_{14}\frac{\partial}{\partial t}T_{4x} \\ &\psi_{T1}T_{1x} + \psi_{T2}T_{2x} + \psi_{T3}T_{3x} + \psi_{T4}T_{4x} \\ &= \frac{\partial(v_{1x} + v_{1z})}{\partial x} \end{aligned} \tag{9}$$

$$s_{11}\frac{\partial}{\partial t}T_{1z} + s_{12}\frac{\partial}{\partial t}T_{2z} + s_{13}\frac{\partial}{\partial t}T_{3z} + s_{14}\frac{\partial}{\partial t}T_{4z} = 0. \tag{10}$$

where Ψ_{Ti} denote the loss term for the corresponding stress component.

For the computational grid depicted in Fig. 3, where the direction of attenuation is along the x-axis, the PML equations, in vector form are given by

$$\hat{\boldsymbol{s}}^E\frac{\partial \boldsymbol{T}_x}{\partial t} + \boldsymbol{\Psi}_T\boldsymbol{T}_x = \nabla_{sx}\boldsymbol{v} \tag{11}$$

$$\hat{\boldsymbol{s}}^E\frac{\partial \boldsymbol{T}_z}{\partial t} = \nabla_{sz}\boldsymbol{v} \tag{12}$$

$$\rho\frac{\partial \boldsymbol{v}_x}{\partial t} + \psi_v\boldsymbol{v}_x = \nabla_x\boldsymbol{T} \tag{13}$$

$$\rho\frac{\partial \boldsymbol{v}_z}{\partial t} = \nabla_z\boldsymbol{T}\,, \tag{14}$$

where $\boldsymbol{\Psi}_T$ is a 6×6 stress loss tensor containing non zero Ψ_{Ti} components only where the $\hat{\boldsymbol{s}}^E$ matrix has nonzero entries. ψ_v is a non-physical scalar denoting the velocity loss-coefficient, and ∇_{sx}, similar to the ∇_s, is a matrix whose only non-zero entries are $\partial/\partial x$. ∇_{sz}, ∇_x, and ∇_z is similarly defined.

Noting that some coefficients are now tensor quantities, we define the acoustic matching condition as

$$\boldsymbol{\Psi}_T = \frac{\psi_v}{\rho}\hat{\boldsymbol{s}}^E\,. \tag{15}$$

This relation states that the ratios between the stress and velocity loss-coefficients are the same as the ratios of the field variable coefficients. Similar to the electromagnetic case, the matching condition (15) ensures that the loss-coefficients always maintain the same ratio, even as they progressively increase through the PML.

C. The PML time update equations

The derivation of the PML time update equation for the velocity field is less burdensome. This has been previously reported as [9]

$$\boldsymbol{v}_x^{\,n+1/2} = \left(\frac{2-\Delta t\psi_{v,i}}{2+\Delta t\psi_{v,i}}\right)\boldsymbol{v}_x^{\,n-1/2} + \frac{\Delta t}{\rho}\left(\frac{1}{2+\Delta t\psi_{v,i}}\right)\nabla_x\boldsymbol{T}\,. \tag{16}$$

As for the PML time update equations for the stress field, we start with the first row of equation (11). The same analysis applies to the remaining five rows. The first row of this equation in component form is:

$$\begin{aligned} & s_{11}\frac{\partial}{\partial t}T_{1x}+s_{12}\frac{\partial}{\partial t}T_{2x}+s_{13}\frac{\partial}{\partial t}T_{3x}+s_{14}\frac{\partial}{\partial t}T_{4x}+ \\ & +\psi_{T1}T_{1x}+\psi_{T2}T_{2x}+\psi_{T3}T_{3x}+\psi_{T4}T_{4x} \\ & =\frac{\partial(v_{1x}+v_{1z})}{\partial x}. \end{aligned} \tag{17}$$

Applying the time-averaging, for quantities at time n and using a central difference scheme for approximating the time derivatives, equation (17) becomes

$$\begin{aligned} & s_{11}\left(\frac{T_{1x}\Big|_{i,j}^{n+1/2}-T_{1x}\Big|_{i,j}^{n-1/2}}{\Delta t}\right)+s_{12}\left(\frac{T_{2x}\Big|_{i,j}^{n+1/2}-T_{2x}\Big|_{i,j}^{n-1/2}}{\Delta t}\right)+ \\ & +s_{13}\left(\frac{T_{3x}\Big|_{i,j}^{n+1/2}-T_{3x}\Big|_{i,j}^{n-1/2}}{\Delta t}\right)+s_{14}\left(\frac{T_{4x}\Big|_{i,j}^{n+1/2}-T_{4x}\Big|_{i,j}^{n-1/2}}{\Delta t}\right)+ \\ & +\psi_{T1}\left(\frac{T_{1x}\Big|_{i,j}^{n+1/2}+T_{1x}\Big|_{i,j}^{n-1/2}}{2}\right)+\psi_{T2}\left(\frac{T_{2x}\Big|_{i,j}^{n+1/2}+T_{2x}\Big|_{i,j}^{n-1/2}}{2}\right)+ \\ & +\psi_{T3}\left(\frac{T_{3x}\Big|_{i,j}^{n+1/2}+T_{3x}\Big|_{i,j}^{n-1/2}}{2}\right)+\psi_{T4}\left(\frac{T_{4x}\Big|_{i,j}^{n+1/2}+T_{4x}\Big|_{i,j}^{n-1/2}}{2}\right) \\ & =\frac{\partial(v_{1x}+v_{1z})}{\partial x}. \end{aligned} \tag{18}$$

Grouping the terms at time $n+0.5$ yields the time update equation

$$\begin{aligned} & (2s_{11}+\Delta t\psi_{T1})T_{1x}\Big|_{i,j}^{n+1/2}+(2s_{12}+\Delta t\psi_{T2})T_{2x}\Big|_{i,j}^{n+1/2}+ \\ & +(2s_{13}+\Delta t\psi_{T3})T_{3x}\Big|_{i,j}^{n+1/2}+(2s_{14}+\Delta t\psi_{T4})T_{4x}\Big|_{i,j}^{n+1/2}+ \\ & =(2s_{11}-\Delta t\psi_{T1})T_{1x}\Big|_{i,j}^{n-1/2}+(2s_{12}-\Delta t\psi_{T2})T_{2x}\Big|_{i,j}^{n-1/2}+ \\ & +(2s_{13}-\Delta t\psi_{T3})T_{3x}\Big|_{i,j}^{n-1/2}+(2s_{14}-\Delta t\psi_{T4})T_{4x}\Big|_{i,j}^{n-1/2}+ \\ & 2\Delta t\frac{\partial(v_{1x}+v_{1z})}{\partial x}. \end{aligned} \tag{19}$$

For all rows, the result can be cast in the more concise matrix form

$$(2\hat{\boldsymbol{s}}^{E}+\Delta t\boldsymbol{\Psi}_{T})\boldsymbol{T}_{\boldsymbol{x}}\Big|_{i,j}^{n+1/2}=(2\hat{\boldsymbol{s}}^{E}-\Delta t\boldsymbol{\Psi}_{T})\boldsymbol{T}_{\boldsymbol{x}}\Big|_{i,j}^{n-1/2}+2\Delta t\nabla_{x}\boldsymbol{v}. \tag{20}$$

Making use of the matching condition defined in equation (15) to substitute for $\boldsymbol{\Psi}_{\boldsymbol{T}}$, we have:

$$\begin{aligned} & (2\hat{\boldsymbol{s}}^{\boldsymbol{E}}+\Delta t\hat{\boldsymbol{s}}^{\boldsymbol{E}}\frac{\psi_v}{\rho})\boldsymbol{T}_x\Big|_{i,j}^{n+1/2}= \\ & (2\hat{\boldsymbol{s}}^{\boldsymbol{E}}-\Delta t\hat{\boldsymbol{s}}^{\boldsymbol{E}}\frac{\psi_v}{\rho})\boldsymbol{T}_x\Big|_{i,j}^{n-1/2}+2\Delta t\nabla_x\boldsymbol{v}. \end{aligned} \tag{21}$$

Multiplying by $\hat{\boldsymbol{c}}^{\boldsymbol{E}}$ which is the inverse of $\hat{\boldsymbol{s}}^{\boldsymbol{E}}$ the time update equation within the PML becomes

$$\boldsymbol{T}_x{}^{n+1/2}=\frac{\xi_v}{\xi_v^*}\boldsymbol{T}_x{}^{n-1/2}+\frac{2\Delta t}{\xi_v^*}\hat{\boldsymbol{c}}^{\boldsymbol{E}}\nabla_x\boldsymbol{v} \tag{22}$$

where $\xi_v=(2-\Delta t\psi_v/\rho)$ and $\xi_v^*=(2+\Delta t\psi_v/\rho)$. It should be noted that the quantities ξ_v and ξ_v^* are scalars. There is no need for matrix inversion. This significantly relaxes the computational resources for calculating the field values inside the PML. The $\boldsymbol{T}_z$ component of the stress field is allowed to propagate without loss, and the equation is given by

$$\boldsymbol{T}_z{}^{n+1/2}=\boldsymbol{T}_z{}^{n-1/2}+\Delta t\,\hat{\boldsymbol{c}}^{\boldsymbol{E}}\nabla_z\boldsymbol{v}\,. \tag{23}$$

The end of the boundary is often terminated with a perfect reflector. This ensures that any reflections from the terminal layer of the PML undergo a secondary attenuation upon return.

The matching condition is in essence a constraint, which connects the loss-coefficients of the stress and velocity fields. That is, setting ψ_v is sufficient for defining both equations (16) and (22). Note that these two equations define one layer of the PML. An arbitrary number of layers can be specified. Generally the more layers the PML has, the better it is in suppressing reflections.

From one layer to the next, starting at the medium-PML interface, the loss-coefficients are gradually increased according to a profile function. At the starting layer, the loss-profile ψ_v is small; however, it is ramped up at every layer, terminating at a final value $\psi_{v,0}$ at the end of the PML. Generally, either a polynomial or exponential loss profile is employed to define the sequence of ψ_v values, as is done in electromagnetics. We have used a polynomial loss profile given by [14]

$$\psi_{v,i} = \psi_{v,0}\left(\frac{i - x_{PML}}{\delta}\right)^m, \qquad (24)$$

where x_{PML} is the position of the onset of the PML, i is the position of each PML, δ is the thickness of the PML, $\psi_{v,0}$ is the loss-coefficient at the terminal layer of the PML, and m is the order of the polynomial used. $\psi_{v,0}$ is either chosen heuristically, or using an empirical formula similar to the electromagnetic PML explained in [12].

IV. RESULTS AND DISCUSSION

Figure 3 shows the computational domain, which is the discretized sagittal plane depicted in Fig. 2. The domain is terminated on the left and the right sides by periodic boundaries, modelling an infinite interdigital transducer (IDT). This is the case, for example, in a SAW resonator, where the excitation travels symmetrically in both directions.

A. Point-excitation in the vicinity of the PML

The first example addresses the case of a point excitation in the vicinity of the PML. The domain is one IDT period of the sagittal plane shown in Fig. 2 with the assumption that the IDT is infinitely long compared to the wavelength of the SAW. This reduces the problem to a two dimensional analysis in the sagittal plane. A spatial resolution of 33.57×10^{-5} m, and a temporal timestep of 0.318 ns are used on a 91×91 grid.

The PML was tested for sinusoidal, Gaussian, and impulse excitations placed 8 spatial steps from a PML with 15 layers. The relative amplitude of reflection for all excitations, was less than 10^{-6} after 6000 timesteps or 19 μs.

The implemented PML is used for the bottom of the domain. This allows any unwanted parasitic waves to be removed from the computational domain, as though the computational domain were a semi-infinite plane. Any other boundary condition will result in spurious reflections from the bottom that will show up in the detection IDT of the device as computational noise.

The top boundary condition is stress-free, implying that all components of the stress normal to the boundary (i.e. T_1, T_5, T_6) are set to zero [8]. Therefore, at the stress-free boundary, the only non-zero components of the stress are the transverse ones.

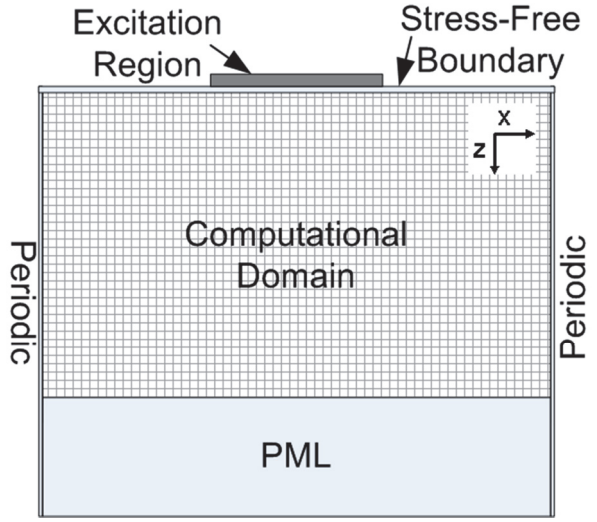

Fig. 3. The computational domain.

A Gaussian-modulated sinusoidal with a center frequency of 1.0 GHz is applied to the middle of the free surface. This excitation is applied to the T_3 component of the wave which is a compressional stress component in the z-direction.

Figure 4 shows the plot of the v_1 component of the field in an unbounded region, where the wave is freely propagating (solid curve) vs. the same measurement when one side of the boundary is terminated by a PML. The two curves are virtually overlapping and the reflection is under 10^{-6} as seen in Fig. 4.

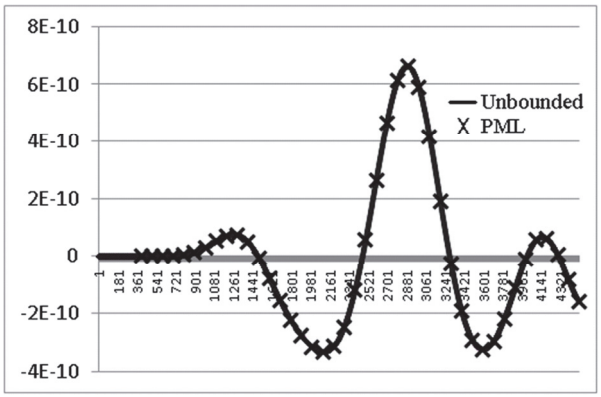

Fig. 4. A comparison of reflection of the normalized v_1 field component for an unbounded medium and a PML-bounded medium. The vertical axes is the amount of reflection from the boundary and the horizontal axes denotes the number of timesteps.

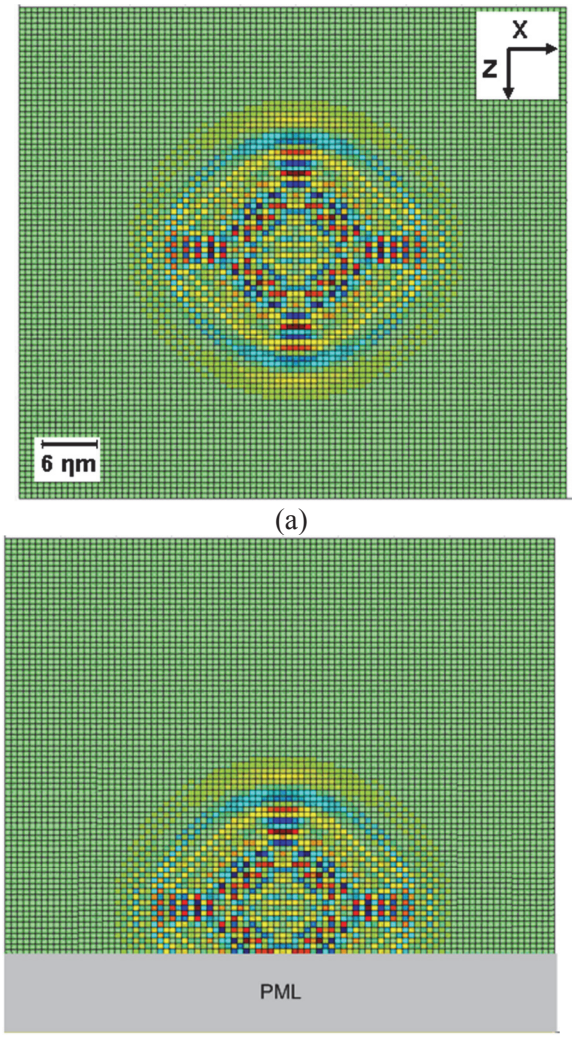

(a)

(b)

Fig. 5. v_1 field component of an excitation near the PML; (a) A sinusoidal excitation in an unbounded region, and (b) symmetric spread of the same excitation near the PML after 15.9 μs or 5000 time steps.

Figure 5(a) shows the propagation of the wave in the unbounded region while Fig. 5(b), shows the field near the boundary after 15.9 μs. The two profiles are identical for the domain region outside the PML. The symmetric shape of the excitation is preserved even after a prolonged interaction with the PML.

B. Line-excitation via a metallic IDT

Figure 6 shows the excitation under the metallic IDT in the computational domain of Fig. 2. The excitation for this example is a line source underneath the metallic strip. A Gaussian-modulated time profile with a center frequency of 1.0 GHz is also used in this example. The crystal cut is chosen as 128 X-Cut Y propagating lithium niobate. The main excitation type is of Rayleigh type; with some bulk waves also excited.

If these excitations are not removed, they introduce computational noise, shown in Fig 7(a) where the domain is not terminated with a PML. The reflections are magnified in the figure near their corresponding boundaries.

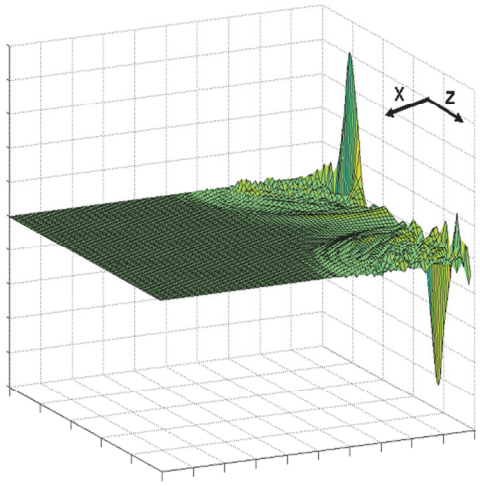

Fig. 6. v_1 field component of a line excitation of a SAW on the surface of the piezoelectric material.

However, by introducing a PML-terminated computational domain in Fig. 7(b), these spurious reflections are effectively removed, and are not reintroduced into the computational domain.

V. CONCLUSION

A matching condition is developed for the implementation of a perfectly matched layer for propagation of waves in piezoelectric materials. The new matching condition preserves the impedance matching criteria for all components of the stress and velocity fields. Coupled piezoelectric waves require a more elaborate matching condition to preserve the wave impedance in the PML region. We plan on further reducing the reflections by choosing PML grading optimized for all wave components.

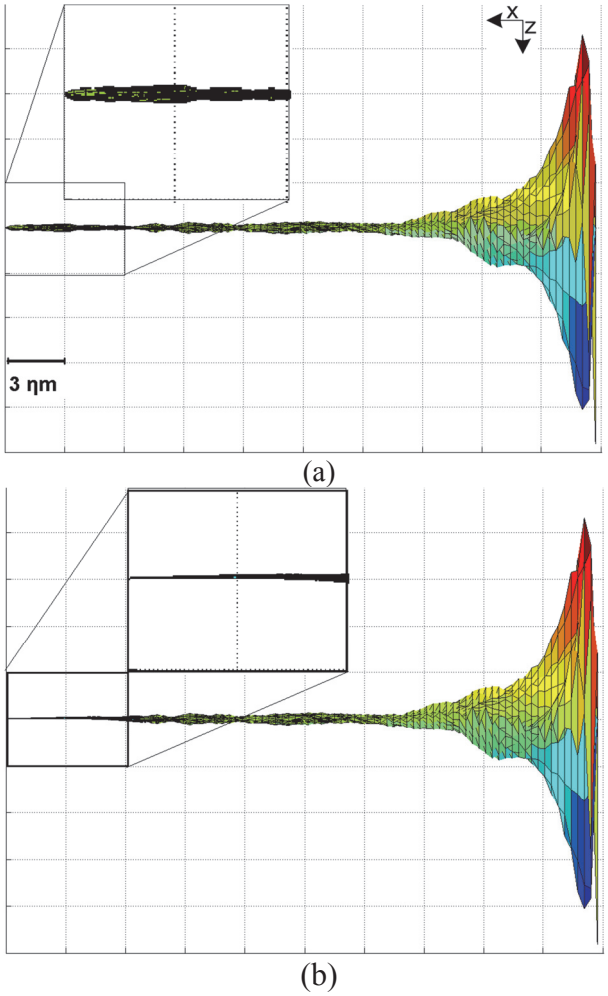

Fig. 7. Snapshots of the v_1 component of the acoustic waves inside the device (a) SAW and BAW generated in a medium without PML on the left boundary. (b) Same IDT excitation terminated with PML.

REFERENCES

[1] C. K. Campbell, Surface Acoustic Wave Devices for Mobile and Wireless Communications, Academic Press, New York, 1998.

[2] P. Ventura, J. M. Hode, M. Solal, J. Desbois, and J. Ribbe, "Numerical Methods for SAW Propagation Characterization," *IEEE Ultrasonics Symposium*, vol. 1, pp. 176-186, 1998.

[3] K. Y. Hashimoto, *Surface Acoustic Wave Devices in Telecommunications. Modelling and Simulation,* Springer, 2000.

[4] P. Ventura, J. M. Hode, and M. Solal, "A New Efficient Combined FEM and Periodic Green's Function Formalism for the Analysis of Periodic SAW Structures," *IEEE Ultrasonics Symposium*, vol. 1,pp. 263-268, 1995

[5] K. Y. Hashimoto, "Simulation of Surface Acoustic Wave Devices," *Jap. J. of App. Phys.*, vol. 45, no. 5B, pp. 4423-4428, 2006.

[6] K. Y. Hashimoto, T. Omori, and M. Yamaguchi, "Analysis of SAW Excitation and Propagation under Periodic Metallic Grating Structures," *International J. of High Speed Electronics and Systems*, Singapore, World Scientific Publishing, vol. 10, no. 3, pp. 685-734, 2000.

[7] C. C. W. Ruppel, W. Ruile, G. Scholl, K. C. Wagner, and O. Manner, "Review of Models for Low-Loss Filter Design and Applications," *IEEE Ultrasonics Symposium*, vol. 1, pp. 313-324, 1994.

[8] K. Y. Wong and W. Y. Tam, "Analysis of the Frequency Response of SAW Filters using Finite-Difference Time-Domain Method," *IEEE Trans. on Microwave Theory and Techniques*, vol. 53, no. 11, 2005.

[9] F. Chagla and P. Smith, "Finite Difference Time Domain Methods for Piezoelectric Crystals," *IEEE Trans. on Ultras. Ferroelec. and Freq. Cont.*, vol. 53, no. 10, 2006.

[10] J. P. Bérenger, "A Perfectly Matched Layer for the Absorption of Electromagnetic Waves," *J. of Computational Physics*, vol. 114, issue 2, pp. 185-200, 1994.

[11] R. Mittra and M. Kuzuoglu, "A Review of Some Recent Advances in Perfectly-Matched Absorbers for Mesh Truncation in FEM," *IEEE Antennas and Propagation Society International Symposium*, vol. 2, pp. 1302-1305, 1997.

[12] A. Taflove and S. C. Hagness, *Computational Electrodynamics: The Finite-Difference Time-Domain Method*, 2nd ed. Norwood, MA, Artech House, 2000.

[13] W. C. Chew and Q. H. Liu, "Perfectly Matched Layers for Elastodynamics: A New Absorbing Boundary Condition," *J. of Comp. Acoust.*, vol. 4, no. 4, pp. 341-360, 1996.

[14] J. P. Bérenger, Perfectly Matched Layer (PML) for Computational Electromagnetics, 1st ed., Morgan & Claypool, 2007.

[15] B. A. Auld, *Acoustic Fields and Waves in Solids*, 2nd ed., New York, Kruger Publishing Co., 1990.

Arthur Montazeri received his B.Eng. in Engineering Physics at McMaster University in 2004. He then joined the Department of Physics and Astronomy at McMaster University, as a Research Assistant studying the diffusion of macro-molecules in the dense cellular environment. He earned his M.A.Sc. degree in Electrical and Computer Engineering from McMaster University in 2010, and is currently a Ph.D. student at the ECE Department at McMaster University. His research interests include modeling physical media and wave propagation using numerical techniques, and studying novel approaches for high efficiency solar conversion systems.

Mohamed Bakr received a B.Sc. and M.Sc. degrees in Electronics and Communications Engineering and Engineering Mathematics from Cairo University, Egypt in 1992 and 1996, respectively with distinction (honors). From 1998 to 2000, he worked as a research assistant with the Simulation Optimization Systems (SOS) research laboratory, McMaster University, Hamilton, Ontario, Canada. He earned the Ph.D. degree in September 2000 from the Department of Electrical and Computer Engineering, McMaster University. In November 2000, he joined the Computational Electromagnetics Research Laboratory (CERL), University of Victoria, Victoria, Canada as an NSERC Post Doctoral Fellow. His research areas of interest include computer-aided design and modeling of microwave and photonic circuits, neural network applications, efficient optimization using time/frequency domain methods, and bioelectromagnetism. He is a main contributor to the theories of electromagnetic adjoint sensitivities and space mapping optimization. He is currently an associate professor with the Department of Electrical and Computer Engineering, McMaster University.

Yaser M. Haddara received a B.Eng. in Electrical Engineering from Memorial University of Newfoundland, St. John's, Newfoundland, in 1991, and an M.S. and Ph.D. from Stanford University, CA, in 1993 and 1997. He was a postdoctoral research associate at the University of Florida, Gainesville, FL, and was a Senior Engineer in the device group at Cypress Semiconductor. He is currently an Associate Professor in Electrical & Computer Engineering at McMaster University, Hamilton, Ontario and has been at McMaster since 2002. Dr. Haddara's research interests are in front-end silicon and silicon-germanium process modeling, nanowires growth and modeling technology CAD, and RF circuit design. His teaching interests are in microelctronics, device physics, process modeling, and probability and statistics.

Beam Scanning Antenna Using a Reflectarray as Sub-Reflector

Manuel Arrebola [1], Eduardo Carrasco [2], and Jose A. Encinar [2]

[1] Department of Electrical Engineering
Group of Signal Theory and Communications
Universidad de Oviedo, Gijón (Asturias) 33203, Spain
arrebola@tsc.uniovi.es

[2] Department of Electromagnetism and Circuit Theory
Universidad Politécnica de Madrid, Madrid 28040, Spain
carrasco@etc.upm.es, encinar@etc.upm.es

Abstract ─ In this paper, a dual-reflector antenna based on a main parabolic reflector and a reconfigurable reflectarray as subreflector is proposed for beam scanning applications. The beam deflecting is achieved by modifying the phase introduced by each element of the subreflectarray. The required phase distribution for each scan angle is obtained through a synthesis technique based on the analysis of the antenna in receive mode. The design technique has been applied to the particular cases of beam scanning in azimuth and elevation planes. Patches aperture-coupled to delay lines, which provide low losses and cross-polar levels, are proposed as elements for the reflectarray subreflector, allowing the easy implementation of electronic control devices in the microstrip delay lines. The results show that the beam can be scanned in a range ±6º by inserting switches on the delay line to provide a 3-bit quantization.

Index Terms ─ Beam scanning, dual-reflector antenna, reconfigurable antenna, reflectarray.

I. INTRODUCTION

Antennas with beam scanning capabilities are required in a number of applications, as radar, emergency communications, or earth observation from space missions, [1-2]. Usually, these applications also require high gain antennas (narrow beams). Different solutions have been proposed, based either on mechanic, electronic, or hybrid mechanic-electronic scanning of the beam [3-23]. Lenses [3], reflector antennas [4-6], phased arrays [7-12], reflectarrays [13-20], and array fed reflectors [21-23] have been studied and proposed as solutions for beam steering applications requiring a narrow beam. The solutions based on lenses usually imply the use of mechanic devices [3]. The motion of the antenna components can be reduced by the use of complex antenna optics based on three reflectors [4]. Mechanic scanning options are not optima in terms of volume, mass and power consumption, being preferred electronic beam scanning. Beam steering can also be achieved by feeding the reflector by a horn array and using two shaped reflectors [5-6]. However, the cost of a shaped reflector manufacture process is high because of the moulds. Two possibilities for achieving electronic beam scanning are phase-arrays and reflectarrays. Phased arrays have been used as reconfigurable and wide angle beam steering antennas [7-8]. The reconfiguration of the beam is achieved by introducing active elements [9]. Combined electronic and mechanic beam control is proposed for applications with stringent scanning requirements [10]. Conventional phased arrays with large apertures would require transmit-receive (T/R) modules due to the losses of the feeding network [7], requiring very complex control circuitry [11-12]. On contrary, reflectarray is spatially fed, without any feeding network, and the ohmic losses are much lower than in phased arrays. Then, reflectarrays can provide a low-cost low-complexity solution for beam scanning by

simply inserting low-loss phase-shifters in each element [13-16]. Some recent works have shown different implementations for phase control in reflectarray antennas, based on electronic devices as MEMS or diodes [17-20].

If high gain and electronic reconfigurability or scanning of the beam is required, a dual-reflector antenna with an electronically controllable reflectarray subreflector can be used (see

Fig. 1). Reflectors with an array as feed have been proposed for beam steering applications [21-23]. Different optics have been proposed for this configuration, including single parabolic [21] or spherical [22] reflectors and Cassegrain dual reflectors configurations [23]. These options reduce the complexity, mass, volume, and power consumption of the control circuitry compared to a large reconfigurable phased array. However, the array as feed solution exhibits the same inconveniences as single phased arrays: transmit-receive (T/R) modules and complex feeding networks are required. The capability of a subreflectarray–main parabolic reflector configuration for beam scanning has been demonstrated for a passive reflectarray [24], where the beam was deflected by introducing a progressive phase along the y-axis of the subreflectarray, according to Fig. 1. However, the results in [24] showed that the beam suffered also a slight deflection in the vertical direction, because the reflectarray subreflector was tilted. To avoid this problem, a more elaborate phase-synthesis is required to provide beam scanning, than simply introducing a progressive phase on the sub-reflectarray.

A phase-synthesis technique is proposed in this paper to provide beam scanning in a dual-reflector configuration using a reflectarray subreflector. The synthesis technique has been applied to design a dual-reflector antenna for beam scanning in the principal planes at 11.7GHz. After defining the geometry and elements of the antenna, the beam scanning performance is evaluated.

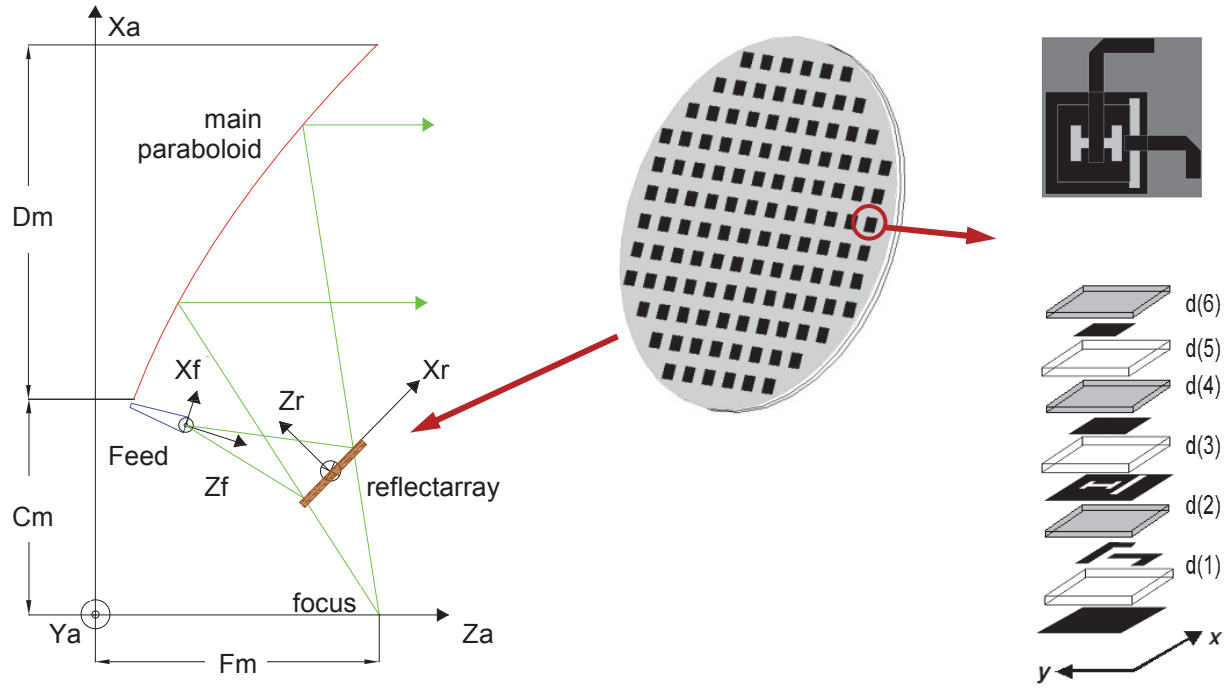

Fig. 1. Scheme of the dual-reflector configuration.

II. ANALYSIS AND SYNTHESIS TECHNIQUES

A scheme of the configuration of the antenna is shown in

Fig. 1, which includes three main elements: a primary feed (horn antenna), a reflectarray as subreflector, and a main parabolic reflector.

A. Antenna analysis

The antenna analysis technique is described in [25]. It combines several techniques for the analysis of the different elements of the antenna. For simplicity, an ideal feed-horn model based on $\cos^q(\theta)$ function is used. However, the near-field of the primary feed, obtained from measurements or full-wave simulations, can be used [26]. The elements of the subreflectarray are analyzed through a convenient full-wave tool, considering local periodicity and the real incidence angle of the wave coming from the feed. Once the field reflected by the elements of the subreflectarray has been obtained, the parabolic reflector is analyzed through physical optics (PO).

The far field produced by each reflectarray element, considered as a small rectangular aperture, is used to compute the PO printed currents on the parabolic surface. The equivalent currents on the main reflector are computed by adding the contributions from all the elements of the reflectarray, and the final illumination (amplitude and phase of the incident field) on the parabolic surface depend on the phase-shift introduced by the reflectarray cells. Finally, the radiation pattern is computed using an FFT-based algorithm, which is applied to the electric field on the antenna aperture. This technique has been validated by comparing the simulated and measured radiation patterns of a breadboard in the 94GHz band, see [24].

In this antenna, the beam is deflected by adjusting only the phase-shift on the reflectarray elements. Note that the amplitude is not changed on the reflectarray subreflector, except for small variation in the ohmic losses. However, the resulting illumination on the main reflector is different for each scan angle, because the currents induced by all the reflectarray cells are superposed.

B. Phase synthesis for beam scanning

A technique based on PO is applied to synthesize the required phase distribution on the reflectarray subreflector for a required scan angle. The synthesis is carried out by analyzing the antenna in receive mode, as in [27]. In a receiving antenna, the incident field is a plane wave that propagates in a direction forming an angle with the paraboloid Z_a-axis, see Fig. 1. In a dual reflector antenna, the incident wave defines an electric field distribution on the antenna aperture (the flat surface defined by the reflector edge) with a progressive phase according to the incidence angle. Then, the inverse process to that used for the analysis of the transmitting antenna is carried out. First, the PO currents on the reflector surface are calculated. Second, the incident electric field on each element of the subreflectarray produced by the printed currents in the main reflector is computed, being the phase of this field retrieved on each reflectarray element (m,n) denoted as $\phi_{retr}(m,n)$. The phase of the field reflected by the reflectarray in receive mode will be:

$$\phi_{RA}(m,n)+\phi_{retr}(m,n), \qquad (1)$$

where $\phi_{RA}(m,n)$ is the phase-shift introduced by the reflectarray element (m,n). The fields reflected on all the elements (m,n) should converge to the focal point where the feed is located, after propagating along the corresponding paths. This propagation produces the phase delay $\phi_{feed}(m,n)$ from the element (m,n) to the feed. By reciprocity, $\phi_{feed}(m,n)$ is the same phase of the incident field on the reflectarray element (m,n) coming from the feed when the antenna is in transmit mode. Therefore, assuming the antenna in reception mode, the condition to concentrate all the signals to the focal point when a field is received from a given scan angle, is:

$$\phi_{RA}(m,n)+\phi_{retr}(m,n)+\phi_{feed}(m,n)=C, \qquad (2)$$

where C is a constant. Then, the required phase-shift on the reflectarray elements $\phi_{RA}(m,n)$ is:

$$\phi_{RA}(m,n)=-\left(\phi_{feed}(m,n)+\phi_{retr}(m,n)\right)+C. \qquad (3)$$

Finally, the phase-shift $\phi_{RA}(m,n)$ has to be implemented in each reflectarray element. If a discrete phase control is used, the phase shift at each reflectarray cell will be approximated by a finite number of phase values, defined by

$$\phi_{RA}'(m,n) = (p-1)\frac{\pi}{2^{k-1}}, \qquad p \in \mathbb{N}\left[1, 2^k\right], \tag{4}$$

where k is the number of control bits in each element and a uniform quantization is assumed. Thus, the value of the phase $\phi_{RA}'(m,n)$ is chosen at each cell (m,n) to minimize the phase error.

III. RESULTS

A. Antenna definition

A general scheme of the dual-reflector antenna is shown in

Fig. 1. The antenna geometry is defined by the parameters given in Table 1. The design and analysis is carried out at 11.7GHz. In this antenna, the main parabolic reflector is oversized in order to obtain beam deflecting without significant reduction in the gain because of spillover. Note that the change in beam pointing is obtained by scanning the illumination on the main reflector surface. The antenna optics has been defined to fulfill two conditions. First, a beam in the boresight direction should be obtained when the phase-shift is constant along the subreflectarray surface. Second, the beam is scanned in a ±6degree range both in elevation and in azimuth without subreflector blockage. As shown in Table 1, the reflectarray is elliptical with 24 and 22 elements along X_R and Y_R axis, respectively. Considering that the size of the reflectarray cell is 12.5mm × 12.5mm, the axes of the resulting surface are 300mm and 275mm. In this case, the reflectarray is illuminated with a taper at edges of -10dB. The radiation patterns of the boresight beam have been computed on the principal planes considering an ideal phase distribution for dual linear polarization, see Fig. 2. The computed antenna gain is 35.8 dBi. According to the antenna optics, the spillover efficiency is quite high, ε_s=0.81. However, the oversized main reflector produces a low aperture efficiency, ε_t =0.31, being the antenna efficiency the product of the two terms, $\varepsilon=\varepsilon_s*\varepsilon_t$=0.25.

Table 1: Main parameters of the antenna

Parabolic Reflector	
Aperture diameter (Dm)	989mm
Clearance (Cm)	595mm
Focal Distance (Fm)	792mm
Subreflectarray	
Center	(390, 0, 640)mm
Periodic cell size	12.5mm×12.5mm
Reflectarray size	24 × 22 elements
Direction cosines	$\begin{pmatrix} \sqrt{2}/2 & 0 & \sqrt{2}/2 \\ 0 & -1 & 0 \\ \sqrt{2}/2 & 0 & -\sqrt{2}/2 \end{pmatrix}$
Feed-horn *(in Sub-RA coordinate system)*	
Phase center	(-174, 0, 375)mm
Pointing	(0, 0, 0)mm

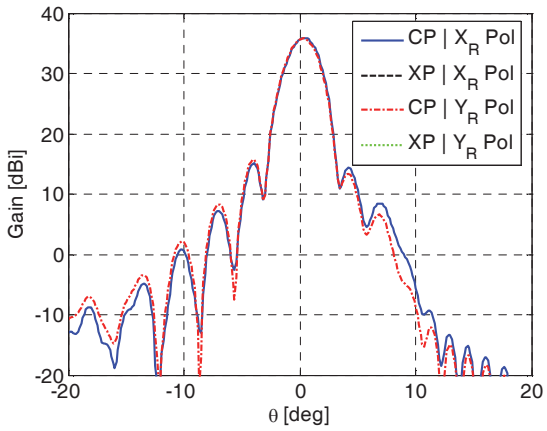

(a)

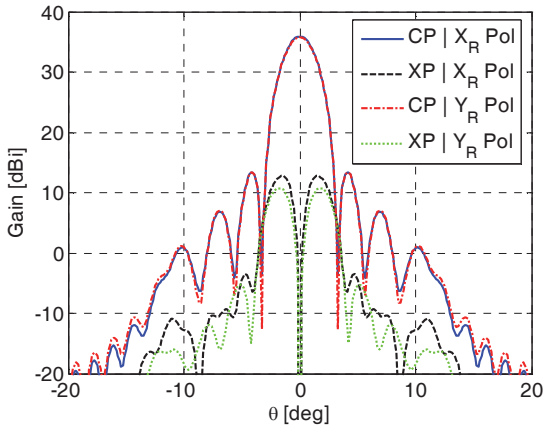

(b)

Fig. 2. Radiation pattern of the boresight beam. Main cuts in elevation (a) and azimuth(b).

B. Sub-reflectarray periodic cell definition

The proposed reflectarray element is based on the patches aperture-coupled to delay lines, as that shown in Fig. 3 and can be used for dual linear polarization. With the aim of providing a broadband element, two square patches have been stacked (dimensions of the upper patch are scaled by a factor of 0.68 with respect those of the lower patch which is 8.0mm × 8.0mm). The room restriction for placing the two slots has been solved using an H-shaped slot for the X-polarization (the width of all the branches is 0.8 mm, the main branch length is 4mm and the secondary branches length is 2.8mm), while a rectangular slot is used for the Y-polarization (0.8mm × 7mm). The width of both delay lines is 1.18 mm. The period for the element has been fixed to 12.50mm×12.50mm, while the dielectric materials used in the design are summarised in Table 2.

These elements exhibits very low cross polarization levels and allow the implementation of electronic phase control devices, as MEMS [28] or diodes [29]. Because of the presence of the ground plane, the electronic switches and their control network are on the opposite side of the radiating patches, avoiding spurious radiation. Fig. 3(c) shows one option for implementing series switches between different segments of the microstrip line, allowing a change in the length of the delay line and therefore a variation in the phase of the reflected wave, [30].

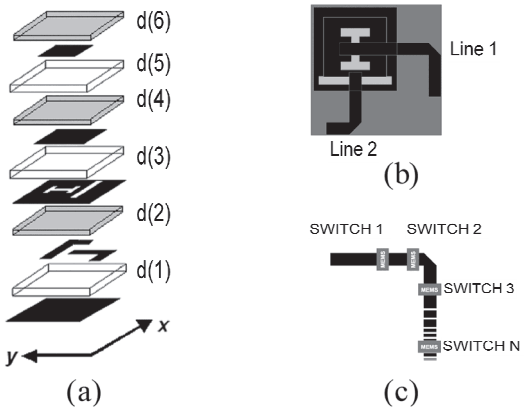

Fig. 3. Dual-polarization reflectarray element based on patches aperture-coupled to delay lines. (a) Expanded view. (b) Upper view. (c) Implementation of series switches in the delay line.

Fig. 4(a) and (b) show respectively the phase and amplitude response of the element when a plane wave with the electric field oriented in the X-axis direction impinges on top of the element. The surfaces have been generated as a function of both line lengths using the frequency domain solver of CST Microwave Studio® [31] with Floquet conditions. The element has been analyzed for an incident field impinging at an angle $\theta=\varphi=30^{\circ}$, assuming that for smaller angles the cross-polar component will be lower. As can be seen, in all the cases the average losses produced at 11.70 GHz are around 0.2 dB.

For X-polarization, the phase is practically a linear function of the delay line L1 (for different values of the second delay line, L2), as shown in Fig. 4(c). These phases are compared with that produced by an ideal phase-shifter where the phase is equal to $-2\beta L$, being β the propagation constant for the microstrip line, at the working frequency of 11.70GHz, and L the length of the delay line. More than 360º of phase delay can be obtained if the line is bent, allowing true-time delay (TTD) [32]. The average cross-polar levels are better than –25 dB, except for the length L1=5.8 mm, where increases until –18 dB, as can be seen in Fig. 4(d). The phase response of this element remains very similar for incidence angles up to $\theta=30^{\circ}$, with variation in phase smaller than 30º. As a first approach, the subreflectarray can be designed considering the data from normal incidence, however the real angles of incidence should be taken into account for a more accurate design.

The electronic control implementation in these kinds of elements has been previously validated with PIN diodes [33] and MEMS devices [28].

Table 2: Dielectric slabs values

Layer	**d(1)**	**d(2)=d(4)=d(6)**	**d(3)=d(5)**
Material	Vacuum	Arlon	Eccostock
thickness (mm)	6.400	0.508	1.000
ε_r	1.0054	3.3800	1.0400

tanδ	0.0002	0.0035	0.0010

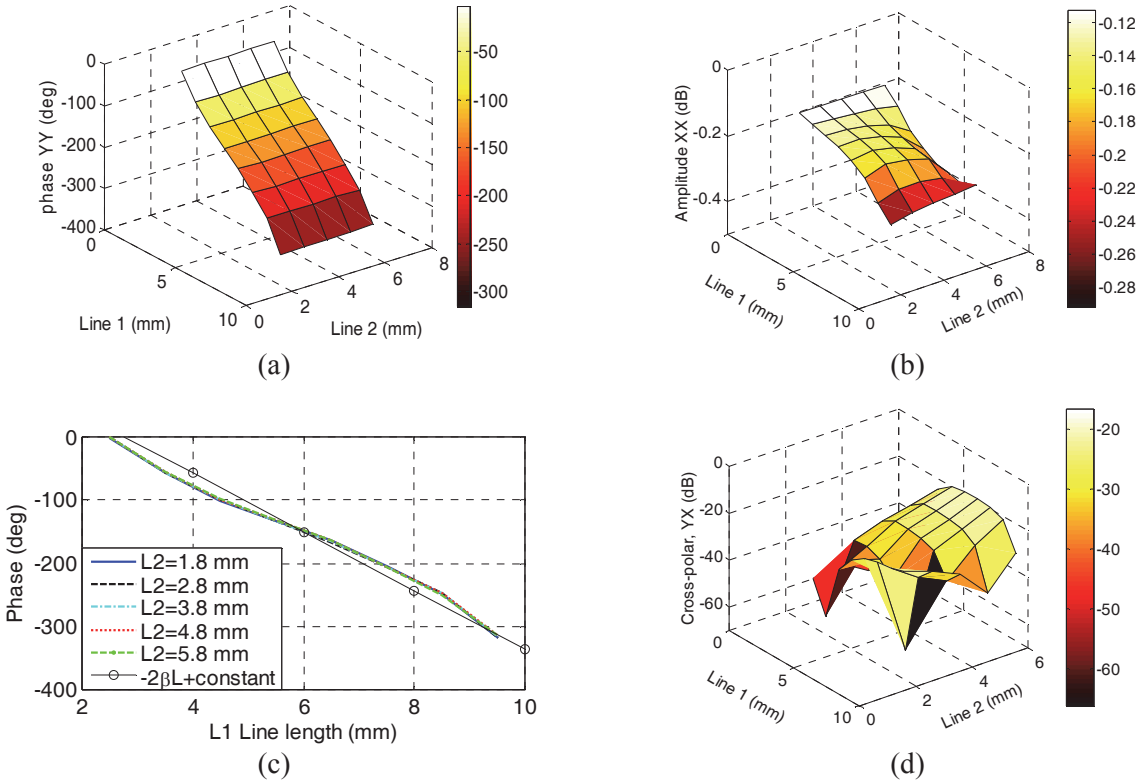

Fig. 4. Response for the proposed reflectarray element, at 11.70 GHz, when impinges an X-polarization plane wave. (a) Copolar phase response. (b) Losses. (c) Phase cut as a function of line L1. (d) Amplitude of the cross-polar component.

C. Beam scanning performance

For the antenna geometry under study, the phase distribution has been synthesized on the subreflectarray for two scan angles and the antenna is analyzed considering X_R polarization according to

Fig. 1 shows that the first case corresponds to the synthesis of a beam deflected –6 degrees in elevation. The phase distribution obtained by equation (3) is shown in Fig. 5(a). These phases are introduced in the analysis tool to compute first the electric field on the antenna aperture and then, the radiation pattern of the entire antenna. The amplitude and phase of the electric field on the antenna aperture are shown in Fig. 5(b) and (c), respectively. According to these results, the beam deflecting is achieved by scanning the field coming from the subreflectarray on the main reflector surface. The progressive phase is not obtained along the entire aperture of the antenna, see Fig. 5(c). However the required phase is achieved in the area with high illumination level, see Fig. 5(b) and (c), and therefore the beam is satisfactorily scanned. The zone of the aperture with low illumination will introduce a small distortion in the radiation pattern.

The second case corresponds to a beam scanned in the orthogonal dimension: +6 degrees in azimuth. As in the previous case, the required phase distribution on the subreflectarrray surface is first obtained and then introduced in the model to compute the electric field at the antenna aperture, see Fig. 6. Now, the illumination is scanned along the azimuth direction as shown in Fig. 6(b). As in the former case, the suitable progressive phase is achieved on the area of the antenna aperture with significant illumination level, see Fig. 6(b) and (c). Note that in this case the required phase-shift distribution shows some variation along the X_{RA} axis according to Fig. 6(a). The reason for this result is that the subreflectarray is tilted. If a progressive phase would be introduced along the Y_{RA} axis (with no variation on the orthogonal direction), the scanned beam

will suffer a slight deflection in the vertical dimension, as shown in [24].

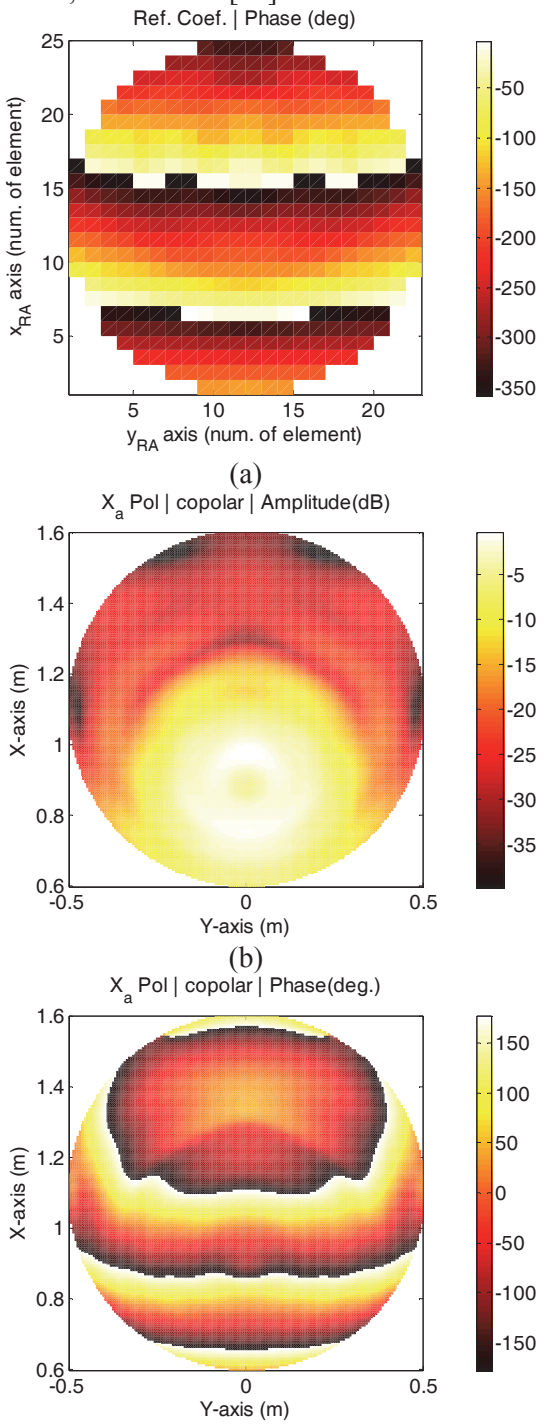

Fig. 5. Case of –6 degree deflected beam in elevation with continuous phase-shift control. (a) Required phase shift of the sub-reflectarray. (b) Amplitude and (c) phase of the electric field at the antenna aperture.

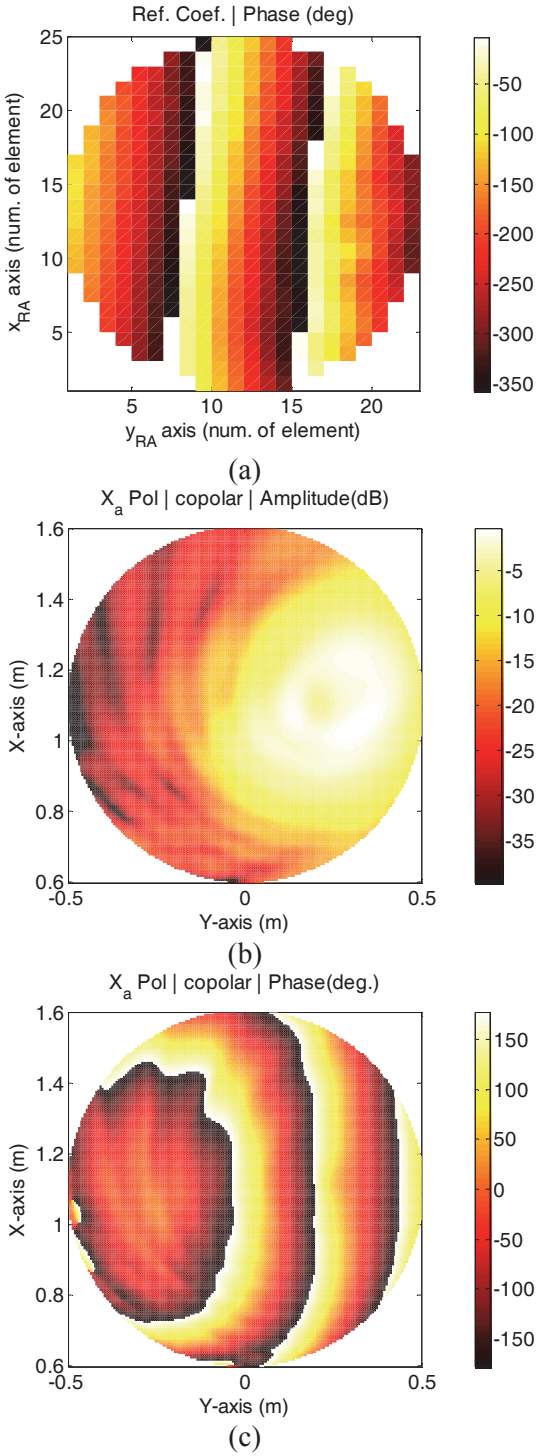

Fig. 6. Case of +6 degree deflected beam in azimuth with continuous phase-shift control. (a) Required phase shift of the sub-reflectarray. (b) Amplitude and (c) phase of the electric field at the antenna aperture.

The radiation patterns are computed for the two cases studied and they are compared with the case of the beam in the boresigth direction. The main cuts of the patterns, elevation and azimuth, are plotted in Fig. 7. A small reduction in gain with respect to the boresight beam is observed, 1dB in both cases, because of the reduction in the spillover efficiency. For the scanned beams, the spillover and aperture efficiencies are 0.7 and 0.29 respectively, being the total antenna efficiency 0.2. Note that the aperture efficiency is slightly lower than that obtained for the case of the beam in the boresight direction (0.31). In the case of the scanning in the azimuth plane, the cross-polar level is strongly increased (-14dB) since on the sub-reflectarray the beam is scanned out of the symmetry planes.

For a practical electronic control of the phase on the subreflectarray, the number of phase states is imposed by the number of control bits. Therefore, the phase distribution is quantized assuming n-bit control according to equation (4). In this case, 3-bit control is considered (eight phase states at each element). The discrete phase control implies a reduction in the degrees of freedom and some distortion in the radiation patterns is produced. The phase distribution for the case of +6degree deflected beam in azimuth and considering 8-level phase quantification is shown in Fig. 8. The corresponding radiation patterns obtained with these phase distributions are plotted in Fig. 9, showing a small distortion with respect to those assuming a continuous phase control, see Fig. 7.

The results have been obtained considering vertical polarization (X_a polarization), being the performance very similar for the orthogonal polarization.

IV. CONCLUSION

A dual-reflector antenna based on a reconfigurable reflectarray as subreflector has been presented as a solution for beam scanning applications that require high gain and narrow beams. In this antenna, the beam gain is obtained by a passive large parabolic reflector while the beam deflecting control is achieved by a small planar subreflectarray. The subreflectarray elements are based on printed patches aperture-coupled to delay lines where electronic control elements can be implemented. A synthesis technique, which is based on the analysis of the antenna in receive mode, has been applied to determine the phase-shift distribution on the subreflectarray surface for producing a given scanning angle. To validate the synthesis technique, an antenna has been defined at 11.7GHz and the beam scanning capabilities in both elevation and azimuth planes have been evaluated.

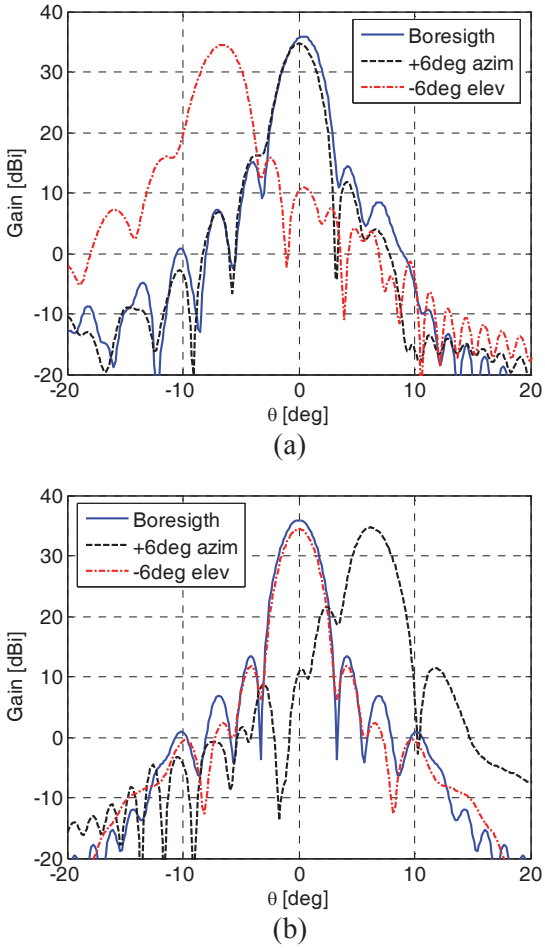

Fig. 7. Radiation patterns of different cases of scanned beams assuming continuous phase-shift control. Main cuts in (a) elevation and (b) azimuth.

ACKNOWLEDGMENT

This work has been supported in part by the "Ministerio de Ciencia e Innovación" (Spanish Government) under projects TEC2010-17567, TEC2008-01638 and CONSOLIDER-INGENIO CSD2008-00068 (TERASENSE).

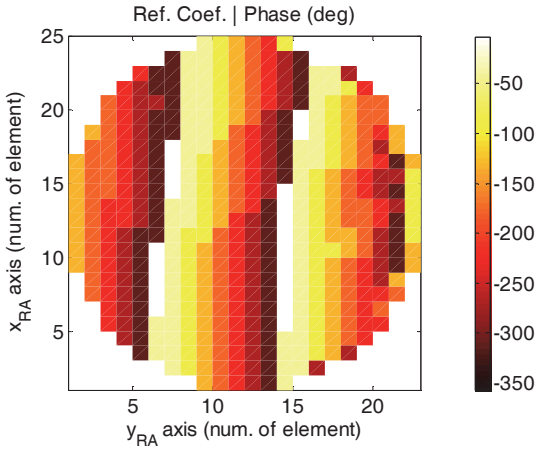

Fig. 8. Case of 3-bit phase-shift control. Required phase-shift for a beam deflected +6 degree in azimuth.

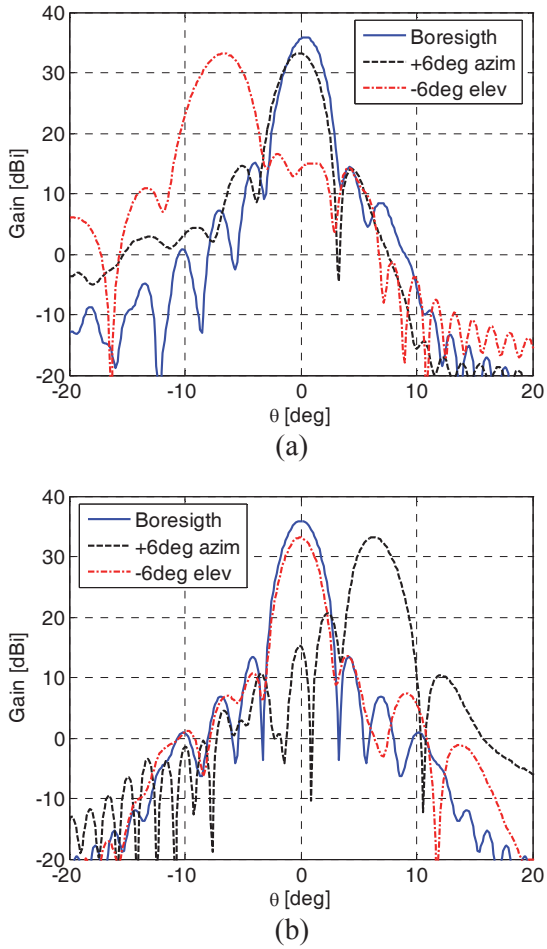

Fig. 9. Radiation patterns of different cases of scanned beams assuming 3-bit discrete phase-shift control. Main cuts in (a) elevation and (b) azimuth.

REFERENCES

[1] U. Frisk, M. Hagström, J. Ala-Laurinaho, S. Andersson, J. C. Berges, J. P. Chabaud, M. Dahlgren, A. Emrich,G. Floren, G. Florin, M. Fredrixon, T. Gaier, R. Haas, T. Hirvonen, A. Hjalmarson, B. Jakobsson, P. Jukkala, P.-S. Kildal, E. Kollberg, J. Lassing, A. Lecacheux, P. Lehikoinen, A. Lehto, J. Mallat, C. Marty, D. Michet, J. Narbonne, M. Nexon, M. Olberg, H. Olofsson, G. Olofsson, A. Origne, M. Petersson, P. Piirone, D. Pouliquen, I. Ristorcelli, C. Rosolen, G. Rouaix, A. V. Raisanen, G. Serra, F. Sjoberg, L. Stenmark, S. Torchinsky, J. Tuovinen, C. Ullberg, E. Vinterhav, N. Wadefalk, H. Zirath, P. Zimmermann, and R. Zimmermann, "The Odin satellite: I: Radiometer Design and Test.," *Astron Astrophys., A&A*, vol. 402, pp. L27-L34, 2003.

[2] M. Oldfield, B. Moynaa, E. Allouisa, R. Bruntb, U. Cortesid, B. Ellisona, J. Eskellc, T. Forwardc, T. Jonesa, D. Lamarree, J. Langene, P. de Maagte, D. Mathesona, I. Morganb, J. Reburna, R. Siddansa, "MARSCHALS: Development of an Airborne Millimetre-Wave Limb Sounder," *Proc. 8th Int. Symp. on Remote Sensing, SPIE*, vol. 4540, pp. 221-228, 2001.

[3] J. Qiu, W. Li, and Y. Suo, "A Novel High Gain Beam Scanning Hemispherical Dielectric Lens Antenna," *6th Int. Conf. on ITS Telecommunications Proc.,* Chengdu, China, pp. 21-23, June 2006.

[4] P. C. Werntz, W. L. Stutzman, and K. Takamizawa, "A High-Gain Trireflector Antenna Configuration for Beam Scanning," *IEEE Trans. Antennas Propagat.*, vol. 42, no. 9, pp. 1205-1213, Sep. 1994.

[5] C. M. Rappaport, "An Offset Bifocal Antenna Design for Wide-Angle Beam Scanning," *IEEE Trans. Antennas Propagat.*, vol. AP-32, pp. 1196-1204, Aug. 1984.

[6] V. Galindo-Israel, W. Veruttipong, R. D. Norrod, and W. A. Imbriale, "Scanning Properties of Large Dual-Shaped Offset and Symmetric Reflector Antennas," *IEEE Trans. Antennas Propagat.*, vol. 40, no. 4, pp. 422-432, April 1992.

[7] R. C. Hansen, *Phased Array Antennas,* Wiley-Interscience, 1998.

[8] P. F. McManamon, P. J. Bos, M. J. Escuti, J. Heikenfeld, S. Serati, H. Xie, and E. A. Watson, "A Review of Phased-Array Steering for Narrow-Band Electrooptical Systems," *Proc. of the IEEE,* vol. 97, pp. 1078-1096, June 2009.

[9] R. J. Pogorzelski, "A 5-by-5 Element Coupled Oscillator-Based Phased Array," *IEEE Trans. Antennas Propagat.*, vol. 53, no. 4, pp. 1337-1345, April 2005.

[10] A. A. Tolkachev, V. V. Denisenko, A. V. Shishlov, and A. G. Shubov, "High Gain Antenna Systems for Millimeter Wave Radars with Combined Electronical and Mechanical Beam Steering," *IEEE Int. Symp. on Phased Array Systems and Technology, 1996,* Boston, MA. 15-18 Oct. 1996.

[11] G. W. Kant, P. D. Patel, S. J. Wijnholds, M. Ruiter, and E. van der Wal, "EMBRACE: A Multi-Beam 20000-Element Radio Astronomical Phased Array Antenna Demonstrator," *IEEE Trans. Antennas Propagat.,* In Press, 2011.

[12] W. Gerlitzki, "A Development Line in Radar from Telefunken to EADS", EADS Deutschland Defence Electronics, 2004.

[13] J. Huang and J. A. Encinar, *Reflectarray Antennas,* Wiley Interscience, 2008.

[14] M. Riel, J.-J. Laurin, "Design of an Electronically Beam Scanning Reflectarray Using Aperture-Coupled Elements," *IEEE Trans. Antennas Propagat.*, vol. 55, no. 5, pp. 1260-1266, May 2007.

[15] S. R. Rengarajan, "Scanning and Defocusing Characteristics of Microstrip Reflectarrays," *IEEE Antennas Wireless Propagat. Let.*, vol. 9, pp. 163-166, 2010.

[16] W. Menzel, D. Pilz, and M. Al-Tikriti, "Millimeter-Wave Folded Reflector Antennas with High Gain, Low Loss and Low Profile", *IEEE Antennas Propagat. Mag.*, vol. 44, no. 3, pp. 24-29, June 2002.

[17] B. Mencagli, R. Vincenti Gatti, L. Marcaccioli, and R. Sorrentino, "Design of Large Mm-Wave Beam-Scanning Reflectarrays," *35th EuMC,* Paris, France, 3-7 Oct. 2005.

[18] M. Barba, E. Carrasco, and J. A. Encinar, "Recent Developments in Reconfigurable X-Band Reflectarray Elements Using MEMS", *10th International Symposium on RF-MEMS and RF Microsystems, MEMSWAVE 2009,* Trento, Italy, 6-8 July 2009.

[19] R. Sorrentino, "MEMS-Based Reconfigurable Reflectarrays," Proc. *2nd European Conf. Antennas Propagat. – EuCAP 2007,* Edinburgh, UK, 12-16 Nov. 2007.

[20] J. Y. Lau and S. V. Hum, "A Planar Reconfigurable Aperture with Lens and Reflectarray Modes of Operation," *IEEE Trans. Antennas Propagat.*, vol. 58, no. 12, pp. 3547-3555, Dec. 2010.

[21] R. M. Davis, C.-C. Cha, S. G. Karnak, and A. Sadigh, "A Scanning Reflector Using an Off-Axis Space-Fed Phased-Array Feed," *IEEE Trans. Antennas Propagat*., vol. 39, pp. 391-400, March 1991.

[22] K. Bahadori and Y. Rahmat-Samii, "An Array-Compensated Spherical Reflector Antenna for a Very Large Number of Scanned Beams," *IEEE Trans. Antennas Propagat*., vol. 53, pp. 3547-3555, Nov. 2005.

[23] Y.-B. Jung, A. V. Shishlov, and S.-O. Park, "Cassegrain Antenna with Hybrid Beam Steering Scheme for Mobile Satellite Communications," *IEEE Trans. Antennas Propagat*., vol. 57, pp. 1367-1372, May 2009.

[24] W. Hu, M. Arrebola, R. Cahill, J. A. Encinar, V. Fusco, H. Gamble, Y. Álvarez, and F. Las-Heras, "94 GHz Dual-Reflector Antenna with Reflectarray Sub-Reflector," *IEEE Trans. Antennas Propagat.*, vol. 57, no. 10, part 2, pp. 3043-3050, Oct. 2009.

[25] M. Arrebola, L. de Haro, and J. A. Encinar, "Analysis of Dual-Reflector Antennas with a Reflectarray as Subreflector," *IEEE Antennas Propag. Mag.*, vol. 50, no. 6, pp. 39-51, Dec. 2008.

[26] M. Arrebola, Y. Álvarez, J. A. Encinar, and F. Las-Heras, "Accurate Analysis of Printed Reflectarrays Considering the Near Field of the Primary Feed," *IET Microwave, Antennas and Propagation*, 2008, vol. 3, no. 2, pp. 187-194, March 2009.

[27] W. Menzel, M. Al-Tikriti, and R. Leberer, "A 76 GHz Multiple-Beam Planar Reflector Antenna," *32nd European Microwave Conference*, Oct. 2002.

[28] E. Carrasco, M. Barba, B. Reig, J. A. Encinar, and P. L. Charvet, "Demonstration of a Gathered Element for Reconfigurable-Beam Reflectarrays Based on Ohmic MEMS", *5th*

European Conference on Antennas and Propagation, EuCAP 2011, Rome, Italy, 11-16 April 2011.

[29] E. Carrasco, M. Barba, and J. A. Encinar, "Switchable-Beam Reflectarray With Aperiodic-Gathered Elements Based on PIN Diodes," *32nd ESA Antenna Workshop on Antennas for Space Applications*, European Space Agency, Noordwijk, The Netherlands, 5-8 October 2010.

[30] E. Carrasco, J. A. Encinar, M. Barba, R. Vincenti, and R. Sorrentino, "Dual-Polarization Reflectarray Elements for Ku-Band Tx/Rx Portable Terminal Antenna", Proc. *4th European Conf. Antennas Propagat. – EuCAP,* Barcelona, Spain, 12-16 Apr. 2010.

[31] CST Microwave Studio®, www.cst.com.

[32] E. Carrasco, J. A. Encinar, and M. Barba, "Bandwidth Improvement in Large Reflectarrays by Using True-Time Delay," *IEEE Trans. Antennas Propagat*., vol. 56, pp. 2496-2503, Aug. 2008.

[33] M. Barba, E. Carrasco, J. E. Page, and J. A. Encinar, "Electronic Controllable Reflectarray Elements in X Band," *Frequenz Mag.*, no. 9, October 2007.

Manuel Arrebola was born in Lucena (Córdoba), Spain. He received the Ingeniero de Telecomunicación degree from Universidad de Málaga (UMA) in 2002, and the Ph.D. degree from the Universidad Politécnica de Madrid (UPM) in 2008.

From 2003 to 2007, he was with the Department of Electromagnetism and Circuit Theory, UPM, as a Research Assistant. From August to December 2005, he was with the Institute of Microwave Techniques at the Universität Ulm, Germany, as a Visiting Scholar. In 2009 he enjoyed a two month stay at the Antenna Section of European Space Agency (ESA). In December 2007, he joined the Electrical Engineering Department at the Universidad de Oviedo, Spain, where he is an Associate Professor. His current research interests include analysis and design techniques of printed reflectarrays in single and dual-reflector configurations and planar antennas.

Eduardo Carrasco was born in Mexico City. He received the Telecommunication Engineer degree from the Universidad Nacional Autonoma de Mexico (UNAM), Mexico in 2000, and the Telecommunication Ph.D. degree from the Universidad Politecnica de Madrid (UPM), Spain, in 2008.

From 1999 to 2001, he was with Directv Latin America as Broadcast Operation System Specialist. In 2002, he received a grant from Fundacion Vodafone, Spain, to obtain a Telecommunication Management Degree at Escuela de Organizacion Industrial (EOI), Spain. From January to April 2008, he visited the Microwave Engineering Laboratory at the Universita degli Studi di Perugia, Perugia, Italy. Since 2009, Dr. Carrasco is with the Electromagnetism and Circuits Theory Department at Universidad Politecnica de Madrid (UPM), Spain, as Postdoctoral Researcher. His current research interests include reconfigurable-beam reflectarrays, multilayer periodic structures and space antennas.

Jose A. Encinar was born in Madrid, Spain. He received the Electrical Engineer and Ph.D. degrees, both from Universidad Politécnica de Madrid (UPM), in 1979 and 1985, respectively.

Since January 1980, has been with the Applied Electromagnetism and Microwaves Group, UPM, as a Teaching and Research Assistant from 1980 to 1982, as an Assistant Professor from 1983 to 1986, and as Associate Professor from 1986 to 1991. From February to October 1987, he was with Polytechnic University, Brooklyn, NY, as a Postdoctoral Fellow of the NATO Science Program. Since 1991, he is a Professor of the Electromagnetism and Circuit Theory Department, UPM. In 1996, he was with the Laboratory of Electromagnetics and Acoustics, Ecole Polytechnique Federale de Lausanne (EPFL), Switzerland, as a Visiting Professor. His research interests include numerical techniques for the analysis of multilayer periodic structures, design of frequency selective surfaces, printed arrays and reflectarrays.

Application of the Wheeler Incremental Inductance Rule for Robust Design and Modeling of MMIC Spiral Inductors

Grant A. Ellis

Department of Electrical and Electronic Engineering
Universiti Teknologi Petronas, 31750 Tronoh, Perak Darul Ridzuan, Malaysia
grant_ellis@petronas.com.my

Abstract ─ A physics based model using Wheelers incremental inductance rule for calculating the change in inductance due to variations in line width and thickness for planar circular spiral inductors is given. It is shown that the series resistance of an MMIC inductor can be used as a figure of merit for the robustness of the inductor against etching variations in line width during fabrication. Circular inductors are shown to have less inductance variation than rectangular inductors. This model can be evaluated quickly using a circuit simulator without the need for expensive EM analysis. In the electromagnetic modeling of MMIC inductors, a fine grid and several sheets are used to accurately model the current distribution and determine the resistance. Sonnet^{TM} is used to accurately model the 3D characteristics of thick conductors such as loss and effects of physically thick metal. A procedure based on the Richardson extrapolation method is used to extract the resistance values without long computation time. Applications include calculating the change in inductance due to over- or under-etching of metal lines during fabrication. For 2 to 4 turn inductors with variations in line width of +/-20% of the nominal width, the average variation in modeled inductance is within 8% of the EM simulated variation.

Index Terms - Microwave components, MMIC technology, planar inductors.

I. INTRODUCTION

During fabrication of the MMIC inductors, variations in line width or line thickness may occur. This can be due to variations in the etch rates during wafer processing. The effect of these processing variations can result in the detuning of the MMICs lowering circuit yield. As development cycles for wireless products accelerate, design techniques for planar spiral inductors for robust performance in the presence of these process variations in the fabrication of MMICs become necessary.

In design and optimization of microwave circuits using planar spiral inductors, extensive use is made of equivalent circuit models like the one shown in Fig. 1. The circuit parameters, L_0, $R(f)$, C, and $C_{g1,2}$ are specified for a given number of turns, line width, and center-to-center line spacing.

Electromagnetic (EM) simulation is necessary in modeling planar inductors due to their complex structure and effects such as skin and proximity effects between the conductors and mutual inductance between the turns. Full-wave EM simulation of planar inductors can be expensive in terms of computation time and memory, making calculation of circuit response, and circuit yield prohibitive.

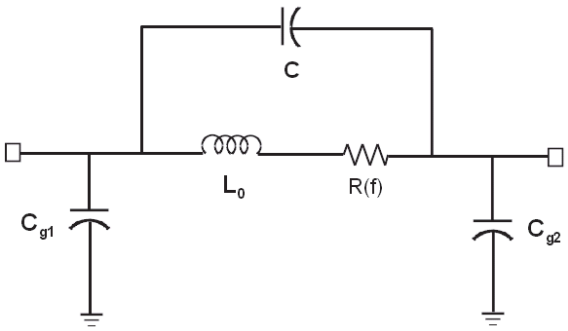

Fig. 1. Equivalent nominal circuit model for spiral inductor used in MMICs.

The Wheeler incremental inductance rule shows that the total change in inductance due to the variation of all conductor surfaces is proportional to the resistance [1-5]. In our earlier paper [6], the inductance change due to variation in the width and thickness of the inductor line was approximated for circular inductors. Here, circular inductors are assumed to have a nearly continuous current distribution while rectangular inductors due to current crowding in the corners have a mostly discontinuous distribution.

The incremental inductance rule allows for the determination of the high frequency resistance of an electrical conductor from its external inductance. A typical application of the incremental inductance rule is for calculating the resistance and loss of a conductor based on information about its inductance [2]. In this paper, the incremental inductance rule is used in reverse of the conventional approach to calculate the change in inductance given its known nominal resistance and assuming variation in one of the physical parameters, namely its conductor width, w, or thickness, t.

The incremental inductance rule can be used to quickly estimate the variation in inductance due to variation in the conductor line width or thickness given only its nominal resistance value. The estimate for variation in inductance together with the known nominal inductance can be used to calculate the total inductance due to over- or under-etching of the metal lines.

Sonnet em [7] is a method of moments based analysis tool and is used to calculate the scattering parameters for several inductors. The resulting equivalent circuit model parameters are extracted and the series resistance values are used to estimate the change in inductance due to variation in line width. Using this method, accurate calculation of the resistance becomes necessary. Multiple sheets and a fine discretization grid must be used to get high accuracy. A convergence test is used to verify the extracted model parameter values. An alternative to the method of moments is a stochastic solution for extraction of external inductances [8]. The advantage of the stochastic methodology is that it requires no descretization or meshing.

This paper is organized as follows: Section II describes the Wheeler incremental inductance rule and a simple model is derived for the normalized change in inductance for microstrip lines; Section III the model is verified; Section IV gives results for the change in inductance for different inductors; and finally, the paper is concluded.

II. THEORETICAL DEVELOPMENT

The Wheeler incremental inductance rule states that the high frequency loss resistance of a conductor can be determined from the normal derivative of its inductance. This rule applies to all conductor shapes for which the current flow is determined by the skin effect. This rule assumes that the radius of curvature of each conductor is large compared with the conductor skin depth (preferably several skin depths) [2]. For a rectangular microstrip line, the incremental inductance rule becomes (see Fig. 2a and 2b):

$$R(f) = \frac{R_S}{\mu_0} \sum_{j=1}^{6} \frac{\partial L}{\partial n_j} = \frac{R_S}{\mu_0} \left(-2\frac{\partial L}{\partial w} - 2\frac{\partial L}{\partial t} + 2\frac{\partial L}{\partial h} \right), \quad (1)$$

where $R_s = \sqrt{\pi f \mu / \sigma}$ is the surface resistance of the conductor and n_j is the normal pointing into the j^{th} conductor surface.

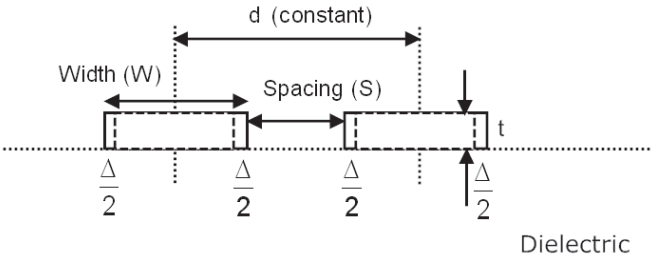

Fig. 2a. Cross-section of microstrip lines showing under-etch/over-etch of lines.

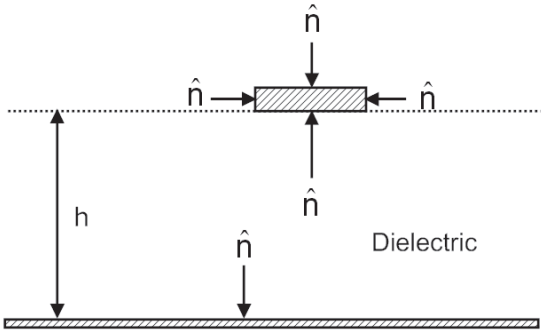

Fig. 2b. Cross-section of microstrip line showing normal vector to each conducting surface.

A widely used expression for microstrip line inductance is from Wheeler [2]:

$$L = \frac{\mu_0}{2\pi} l \left[ln\left(\frac{8h}{w'}\right) + \frac{1}{32}\left(\frac{w'}{h}\right)^2 + \ldots \right], \qquad (2)$$

for $w'/h \le 1$ and w' is the equivalent conductor width and l is the length of the microstrip line.

Microstrip transmission lines having width w and nonzero thickness ($t > 0$) can be modeled as a conductor having zero thickness ($t = 0$) and an equivalent conductor width given by $w' = w + \Delta w$. Different widths (Δw) must be used depending on the transmission line parameter being considered e.g. L, C, Z_0, or ε_{eff} [3]. The inductance (L) is not affected by the substrate dielectric constant. For microstrip, an accurate model for the increment in the conductor width is given by [9] and the equivalent line width becomes:

$$w' = w + \Delta w = w + \frac{t}{\pi}\left(1 + ln\left(\frac{4\pi w}{t}\right)\right). \qquad (3)$$

Using the above definition for L, the ratio of the incremental inductance from one side of the microstrip to the total incremental inductance is approximated for $h >> w$ as:

$$C(h,w,t) = \frac{-\partial L/\partial w}{\sum_j \frac{\partial L}{\partial n_j}} \approx \frac{1 + t/(\pi w)}{2 + 2t/(\pi w) + \frac{2}{\pi} ln\left(\frac{4\pi w}{t}\right) + \frac{2w'}{h}}. \qquad (4a)$$

The ratio of the change in incremental inductance from the top of the microstrip line to the total incremental inductance can be approximated as:

$$D(h,w,t) = \frac{-\partial L/\partial t}{\sum_j \frac{\partial L}{\partial n_j}} \approx \frac{\frac{1}{\pi} ln\left(\frac{4\pi w}{t}\right)}{2 + 2t/(\pi w) + \frac{2}{\pi} ln\left(\frac{4\pi w}{t}\right) + \frac{2w'}{h}}. \qquad (4b)$$

Substituting the partial change in inductance in equations (4a) and (4b) into the definition for loss resistance in equation (1), the change in inductance verse change in line width for the microstrip is:

$$\frac{dL}{dw} = C(h,w,t)\frac{\mu_0}{R_s} R(f), \qquad (5a)$$

and the change in inductance verse change in line thickness becomes:

$$\frac{dL}{dt} = D(h,w,t)\frac{\mu_0}{R_s} R(f). \qquad (5b)$$

III. MODEL VERIFICATION

To corroborate the above, $C(h,w,t)$ and $D(h,w,t)$ are compared with the simulated change in inductance for a microstrip line using Sonnet. Sonnet is a full wave electromagnetic simulator for planar microwave structures and is a tool of choice due to high accuracy requirements. Microstrip lines with length l = 150 μm and width varying from 3 to 20 μm on Gallium Arsenide (GaAs, ε_r = 12.9) with a substrate thickness of h = 100 μm and metal thickness of t = 2 μm are simulated. The microstrip conductor is Gold and for simplicity the loss tangent for the GaAs substrate is assumed to be zero. The thick metal approximation in Sonnet is used to accurately model the 3D characteristics of thick conductors such as loss and electromagnetic effects of physically thick metal such as coupling between closely spaced conductors.

For accurate EM analysis, a calibration procedure is first carried out to determine the number of sheets and grid spacing necessary. The microstrip line with w = 5 μm and 10 μm is analyzed for increasing the number of sheets and different grid spacing. The number of sheets is increased until the extracted resistance and inductance values of the microstrip line converge [10]. The pointer robust optimization in Microwave Office is used to extract the series inductance, resistance, and shunt capacitance to ground [11]. This optimization uses multiple search methods to fit the simulated data from Sonnet to the microstrip equivalent circuit model. At 16 GHz, the t = 2 μm thick Gold microstrip line is about 3 skin depths thick. The extracted

inductance value is nearly independent of the number of sheets. For w = 5 μm, the extracted resistance value converges for 15 sheets using a 0.5 μm grid. For w = 10 μm, the extracted resistance value converges to within 5% of the final value for 20 sheets using a 1 μm grid.

To conserve simulation time, a 0.5 μm layout grid is used for 5 μm wide lines, and a 1 μm grid is used for 10 μm wide lines. Also, 20 sheets or about five sheets per skin depth at 16 GHz are used to model the thick conductor. Using the extracted values for $R(f)$ and L for the microstrip line at f = 16 GHz, $\sum_j \partial L / \partial n_j$ is calculated using (1), and $\partial L/\partial w$ and $\partial L/\partial t$ are approximated by calculating $\Delta L/\Delta w$ and $\Delta L/\Delta t$ for w = 3 - 20 μm. Figure 3 shows the ratio of the change in inductance due to recession of the line width and line thickness versus the total change in inductance caused by recession of all conductor surfaces using the models $C(h,w,t)$ and $D(h,w,t)$, and the extracted EM values for $\frac{-\partial L/\partial w}{\sum_j \partial L/\partial n_j}$ and $\frac{-\partial L/\partial t}{\sum_j \partial L/\partial n_j}$.

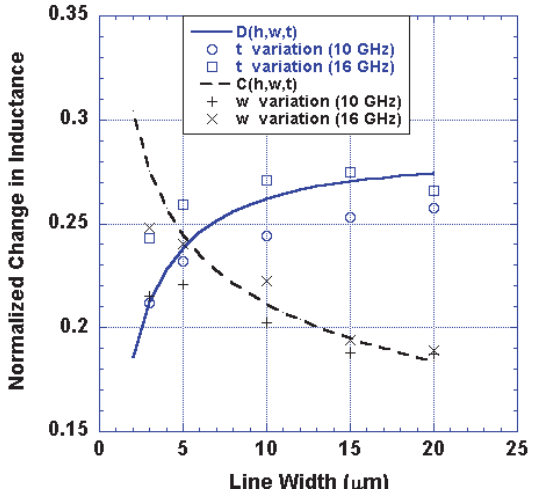

Fig. 3. Ratio of change in inductance due to change in line width and thickness vs. change in total inductance for t = 2 μm line.

These models agree quite well with the extracted values for f = 16 GHz and $w \geq 5$ μm. The modeled and extracted values for normalized changes in inductance for f = 10 GHz begin to diverge for w < 5 μm. At 10 GHz, the skin depth for Gold is 0.8 μm.

Circular inductors on GaAs substrates plated up to 9 μm metal thickness have been reported [12]. In most cases, circular spiral inductors have higher Q and lower resistance than rectangular inductors [12]. The higher resistance in the rectangular inductors is mainly due to the resistance in the corners that are not present in circular inductors. At high frequencies, currents crowd inside of the inner bends and result in higher resistance. The incremental inductance rule implies that the lower resistance in circular inductors results in circular inductors having less variation in inductance than rectangular inductors due to variations in cross section. Circular inductors have no corners and result in more uniform current distribution along the length of the inductor. Figures 4a and 4b show the magnitude of the computed current density using Sonnet for rectangular and circular inductors at 16 GHz. EM simulations were carried out with Sonnet, Release 12 [7] on a workstation using a dual Intel Xeon 2.66 GHz CPU (8 cores) and 16 GByte of RAM. In the next section, simulation results show that circular inductors have lower resistance than the corresponding rectangular inductors with nearly the same dimensions and inductance values.

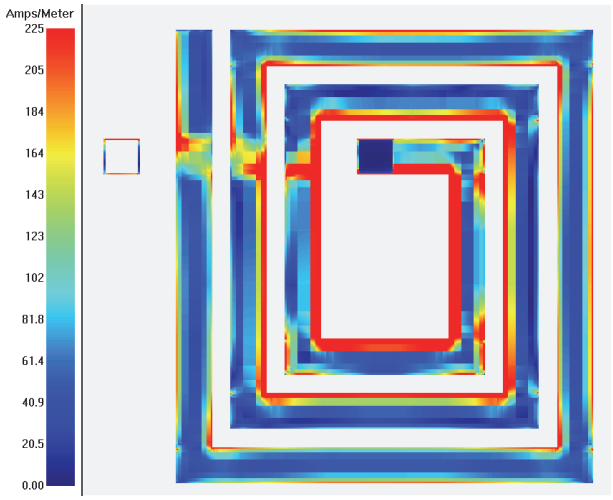

Fig. 4a. Current distribution for three-turn rectangular inductor with w = 10 μm and s = 5 μm at 16 GHz.

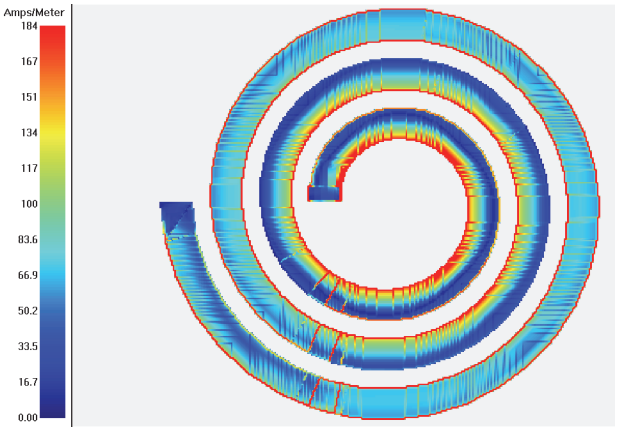

Fig. 4b. Current distribution for three-turn circular inductor with w = 10 μm and s = 5 μm at 16 GHz.

IV. RESULTS

A. Change in inductance

The total inductance including variation due to change in line width Δw and thickness Δt are modeled to first order as:

$$L \cong L_0 + \frac{dL}{dw}\Delta w \text{ , and} \qquad (6a)$$

$$L \cong L_0 + \frac{dL}{dt}\Delta t \text{ ,} \qquad (6b)$$

where L_0 is the nominal inductance (no over- or under-etch) and dL/dw and dL/dt are computed using (6a) and (6b).

Microstrip inductors with line width, w = 5 and 10 μm and spacing, s = 5 μm on Gallium Arsenide (GaAs, ε_r = 12.9) with a substrate thickness of h = 100 μm and metal thickness of t = 2 μm are simulated. The microstrip conductor is Gold and for simplicity the loss tangent for the GaAs substrate is assumed to be zero. The thick metal approximation in Sonnet is used to accurately model the 3D characteristics of thick conductors such as loss and electromagnetic effects of physically thick metal such as coupling between closely spaced conductors. For circular inductors, a conformal type mesh is used. For rectangular inductors, the staircase type fill is used.

Circular spiral inductors with N = 2 to 4 turns and nominal line widths of 5 μm and 10 μm are considered. The nominal spacing is 5 μm. The center-to-center line spacing is held constant and the line thickness is fixed at t = 2 μm. For the first case, all line widths except for the airbridge are under etched and over etched 1 and 2 μm. For the second case, the line width and spacing are fixed at the nominal values and the line thickness is under etched and over etched 0.5 um and 1 μm from the nominal line thickness t = 2 μm.

Using the procedure described earlier, the simulated data for the circular inductors from Sonnet are fit to the equivalent circuit model in Fig. 1 at f = 16 GHz. Figures 5a and 5b show the modeled inductance using equation (6a) and extracted inductance vs. amount of over- and under-etching of line width, Δw. Figures 6a and 6b show the modeled inductance using equation (6b) and extracted inductance vs. amount of over- and under-etching of line thickness, Δt. The extracted inductances vary linearly with Δw and Δt [13-14].

Tables 1a and 1b show the variation in inductance between the models in equations (6a) and (6b) and the extracted values from EM simulation. For N = 3 turns and w = 5 μm, the variation in extracted inductance due to variation in line width is 13 %. For N = 3 turns and w = 10 μm, the variation in extracted inductance is 10.8 %. These values compare well with the modeled inductance variations of 14 % and 10 %. For N = 3 turns and w = 5 μm, the variation in extracted inductance due to variation in line thickness is 6.6 %. For N = 3 turns and w = 10 μm, the variation in extracted inductance is 6.2 %. These values compare well with the modeled inductance variations of 6.8 % and 6.2 %.

B. Circular vs. rectangular inductors

The equivalent circuit model parameters are now computed for circular and rectangular planar inductors. The resistance for circular and rectangular inductors having nearly the same inductance will be extracted and the relationship between the resistance and change in inductance will be shown [14]. The microstrip inductors with N = 3 and 4 turns are analyzed for increasing number of sheets and finer grid spacing. For accurate EM analysis, the procedure used in the previous section is modified to minimize computation time by extrapolating the resistance value.

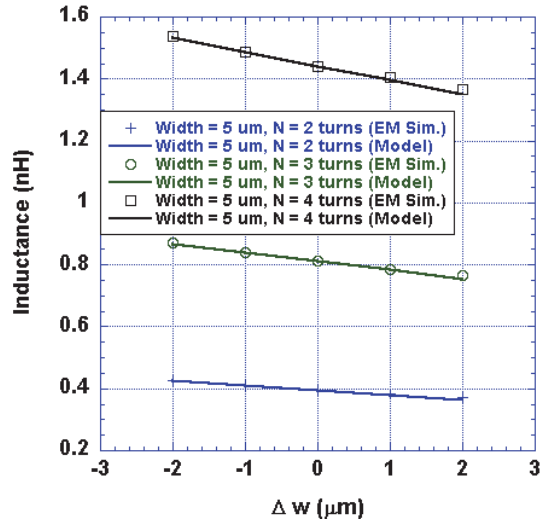

Fig. 5a. Inductance vs. Δw for w = 5 μm.

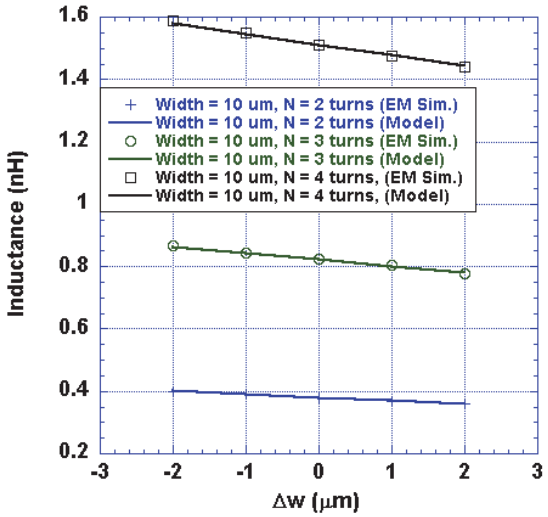

Fig. 5b. Inductance vs. Δw for w = 10 μm.

Using the earlier work by Richardson [15-17], a more accurate solution is achieved without a very fine discretization. A convergence ratio gives a measure of the goodness of the extrapolation. For true monotonic convergence, the convergence ratio is unity. Tables 2a-b and 3a-b show the extracted resistance, inductance, and parallel capacitance values of two circular inductors having w = 10 μm and N = 3 and 4 turns. The extrapolated values using the 3-point Richardson's extrapolation technique are included. As shown in these Tables, the inductance and parallel capacitance values converge very quickly. The resistance values, however, converge more slowly. The extracted resistance and inductance values converge to within 1 % of their final value for 15 sheets using a 0.5 μm grid. To conserve simulation time, a 0.5-μm minimum layout grid size is used for 10 μm wide lines. Also, 15 sheets or about five sheets per skin depth at 16 GHz are used to model the thick conductor.

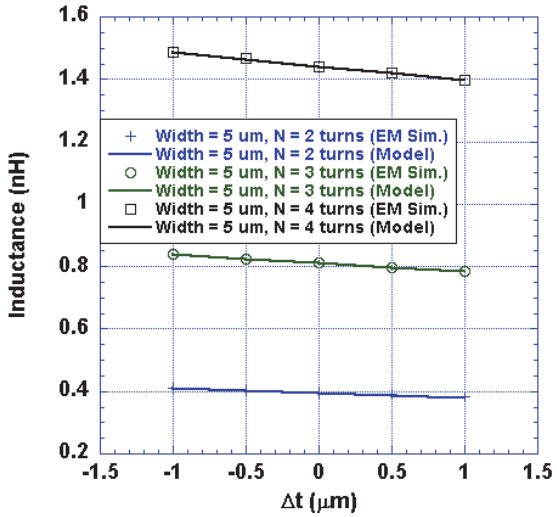

Fig. 6a. Inductance vs. Δt for w = 5 μm.

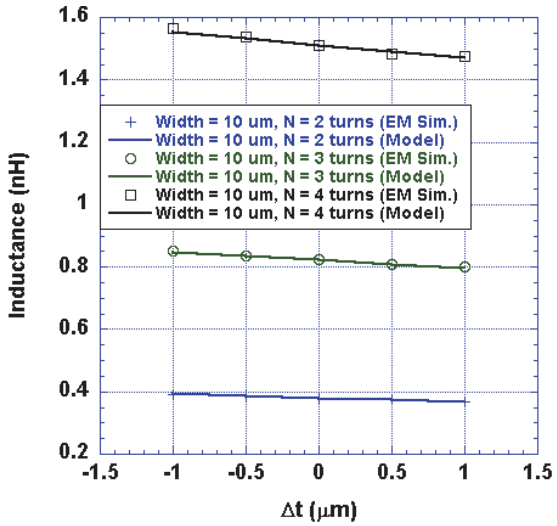

Fig. 6b. Inductance vs. Δt for w = 10 μm.

Using the procedure described above, the simulated data for four circular and rectangular inductors from Sonnet are used to extract the equivalent inductance and resistance values versus variation in line width, Δw at f = 16 GHz. The inductors have N = 3 and 4 turns, with w = 5 and 10 μm and s = 5 μm. The rectangular and circular

inductors also have nearly the same nominal inductance value, e.g. 0.81 nH for $N = 3$ turns, $w =$ 5 μm and 1.45 nH for $N = 4$ turns, $w = 5$ μm. Figures 7a and 7b show the extracted resistance and inductance values vs. over- and under-etch of the line width, Δw for $N = 3$ turns, $w = 5$ and 10 μm. Figures 7c and 7d show the extracted resistance and inductance values vs. amount of over- and under-etch of the line width, Δw for $N =$ 4 turns, $w = 5$ and 10 μm. In each case, the center line to line spacing, $w + s$, is held constant and the extracted inductance values vary linearly with Δw. The nominal resistance vs. the total change in inductance for the circular and rectangular inductors is shown in Table 4. For $N = 3$ turns and $w = 10$ μm, the variation in extracted inductance due to variation in line width is +/-10.7 % for the rectangular inductor and +/-5.5 % for the circular inductor. For $N = 4$ turns and $w =$ 10 μm, the variation in extracted inductance due to variation in line width is +/-9.5 % for the rectangular inductor and only +/-5 % for the circular inductor.

Table 1a: Variation in inductance for $\Delta w =$ +/-2μm

Inductor	EM Simulation	Model using (6a)
N = 2, w = 5 μm	13.5 %	15.3 %
N = 2, w =10 μm	10.2 %	10.6 %
N = 3, w = 5 μm	13 %	14 %
N = 3, w =10 μm	10.8 %	10 %
N = 4, w = 5 μm	11.8 %	12.6 %
N = 4, w = 10 μm	9.7 %	9 %

Table 1b: Variation in inductance for $\Delta t =$ +/-1μm

Inductor	EM Simulation	Model using (6b)
N = 2, w = 5 μm	7.2 %	7.5 %
N = 2, w =10 μm	6.4 %	6.6 %
N = 3, w = 5 μm	6.6 %	6.8 %
N = 3, w =10 μm	6.2 %	6.2 %
N = 4, w = 5 μm	6.3 %	6.1 %
N = 4, w = 10 μm	6.1 %	5.6 %

Table 2a: Convergence ratio (CR) for circular inductor resistance (w = 10 μm, N = 4 turns)

Grid / # sheets	1 μm (10)	0.714 μm (14)	0.5 μm (20)	Extrap-olated Value	CR
10	5.02 Ω	5.37 Ω	5.64 Ω	5.96 Ω	0.98
15	5.03 Ω	5.45 Ω	5.75 Ω	6.01 Ω	0.99
20	5.03 Ω	5.5 Ω	5.78 Ω	6.08 Ω	0.99

Table 2b: Extracted inductance and parallel capacitance values for circular inductor (w = 10 μm, N = 4 turns)

Grid / # sheets	1 μm (10)	0.714 μm (14)	0.5 μm (20)
10	1.512 nH 0.014 pF	1.511 nH 0.0141 pF	1.515 nH 0.0141 pF
15	1.512 nH 0.0141 pF	1.511 nH 0.0141 pF	1.515 nH 0.0142 pF
20	1.512 nH 0.0141 pF	1.513 nH 0.0141 pF	1.516 nH 0.0142 pF

Table 3a: Convergence ratio (CR) for circular inductor resistance (w = 10 μm, N = 3 turns)

Grid / # sheets	1 μm (10)	0.714 μm (14)	0.5 μm (20)	Extrap-olated Value	CR
10	2.96 Ω	3.17 Ω	3.33 Ω	3.51 Ω	0.99
15	3.0 Ω	3.23 Ω	3.41 Ω	3.61 Ω	0.99
20	3.03 Ω	3.24 Ω	3.43 Ω	3.65 Ω	0.98

Table 3b: Extracted inductance and parallel capacitance values for circular inductor (w = 10 μm, N = 3 turns)

Grid / # sheets	1 μm (10)	0.714 μm (14)	0.5 μm (20)
10	0.8237 nH 0.0113 pF	0.8223 nH 0.0113 pF	0.8249 nH 0.0113 pF
15	0.8244 nH 0.0116 pF	0.8227 nH 0.0113 pF	0.8246 nH 0.0114 pF
20	0.8246 nH 0.0114 pF	0.8233 nH 0.0113 pF	0.8253 nH 0.0113 pF

Table 4: Resistance vs. change in inductance

	R Circular	R Rectang-ular	Δ L Circular	Δ L Rectang-ular
$N = 3$, w=5μm	3.5 Ω	4.8 Ω	+/-6.4%	+/- 13 %
$N = 4$, w=5μm	5.8 Ω	7.8 Ω	+/-5.3%	+/- 7 %
$N = 3$, w=10μm	3.6 Ω	4.4 Ω	+/-5.5%	+/-10.7%
$N = 4$, w=10μm	6.1 Ω	7.8 Ω	+/-5%	+/- 9.5 %

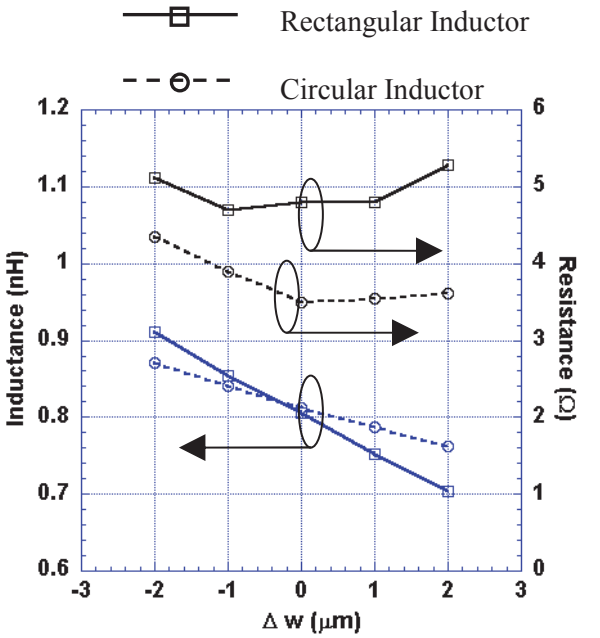

(a) N = 3 turns, w = 5 μm

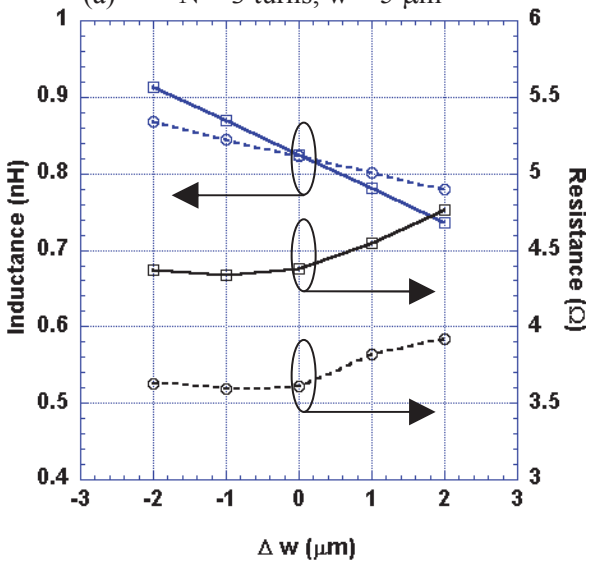

(b) N = 3 turns, w = 10 μm

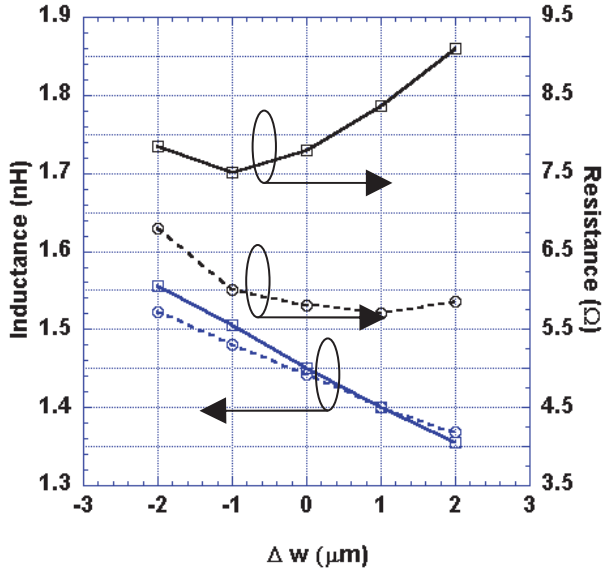

(c) N = 4 turns, w = 5 μm

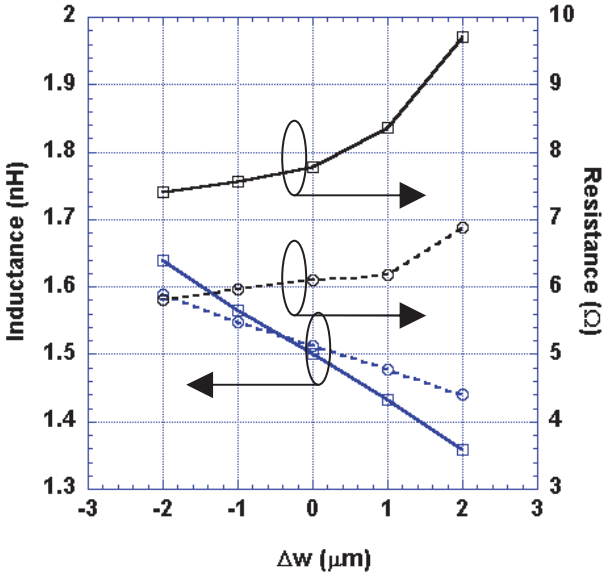

(d) N = 4 turns, w = 10 μm

Fig. 7. Variation in Inductance and Resistance vs. over- and under-etch.

V. DISCUSSION

In the proceeding section, the optimum line width for minimum resistance can be seen as a tradeoff between the resistance of the line and the resistance due to proximity effect between adjacent lines. The close proximity of the lines and the resulting magnetic fields due to the currents flowing in them redistributes the currents causing higher resistance. Consider parallel round

wires having currents flowing in the same direction. This is similar to the case for planar inductors. Each wire has radius *a,* and the center-to-center spacing is *2b*.

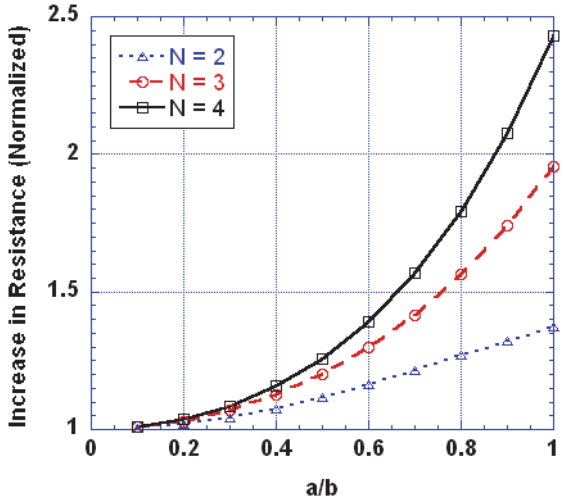

Fig. 8. Proximity effect in parallel conductors.

For small a/b, the increase in proximity resistance is negligible. As the diameter of the wires increases and approaches the spacing, the proximity resistance increases [18]. For more than two wires (N > 2) the increase in resistance becomes even greater (Fig. 8).

VI. CONCLUSION

The variation in inductance for circular planar spiral inductors due to variation in line width and thickness using the Wheeler incremental inductance rule has been investigated. The extracted inductance and capacitance values for planar microstrip inductors using electromagnetic analysis are shown to converge quickly requiring only a 1 μm grid and a few sheets. The extracted resistance values are shown to converge more slowly. At least a 0.5 μm grid and up to five sheets per skin depth are required to accurately capture the cross sectional current distribution of the conductor. An extrapolation procedure is used to accurately extract the resistance values to minimize computation time. The agreement between the modeled and EM simulated variation in inductance is good. This technique can be implemented quickly using a circuit simulator without the need for expensive EM analysis. Results show that circular inductors are more tolerant than rectangular inductors to variations in line width as anticipated by the Wheeler incremental inductance rule. Circular inductors show about one half of the variation in the inductance value due to over- or under-etching than corresponding rectangular inductors having the same inductance value. The results show that an optimum line width can be found for minimum resistance in planar spiral inductors.

ACKNOWLEDGEMENTS

The author wishes to thank Sonnet Software and Applied Wave Research for their generous support.

REFERENCES

[1] H. A. Wheeler, "Formulas for the Skin Effect," *Proc. IRE*, vol. 30, no. 9, pp. 412-424, Sept. 1942.

[2] R. A Pucel, D. J. Masse, and C. P. Hartwig, "Losses in Microstrip," *IEEE Trans. Microw. Theory Tech.*, vol. 16, no. 6, pp.342-350, June 1968.

[3] R. K. Hoffmann, *Handbook of Microwave Integrated Circuits*, Boston, Artech House, 1987.

[4] G. Kompa, *Practical Microstrip Design and Applications*, Boston, Artech House, 2005.

[5] L. Dworsky, *Modern Transmission Line Theory and Applications,* New York, Wiley, 1979.

[6] G. A. Ellis, "Application of Wheeler's Incremental Inductance Rule for Simulating the Effect of Etching Variations in Circular Inductors in MMICs," *INAS 2009,* Dec. 2009.

[7] Sonnet Suites, Release 12, "Users Guide", Chapter 18, Syracuse NY, 2009.

[8] K. Chatterjee, "A Stochastic Algorithm for the Extraction of Partial Inductances in IC Interconnect Structures," *Applied Computational Electromagnetic Society (ACES) Journal*, vol. 21, no. 1, pp. 81-89, March 2006.

[9] H. A. Wheeler, "Transmission-Line Properties of Parallel Strips Separated by a Dielectric Sheet," *IEEE Microw. Theory Tech*, vol. 13, no. 3, pp. 172-185, March 1965.

[10]D. L. Sanderson, J. C. Rautio, R. A. Groves, and S. Raman, "Accurate Modeling of Monolithic Inductors using Conformal

Meshing for Reduced Computation," *IEEE Micro. Mag.*, pp. 87-96, Dec. 2003.

[11] Microwave Offices 2008, AWR, MWO/AO User's Guide.

[12] I. J. Bahl, "High Performance Inductors," *IEEE Trans. Microw. Theory Tech.*, vol. 49, no. 4, pp. 654-664, April 2001.

[13] S. Abdelbagi and G. A. Ellis, "Effects of Variations in Line Width on the Equivalent Circuit Model of Microstrip Spiral Inductors Implemented using GaAs Technology," *SCOReD 2008,* pp. 267-1–267-4, Nov. 2008.

[14] G. A. Ellis, "Application of the Wheeler Incremental Inductance Rule for Robust Design and Modeling of MMIC Spiral Inductors," *26th Annual Review of Progress in Applied Compuatational Electromagnetics,* Tampere, Finland, April 26-29, 2010.

[15] R. C. Culver, "The Use of Extrapolation Techniques with Electrical Network Analogue Solutions," *Brit J. Appl. Phys.,* vol. 3, pp. 376-378, 1952.

[16] H. E. Green, "The Numerical Solution of Some Important Transmission Line Problems," *IEEE Trans. Microw. Theory Tech*, vol. MTT-13, no. 5, pp. 676-692, 1965.

[17] R. Garg, *Analytical and Computational Methods in Electromagnetics,* Boston, Artech House, 2008.

[18] S. Butterworth, "On the Alternating Current Resistance of Solenoidal Coils", *Proc. Roy. Soc.* vol. 107A, p. 693, 1925.

Grant A. Ellis received his Ph.D. degree in Electrical Engineering from the University of Washington, Seattle, in 1995. He is currently Professor of Electrical and Electronic Engineering at the Universiti Teknologi Petronas in Tronoh, Malaysia. His research interests are Monolithic Microwave Integrated Circuit (MMIC) and RFIC design, Microwave computer aided design techniques, and radiowave propagation analysis. Dr. Ellis is the founding chairman of the IEEE MTT/ED/AP Penang Chapter. He has been a Senior Member of the IEEE since 2004.

Parametric Design of Parabolic Reflector Antenna with Switchable Cosecant-Squared Pattern

Ahmet S. Turk[1] and Okan Yurduseven[1,2]

[1] Department of Electronics and Communication Engineering
Yıldız Technical University, Besiktas, Istanbul, 34349, Turkey
asturk@yildiz.edu.tr

[2] Department of Electrical and Electronics Engineering
Marmara University, Goztepe, Istanbul, 34722, Turkey
oyurduseven@marmara.edu.tr

Abstract **-** This paper deals with the parametric analysis of multi-beam parabolic reflector antennas employed for air and coastal surveillance radars. Novel designs are introduced to obtain electronically switchable cosecant-squared and pencil beam radiation patterns, without making any changes on the reflector geometry. The analytical regularization method (ARM) is used as a fast and accurate way to solve the problem of E-polarized wave diffraction by parabolic shaped perfectly electrical conductive (PEC) cylindrical reflector with finite thickness. The numerical procedure is initially verified by the analytical and numerical methods, and the calculated radiation characteristics are presented for the proposed antenna configurations.

Index Terms **-** Analytical regularization method, cosecant-squared radiation pattern, multi-source horn, parabolic reflector antenna.

I. INTRODUCTION

Parabolic reflectors are one of the most popular antenna types commonly used in microwave and millimeter wave radars, power transmission, satellite communication, and navigation systems [1-4]. They have generally large physical dimensions with respect to the wavelength. Thus, high frequency electromagnetic wave scattering techniques such as, geometrical optics (GO), physical optics (PO), aperture integration (AI), and geometric theory of diffraction (GTD) are mostly used for determining the far field antenna characteristics [5-6]. Besides, direct numerical techniques such as, method of moments (MoM), finite element method (FEM), and finite difference methods are considered more versatile and usable in practice for feeder and reflector designs [7-8]. Nevertheless, large size antenna analyses usually require long computation times [9-10]. Furthermore, MoM and FEM can cause unstable numerical processes in most cases due to reducing the boundary value problem (BVP) to the algebraic equation set of the first kind that usually has a singular kernel with a big condition number Thus, minimizing the computational error by increasing the truncation number of the matrix-vector algebraic equation set cannot be guaranteed [11-13]. Hence, the analytical regularization method (ARM) that transforms the ill-conditioned integral equation of the first kind into a well-conditioned one of the second kind is preferred to solve the matrix equation numerically by truncation method with fast convergence to reach fast and reliable solutions [14]. The ARM solutions of the parabolic reflector structure and the H-plane horn feeder have been demonstrated separately by Turk to characterize the antenna patterns in the next step [11,16-17].

In this study, radiation characteristics of the cylindrical parabolic reflector fed by the H-plane

horn are treated parametrically to obtain pencil beam, cosecant-squared, and inverse cosecant-squared radiation patterns for air and coastal surveillance radars. For this purpose, the BVP is essentially formulated with respect to the z-component of the electric field satisfying Helmholtz's equation with Dirichlet boundary condition, and the ARM procedure is applied to obtain fast, accurate, and reliable results (see [15-17] for verification). New design proposals on mechanical switching of different beam types (pencil, cosec2, inverse cosec2) are investigated only by rotating one flare arm of the feeder horn to provide asymmetric illumination.

The final goal of the paper is achieving both pencil beam and cosecant-squared radiation patterns for one fixed reflector antenna geometry simply by electronic pin-switching of the dual-source H-plane horn feeder. By this way, both cosecant-squared and pencil beam radiation patterns can be switched electronically for the same feeder horn and reflector structure.

II. ARM FORMULATION

The parabolic reflector antenna is primarily considered as a perfectly conducting, smooth, longitudinally homogeneous and infinitely long in *z*-direction cylindrical obstacle, which is illuminated by the horn feeder. The XOY cross section of the structure shown in Fig. 1 is denoted by the closed contour *S*. If we assume the case that scalar wave does not vary along *z*-axis, the diffraction problem of such a scatterer object corresponds to the 2D Dirichlet boundary condition for incidence of the E-polarized wave. Thus, the incident and scattered scalar wave functions ($u^i(p)$ and $u^s(p)$) should satisfy the Helmholtz equation and the Dirichlet boundary condition given in Eq. (1) and Eq. (2), also with the Sommerfeld radiation condition (see [14]).

$$\left(\Delta + k^2\right) u^s(p) = 0, \quad p \in R^2 \setminus S, \tag{1}$$

$$u^{s(+)}(p) = u^{s(-)}(p) = -u^i(p), \quad p \in S, \tag{2}$$

where, S is the smooth contour of the structure domain in 2D space R^2 that belongs to the smoothness class $C^{2,\alpha}$ [14]. $u^{s(+)}(p)$ and $u^{s(-)}(p)$ are limiting values of $u^s(p)$ in the inner and the outer sides of the *S*, respectively. The Eq. (3) is the BVP solution obtained by the Green's formula and the boundary condition in Eq. (2).

$$-\frac{i}{4}\int_S \left[H_0^{(1)}(k\,|\,q-p\,|)Z(p)\right] dl_p = -u^i(q), \quad q, p \in S, \tag{3}$$

where, $Z(p) = \dfrac{\partial u^{s(-)}(p)}{\partial n} - \dfrac{\partial u^{s(+)}(p)}{\partial n}$ for $p \in S$, and n is the unit outward with respect to S normal of the point p. The unknown function $Z(p)$ is constructed by solving Eq. (3), and using parameterization of the S contour specified by the function $\eta(\theta) = (x(\theta), y(\theta))$ that smoothly parameterizes the contour S by the points of $\theta \in [-\pi, \pi]$. Using the $\eta(\theta)$ parameterization, the integral equation representation of the first kind in Eq. (3) can be equivalently rearranged as follows:

$$\frac{1}{2\pi}\int_{-\pi}^{\pi} \left\{ \ln\left|2\sin\frac{\theta-\tau}{2}\right| + K(\theta,\tau)\right\} Z_D(\tau)\, d\tau = g(\theta), \tag{4}$$

by means of the following $\eta(\theta)$ transformations:

$$Z_D(\theta) = \left([x'(\theta)]^2 + [y'(\theta)]^2\right)^{1/2} Z(\eta(\theta)), \quad \theta \in [-\pi, \pi] \tag{5}$$

$$|\,q-p\,| = \left\{[x(\theta)-x(\tau)]^2 + [y(\theta)-y(\tau)]^2\right\}^{1/2}, \quad \theta \in [-\pi, \pi] \tag{6}$$

$$g(\theta) = -u^i(\eta(\theta)), \qquad \theta \in [-\pi, \pi]. \tag{7}$$

In Eq. (4), the unknown function is $Z_D(\tau)$, the given function is $g(\theta)$, and $K(\theta,\tau)$ function is the rather smooth section of the Green's function in comparison with the logarithmic part that contains the main singularity of this equation (see [14,15] for details). The Fourier series expansions of the functions are defined in set of Eqs. (8)-(11).

$$K(\theta,\tau) = \sum_{s=-\infty}^{\infty}\sum_{m=-\infty}^{\infty} k_{sm} e^{i(s\theta+m\tau)}, \quad \theta \in [-\pi, \pi], \tag{8}$$

$$\ln\left|2\sin\frac{\theta-\tau}{2}\right| = -\frac{1}{2}\sum_{\substack{n=-\infty \\ n\neq 0}}^{\infty} |\,n\,|^{-1} e^{in(\theta-\tau)}, \quad \theta \in [-\pi, \pi], \tag{9}$$

$$Z_D(\tau) = \sum_{n=-\infty}^{\infty} z_n e^{in\tau}, \quad \tau \in [-\pi, \pi], \tag{10}$$

$$g(\theta) = \sum_{n=-\infty}^{\infty} g_n e^{in\theta}, \quad \theta \in [-\pi, \pi]. \tag{11}$$

Hence, one can obtain the infinite system of the linear algebraic equations of the second kind given in Eq. (12) that guarantees the convergence and stability of the numerical process [14].

$$\hat{z}_s + \sum_{m=-\infty}^{\infty} \hat{k}_{s,m}\hat{z}_m = \hat{g}_s, \quad s = \pm 1, \pm 2, .. \tag{12}$$

where,

$$\left.\begin{aligned} \hat{k}_{s,m} &= -2\tau_s\tau_m\left[k_{s,-m} + \frac{1}{2}\delta_{s,0}\delta_{m,0}\right] \\ \hat{z}_n &= \tau_n^{-1}z_n, \hat{g} = -2\tau_s g_s, \tau_n = \max(1, |n|^{1/2}) \end{aligned}\right\}, \; n = 0, \pm 1, \pm 2, .. \tag{13}$$

Finally, the scattered field $u^s(q)$ for $q \in R^2$ is calculated by the integral equation representation of the Eq. (3) with any required accuracy by using the truncation method (see [15,17] for details).

III. PARAMETRIC DESIGN OF PARABOLIC REFLECTOR ANTENNA

The ARM procedure described at Section II is derived for the investigated parabolic antenna types. The geometrical cross-section of the reflector is a modified parabolic arc, which is modeled by ARM as a closed contour L that goes from point A to point M and back to A corresponding to $\theta \in [-\pi, \pi]$, as illustrated in Fig. 1. The relation between l and θ is formulated in Eq. (14).

$$\left.\begin{aligned} l &= (\theta + \pi)L/2\pi \\ l &\in [0, L] \rightarrow (\theta, \tau) \in [-\pi, \pi] \end{aligned}\right\}. \tag{14}$$

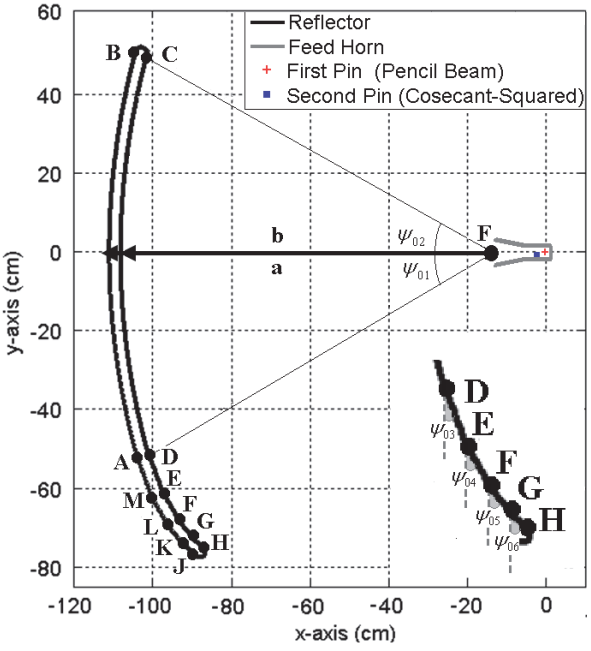

Fig. 1. XOY-plane geometry of parabolic reflector with multi-source H-plane horn feeder.

The reflector structure consists of totally 12 contour parts, which are defined in Table 1 and 2.

Table 1: Parametric definitions of reflector contour

No	Region	Definition
1	AB	$-\pi \le \theta < -\pi + 2L_{AB}\,\pi/L$
2	BC	$-\pi + 2L_{AB}\,\pi/L \le \theta < -\pi + 2L_{BC}\,\pi/L$
3	CD	$-\pi + 2L_{BC}\,\pi/L \le \theta < -\pi + 2L_{CD}\,\pi/L$
4	DE	$-\pi + 2L_{CD}\,\pi/L \le \theta < -\pi + 2L_{DE}\,\pi/L$
5	EF	$-\pi + 2L_{DE}\,\pi/L \le \theta < -\pi + 2L_{EF}\,\pi/L$
6	FG	$-\pi + 2L_{EF}\,\pi/L \le \theta < -\pi + 2L_{FG}\,\pi/L$
7	GH	$-\pi + 2L_{FG}\,\pi/L \le \theta < -\pi + 2L_{GH}\,\pi/L$
8	HJ	$-\pi + 2L_{GH}\,\pi/L \le \theta < -\pi + 2L_{HJ}\,\pi/L$
9	JK	$-\pi + 2L_{HJ}\,\pi/L \le \theta < -\pi + 2L_{JK}\,\pi/L$
10	KL	$-\pi + 2L_{JK}\,\pi/L \le \theta < -\pi + 2L_{KL}\,\pi/L$
11	LM	$-\pi + 2L_{KL}\,\pi/L \le \theta < -\pi + 2L_{LM}\,\pi/L$
12	MA	$-\pi + 2L_{LM}\,\pi/L \le \theta < \pi$

Table 2: Segment lengths of the contour regions

No	Region	Segment Length
1	AB	$L_{AB} = b\tan((\psi_{02} - \psi_{01})/2)$
2	BC	$L_{BC} = L_{AB} + \pi c_2$
3	CD	$L_{CD} = L_{BC} + a\tan((\psi_{02} - \psi_{01})/2)$
4	DE	$L_{DE} = L_{CD} + c_3$
5	EF	$L_{EF} = L_{DE} + 0.75c_3$
6	FG	$L_{FG} = L_{EF} + 0.5c_3$
7	GH	$L_{GH} = L_{FG} + 0.25c_3$
8	HJ	$L_{HJ} = L_{GH} + \pi c_1$
9	JK	$L_{JK} = L_{HJ} + 0.25c_3$
10	KL	$L_{KL} = L_{JK} + 0.5c_3$
11	LM	$L_{LM} = L_{KL} + 0.75c_3$
12	MA	$L = L_{LM} + c_3$
* $c_1 = (b-a)/(1+\cos(\psi_{01}))$, $c_2 = (b-a)/(1+\cos(\psi_{02}))$, $c_3 = 4\lambda$		

The parameterization of the contour line is implemented separately from point A to M, and back to A by means of the variable $l \in [0, L]$ as follows:

$$x = \frac{-2b\cos\varphi_{01}}{1+\cos\varphi_{01}} - X_s, \quad y = \frac{2b\sin\varphi_{01}}{1+\cos\varphi_{01}}, \; l \in [AB), \tag{15}$$

$$\left.\begin{aligned} x &= c_2\cos\left(\frac{-l + L_{AB}}{c_2} + \pi - \psi_{02}\right) - \frac{(a+b)\cos\psi_{02}}{1+\cos\psi_{02}} - Xs \\ y &= c_2\sin\left(\frac{-l + L_{AB}}{c_2} + \pi - \psi_{02}\right) + \frac{(a+b)\sin\psi_{02}}{1+\cos\psi_{02}} \end{aligned}\right\}, \; l \in [BC), \tag{16}$$

$$x = \frac{-2a\cos\varphi_{02}}{1+\cos\varphi_{02}} - X_s, \quad y = \frac{2a\sin\varphi_{02}}{1+\cos\varphi_{02}},\ l \in [CD), \tag{17}$$

$$\left.\begin{aligned} x &= \frac{-2a\cos\psi_{01}}{1+\cos\psi_{01}} + (l - L_{CD})\cos\psi_{03} - X_s \\ y &= \frac{2a\sin\psi_{01}}{1+\cos\psi_{01}} - (l - L_{CD})\sin\psi_{03} \end{aligned}\right\},\ l \in [DE), \tag{18}$$

$$\left.\begin{aligned} x &= \frac{-2a\cos\psi_{01}}{1+\cos\psi_{01}} + c_3\cos\psi_{03} + (l - L_{DE})\cos\psi_{04} - X_s \\ y &= \frac{2a\sin\psi_{01}}{1+\cos\psi_{01}} - c_3\sin\psi_{03} - (l - L_{DE})\sin\psi_{04} \end{aligned}\right\},\ l \in [EF), \tag{19}$$

$$\left.\begin{aligned} x &= \frac{-2a\cos\psi_{01}}{1+\cos\psi_{01}} + (l - L_{EF})\cos\psi_{05} - X_s \\ &\quad + c_3(\cos\psi_{03} + 0.75\cos\psi_{04}) \\ y &= \frac{2a\sin\psi_{01}}{1+\cos\psi_{01}} - (l - L_{EF})\sin\psi_{05} \\ &\quad - c_3(\sin\psi_{03} + 0.75\sin\psi_{04}) \end{aligned}\right\},\ l \in [FG), \tag{20}$$

$$\left.\begin{aligned} x &= \frac{-2a\cos\psi_{01}}{1+\cos\psi_{01}} + (l - L_{FG})\cos\psi_{06} - X_s \\ &\quad + c_3(\cos\psi_{03} + 0.75\cos\psi_{04} + 0.5\cos\psi_{05}) \\ y &= \frac{2a\sin\psi_{01}}{1+\cos\psi_{01}} - (l - L_{FG})\sin\psi_{06} \\ &\quad - c_3(\sin\psi_{03} + 0.75\sin\psi_{04} + 0.5\sin\psi_{05}) \end{aligned}\right\},\ l \in [GH), \tag{21}$$

$$\left.\begin{aligned} x &= c_1\cos\left(\frac{-l + L_{GH}}{c_1} - \psi_{01}\right) - \frac{(a+b)\cos\psi_{01}}{1+\cos\psi_{01}} - Xs \\ &\quad + c_3(\cos\psi_{03} + 0.75\cos\psi_{04} + 0.5\cos\psi_{05} + 0.25\cos\psi_{06}) \\ y &= c_1\sin\left(\frac{-l + L_{GH}}{c_1} - \psi_{01}\right) + \frac{(a+b)\sin\psi_{01}}{1+\cos\psi_{01}} \\ &\quad - c_3(\sin\psi_{03} + 0.75\sin\psi_{04} + 0.5\sin\psi_{05} + 0.25\sin\psi_{06}) \end{aligned}\right\},\ l \in [HJ), \tag{22}$$

$$\left.\begin{aligned} x &= c_1\cos(\pi + \psi_{01}) - \frac{(a+b)\cos\psi_{01}}{1+\cos\psi_{01}} - (l - L_{HJ})\cos\psi_{06} - Xs \\ &\quad + c_3(\cos\psi_{03} + 0.75\cos\psi_{04} + 0.5\cos\psi_{05} + 0.25\cos\psi_{06}) \\ y &= c_1\sin(-\pi - \psi_{01}) + \frac{(a+b)\sin\psi_{01}}{1+\cos\psi_{01}} + (l - L_{HJ})\sin\psi_{06} \\ &\quad - c_3(\sin\psi_{03} + 0.75\sin\psi_{04} + 0.5\sin\psi_{05} + 0.25\sin\psi_{06}) \end{aligned}\right\},\ l \in [JK), \tag{23}$$

$$\left.\begin{aligned} x &= c_1\cos(\pi + \psi_{01}) - \frac{(a+b)\cos\psi_{01}}{1+\cos\psi_{01}} - (l - L_{JK})\cos\psi_{05} - Xs \\ &\quad + c_3(\cos\psi_{03} + 0.75\cos\psi_{04} + 0.5\cos\psi_{05}) \\ y &= c_1\sin(-\pi - \psi_{01}) + \frac{(a+b)\sin\psi_{01}}{1+\cos\psi_{01}} + (l - L_{JK})\sin\psi_{05} \\ &\quad - c_3(\sin\psi_{03} + 0.75\sin\psi_{04} + 0.5\sin\psi_{05}) \end{aligned}\right\},\ l \in [KL), \tag{24}$$

$$\left.\begin{aligned} x &= c_1\cos(\pi + \psi_{01}) - \frac{(a+b)\cos\psi_{01}}{1+\cos\psi_{01}} - Xs \\ &\quad + c_3(\cos\psi_{03} + 0.75\cos\psi_{04}) - (l - L_{KL})\cos\psi_{04} \\ y &= c_1\sin(-\pi - \psi_{01}) + \frac{(a+b)\sin\psi_{01}}{1+\cos\psi_{01}} \\ &\quad - c_3(\sin\psi_{03} + 0.75\sin\psi_{04}) + (l - L_{KL})\sin\psi_{04} \end{aligned}\right\},\ l \in [LM), \tag{25}$$

$$\left.\begin{aligned} x &= c_1\cos(\pi + \psi_{01}) - \frac{(a+b)\cos\psi_{01}}{1+\cos\psi_{01}} - Xs \\ &\quad + c_3\cos\psi_{03} - (l - L_{LM})\cos\psi_{03} \\ y &= c_1\sin(-\pi - \psi_{01}) + \frac{(a+b)\sin\psi_{01}}{1+\cos\psi_{01}} \\ &\quad - c_3\sin\psi_{03} + (l - L_{LM})\sin\psi_{03} \end{aligned}\right\},\ l \in [MA), \tag{26}$$

where, $X_s = 5.243\lambda$ and,

$$\varphi_{01} = \psi_{01} + [(\psi_{02} - \psi_{01})l / L_{AB}], \tag{27}$$

$$\varphi_{02} = \psi_{02} - [(\psi_{02} - \psi_{01})(l - L_{BC}) / (L_{CD} - L_{BC})]. \tag{28}$$

The horn feeder model illustrated in Fig. 1 is assumed to be located at the focus of the PEC reflector antenna. On this scope, the near field distribution of the feed horn, which corresponds to the incident wave, is calculated firstly by using the ARM to determine the illumination pattern on the reflector surface [16].

IV. ANTENNA DESIGNS AND NUMERICAL RESULTS

A. Verification of ARM performance

The parametric analyses of the various types of reflector antennas are focused on obtaining both pencil-beam and cosecant-squared radiation patterns. The main idea of this paper is to improve the air scanning performance of air surveillance microwave radars to detect aircrafts approaching with the right angles towards to radar system. Before demonstrating the numerical results, it is important to explain the reliability of the generic ARM algorithm, which has already been verified with analytical results by achieving very good coherency for the cases of plane wave scattering from a circular cylinder, radiation from open ended waveguide, and two horn types [see 11, 16, 17, respectively]. The ARM solution of 10λ diameter (30cm at 10GHz) parabolic reflector antenna was also compared with 3D MoM simulator, and the good agreement was observed in Fig. 2.

The convergence behavior of the numerical process is highly important for the algorithm performance, as it is strictly related to the stability and processing time of the solution. The average relative computation error on the gain pattern plotted in Fig. 3 implies that ARM is a useful and reliable numerical technique due to fast

convergence and short calculation times (see also Table 3), especially for large size design and wide band analysis of the parabolic antennas.

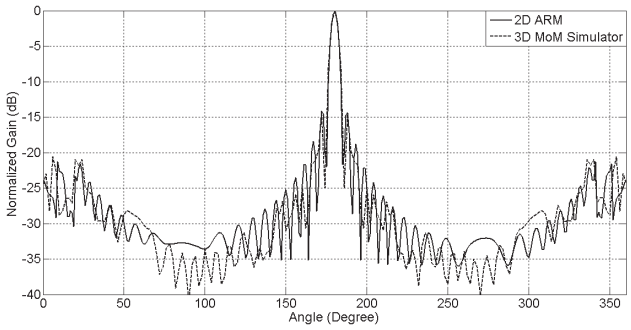

Fig. 2. Comparison of radiation patterns calculated by 2D ARM and 3D MoM simulator.

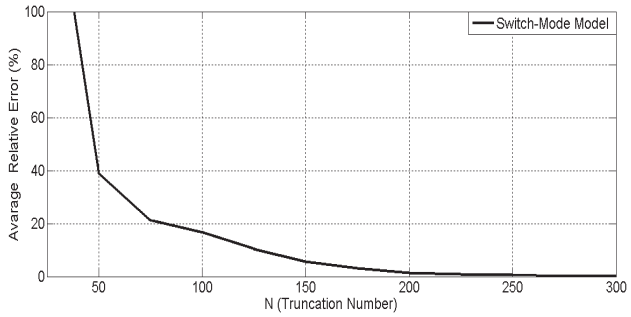

Fig. 3. Average of relative errors in numerical calculations vs. number of segments.

Table 3: Computation times of ARM and 3D MoM simulator (2.8 GHz, 4 GB RAM)

Truncation Number (*N*)	**Computation Time**	
	2D ARM	**3D MoM**
25	5 sec.	20 h.
50	34 sec.	
75	1.5 min.	
100	4 min.	
150	14 min.	
200	25 min.	
300	1.5 h.	
600	11 h.	

B. Analysis of cut-bended reflector model

At the first conventional design structure, the bottom side of classic reflector geometry is cut partially and bended by 5°, 10°, 15°, and 20°, respectively, in order to obtain cosecant-squared radiation pattern. The effects of these parameters on the far field antenna characteristics are analyzed by ARM, and the radiation patterns are demonstrated in Fig. 4. It can be clearly seen that a more bending angle is needed to reach more expanded beam on the radiation pattern. Nevertheless, it is also observed that if we bend the bottom part of the reflector over 20° the radiation pattern tends to bifurcate.

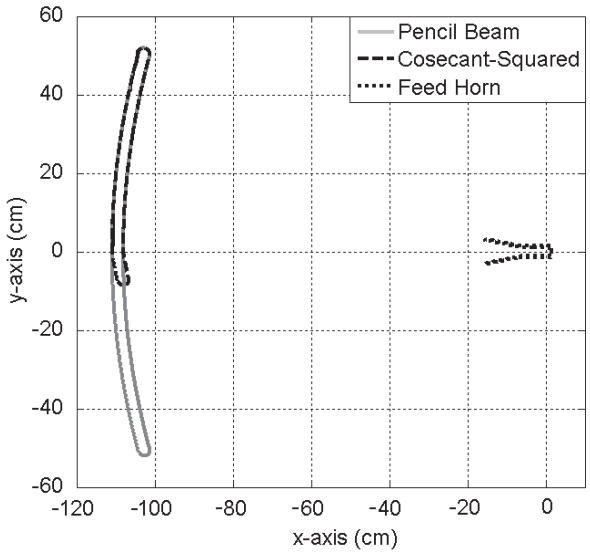

(a)

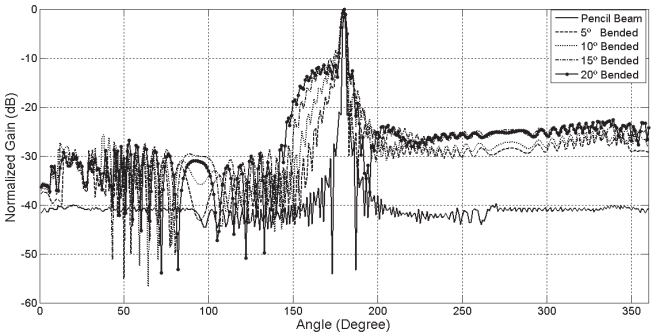

(b)

Fig. 4. (a) XOY-plane cross section of cut-bended reflector; (b) normalized radiation patterns of the structure for different bending angles (f= 10GHz).

C. Analysis of convex reflector model

In the second structure, the upper side of the reflector antenna is designed as convex to obtain cosecant-squared radiation pattern, and it is bended outwards by 5°, 10°, and 15°, respectively. It is seen at Fig. 5 that the expanding angle of the radiation pattern increases as the bending angle is increasing. However similarly, it starts to bifurcate if the convex part is bended over 15°.

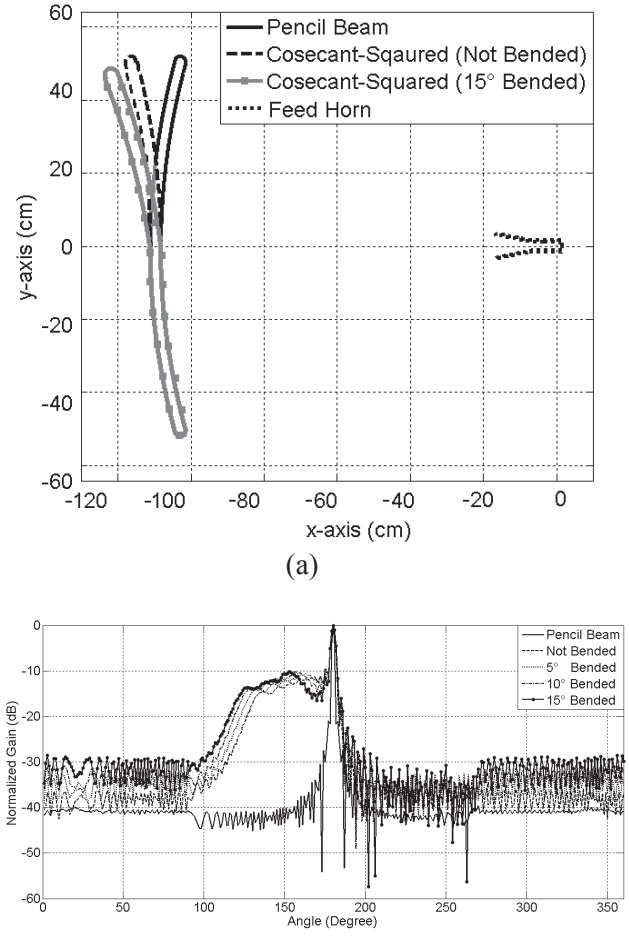

Fig. 5. (a) XOY-plane cross section of convex reflector; (b) normalized radiation patterns of the structure for different bending angles (f= 10GHz).

D. Design proposal by using asymmetric feed horn

For the aim of obtaining both pencil beam and cosecant-squared radiation patterns for the same reflector geometry, an additional cascade part with different lengths is added to the botttom of the classic reflector structure (see Fig. 1), and the antenna is illuminated by using symmetric (solid) and asymmetric (dashed) flare H-plane horn feeders as illustrated in Fig. 6a. Typical pencil beam and cosecant-squared radiation patterns can be switched just by arranging the lower flare angle of the feed horn as 11.18° (solid) and 70° (dashed), respectively. In this way, the amplitude of illumination on the cascade part, which reflects the incident signal upwards instead of into parallel, increases so that a cosecant-squared radiation pattern can appear, as shown in Fig. 6b.

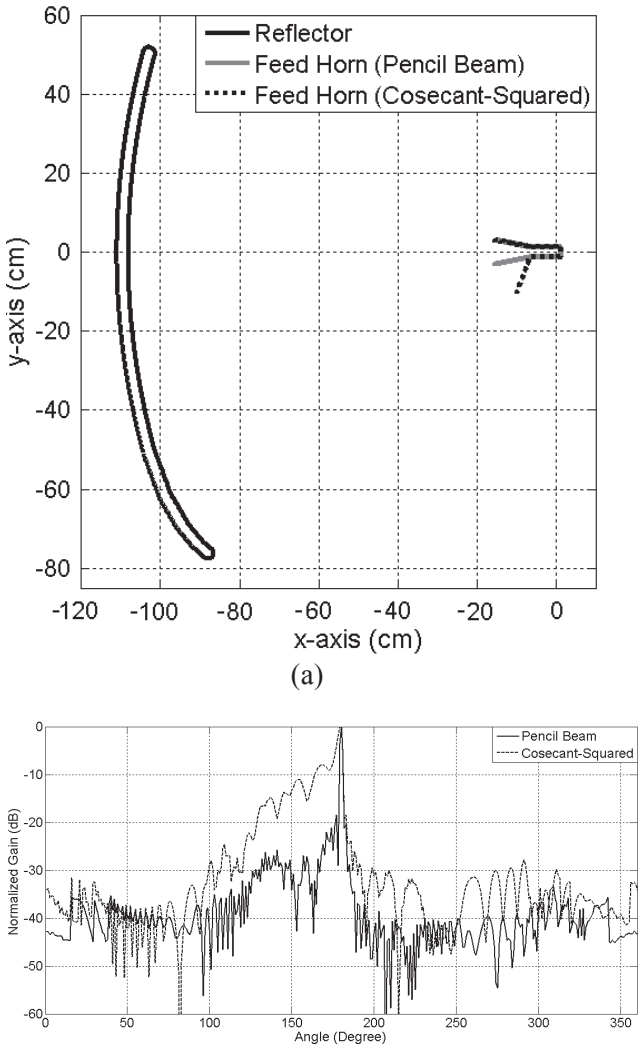

Fig. 6. (a) XOY-plane cross section of the reflector fed by symmetric and asymmetric feed horn; (b) normalized radiation patterns at f= 10GHz.

E. Design proposal by using switch-mode feed horn

This is the final design proposal with double-source feed horn located at the focus of the PEC reflector (see Fig. 1). The analysis procedure is

concentrated on obtaining both pencil beam and cosecant-squared radiation patterns without changing the geometry of feed horn and reflector antennas. In this context, if the first monopole pin of the horn located at the origin is switched on, the feed horn illuminates the reflector aperture to yield a typical pencil beam radiation pattern. In the case of switching on the second monopole pin of the horn located at coordinates x= 1.1λ, y= -0.3λ, a typical cosecant-squared radiation pattern is observed. Figure 7 exhibits the effects of pin switching between two sources of the H-plane feed horn antenna to achieve both pencil beam and cosecant-squared radiation patterns with the same feed horn and reflector geometries.

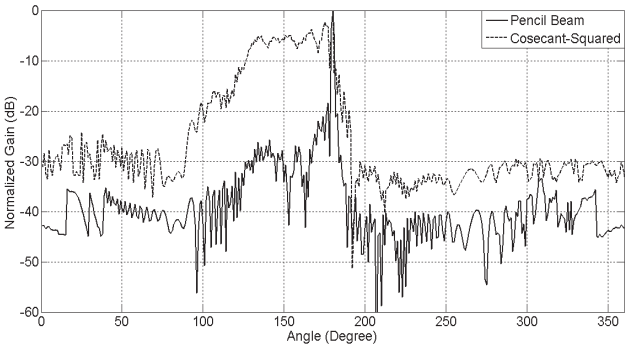

Fig. 7. Normalized radiation patterns of the switch-mode reflector antenna design at f= 10GHz (Solid line: pin 1 is ON, Dashed line: pin 2 is ON).

V. CONCLUSION

In this paper, radiation characteristics of the cylindrical parabolic reflector fed by H-plane horn are investigated parametrically to obtain pencil beam and cosecant-squared radiation patterns for air and coastal surveillance radars. Novel antenna designs are proposed to achieve switchable pencil beam and cosecant-squared radiation patterns without making any changes on the antenna geometries. Furthermore, some common cosecant-squared reflector geometries such as, cut-bended and convex shapes, are also analyzed by using the analytical regularization method, which is fast and reliable numerical-analytical technique. After verification, the analysis results of the designed reflector structures are demonstrated on the radiation patterns.

The main goal of this work in practice is to improve the air scanning performance of air and coastal surveillance radars to enable them to detect aircrafts drifting towards to radar at right angles.

REFERENCES

[1] M. I. Skolnik, "*Radar Handbook*," 2nd ed., McGraw-Hill, 1990.

[2] J. L. Volakis, *Antenna Engineering Handbook*, 4th ed., McGraw-Hill, 2007.

[3] S. Rao, M. Tang, and C. Hsu, "Multiple Beam Antenna Technology for Satellite Communications Payloads," *Applied Computational Electromagnetic Society (ACES) Journal*, vol. 21, no. 3, pp. 353-364, November 2006.

[4] T. Uno and S. Adachi, "Optimization of Aperture Illumination for Radio Wave Power Transmission," *IEEE Trans. Antennas and Propagation*, vol. 32, pp. 628-632, 1984.

[5] K. Tap and P. H. Pathak, "A Fast Hybrid Asymptotic and Numerical Physical Optics Analysis of Very Large Scanning Cylindrical Reflectors with Stacked Linear Array Feeds," *IEEE Trans. Antennas and Propagation*, vol. 54, no. 4, pp. 1142-1151, 2006.

[6] M. Djordjevic and B. M. Notaros, "Higher Order Hybrid Method of Moments-Physical Optics Modeling Technique for Radiation and Scattering from Large Perfectly Conducting Surfaces," *IEEE Trans. Antennas and Propagation,* vol. 53, no. 2, pp. 800-813, 2005.

[7] K. Umashankar and A. Taflove, "*Computational Electromagnetics*," Artech House, 1993.

[8] V. P. Chumachenko, A. S. Turk, "Radiation Characteristics of Wide-Angle H-Plane Sectoral Horn Loaded with Dielectric of Multi-Angular Shape," *Int. Journal Electronics*, vol. 88, no. 1, pp. 91-101, 2001.

[9] F. Arndt, J. Brandt, V. Catina, J. Ritter, I. Rullhusen, J. Dauelsberg, U. Hilgefort, and W. Wessel, "Fast CAD and Optimization of Waveguide Components and Aperture Antennas by Hybrid MM/FE/MoM/FD Methods: State of the Art and Recent Advances," *IEEE Trans. Microwave Theory Tech.*, vol. 52, no.1, 2004.

[10] W. Ewe, L. Li, Q. Wu, and M. Leong, "Analysis of Reflector and Horn Antennas using Adaptive Integral Methods," *IEICE Trans. Comm.*, vol. E88-B, no. 6, 2005.

[11] A. S. Turk, "Analysis of Aperture Illumination and Edge Rolling Effects for Parabolic Reflector Antenna Design,"

International Journal of Electronics and Comm. (AEUE), vol. 60, pp. 257-266, 2006.

[12] J. H. Wilkinson, "*The Algebraic Eigenvalue Problem*," Clarendon Press, Oxford, 1965.

[13] C. A. J. Fletcher, "*Computational Galerkin Method*," Springer-Verlag, Berlin, 1984.

[14] Yu. A. Tuchkin, "Wave Scattering by an Open Cylindrical Screen of Arbitrary Profile with Dirichlet Boundary Value Condition," *Soviet Physics Doclady*, vol. 30, pp. 1027-1030, 1985.

[15] E. Karacuha, A. S. Turk, "E-Polarized Scalar Wave Diffraction by Perfectly Conductive Arbitrary Shaped Cylindrical Obstacles with Finite Thickness," *Int. J. Infrared and Millimeter Waves*, vol. 22, pp. 1531-1546, 2001.

[16] A. S. Turk, O. M. Yucedag, and O. Yurduseven, "Parametric Analysis of H-Plane Horn Antenna Radiation," *Proc. 7th International Kharkov Symposium on Physics and Engineering of Microwaves, Millimeter and Sub-millimeter Waves (MSMW)*, IEEE press, Kharkov, Ukraine, pp. 21-26 June 2010.

[17] A. S. Turk and O. Yurduseven, "Parametric Analysis of Multi-Source Feeding Flare Rolling and Corrugating Effects for H-Plane Horn Radiator," *Applied Computational Electromagnetic Society (ACES) Journal*, vol. 25, no.1, January, 2011.

Ahmet Serdar Turk received the B.Sc. degree in Electronics-Communication Engineering from Yıldız Technical University, Istanbul, Turkey in 1996. He received the M.Sc. and Ph.D. degrees in Electronics Engineering from Gebze Institute of Technology, Kocaeli, Turkey in 1998 and 2001, respectively. He joined the Scientific and Technical Research Council of Turkey (TUBITAK) in 1998.

He has been working on land mine detection systems as an impulse radar RF system and antenna designer since 1998. His research interests include horn, reflector, array, and ultra-wide band antenna designs in RF and microwave bands, numerical methods in electromagnetic wave scattering, high frequency surface wave radar, ground penetrating radar, and microwave and millimeter wave radar systems.

He is currently working as associated professor at Yıldız Technical University.

Okan Yurduseven received the B.Sc. degree in Electronics-Communication Engineering from Yıldız Technical University, Istanbul, Turkey in 2009. He is currently working as research assistant in the Department of Electrical and Electronics Engineering at Marmara University, Istanbul, Turkey. His current research interests are in the areas of electromagnetic fields and waves, microwaves, antennas and propagation, radar systems, radar cross section, and numerical methods in electromagnetic theory.

Polarimetric Scattering from a 3-D Rectangular Crack in a PEC Covered by a Dielectric Layer

Mehdi Bozorgi and Ahad Tavakoli

Electrical Engineering Department
Amirkabir University of Technology, Tehran, 15914, Iran
Mehdi_Bozorgi@aut.ac.ir, Tavakoli@aut.ac.ir

Abstract ─A novel direct approach for calculation of the polarimetric scattering fields from a narrow 3-D rectangular crack in an infinite ground plane underneath a dielectric layer is presented. Since the electromagnetic fields are directly calculated and thus the approach in inversible, this technique is suitable for microwave NDT applications where cracks of narrow width, arbitrary length and depth under a dielectric layer are frequently encountered. A set of coupled field integral equations (FIE) with logarithmic and hypersingular kernels are derived and then descritized by a collocation method based on Chebyshev polynomials. The results of this direct approach are in good agreement with non-inversible full numerical FEM and MoM results.

Index Terms ─ 3-D rectangular crack, Chebyshev polynomials, dielectric layer, integral equation, and polarimetric scattering.

I. INTRODUCTION

To detect surface cracks in metals, several electromagnetic techniques are suggested [1-5]. Recently, far field polarimetric scattering measurements are proposed where common NDT techniques may not be practical such as in blast furnaces [6]. Oil, paint, electrical, and thermal coatings on cracks alters the scattering signature. For practical purposes, a solution that takes the dielectric coating effect into consideration is in demand.

Electromagnetic scattering from a dielectric coated slot in conductors is an ongoing research using various computational techniques. Initially, Knops and Cohn studied the effects of a dielectric layer on top of an aperture [7]. Later, Chen solved the integral equation for a waveguide ended with a dielectric slab and provided some physical and mathematical explanations [8]. Nevels and Butler used electric vector potential and Somerfeld integrals to model the diffraction from a slot covered by a dielectric layer [9-10]. Electromagnetic problems are generally formulated by means of the electric and the magnetic potential integral equations (PIE) [11-13]. Weak singularity of the Green's function allows utilization of a variety of numerical methods [14]. On the contrary, the electric field integral equations (EFIE) and the magnetic field integral equations (MFIE) have strong second-order singularity. Hadamard introduced the hypersingular integrals for solving Cauchy's hyperbolic partial differential problems as the finite part of a divergent integral [15]. An exact solution of the Hadamard integrals exists only in particular cases, where the hypersingular integrals are solved by approximate methods. One approach is transformation of the hypersingular integrals into singular or weakly singular integrals by various regularization techniques [16-18]. Another method that avoids singular point restrictions is the direct numerical computation of the finite part integrals by a variety of quadrature techniques.

Recently, in applied mathematics, some innovative methods are suggested to solve high order singular integrals effectively [19-20]. Thus, a strong singular EFIE or MFIE can be solved directly without using potential vectors and consequently, some tedious numerical computations such as the curl operator are

eliminated. Here, an efficient approach based on finite part sense integrals is developed for calculation of electromagnetic scattering from a dielectric coated three-dimensional crack in a grounded slab.

In Section II, a set of coupled integral equations are formulated via the continuity of the tangential magnetic fields. In Section III, the calculation of the green's functions and in Section IV, the extraction of the singular terms leaving an integrable equation is presented. In Section V, proper basis functions by considering the edge boundary conditions are presented. Then, the resultant linear matrix is solved. The scattered field due to the equivalent magnetic current under a dielectric layer is then obtained in Section VI. In Section VII, the validity and efficiency of the proposed method for calculating the scattering fields of 3-D cracks under a dielectric layer is demonstrated by comparison with MoM and FEM results.

II. THE SCATTERING PROBLEM

Assume a dielectric filled rectangular crack of $a \times b \times c$ in an infinite ground plane is coated with a dielectric slab of height d and arbitrary permittivity and permeability of ε_2, μ_2 (Fig.1). This crack is illuminated by an arbitrary polarized plane wave. Using the surface equivalence principle, we can write the scattered fields in terms of the equivalent magnetic current distribution, $\vec{M}$ on the crack as:

$$\vec{E}^s = \left\langle {}_M\bar{\bar{G}}^e . \vec{M} \right\rangle, \; \vec{H}^s = \left\langle {}_M\bar{\bar{G}}^h . \vec{M} \right\rangle, \tag{1}$$

where ${}_M\bar{\bar{G}}^e$ and ${}_M\bar{\bar{G}}^h$ are magnetic dyadic Green's functions (DGFs). The ${}_M\bar{\bar{G}}^h$ is the Green's function for the magnetic field $\vec{H}$ generated by the magnetic current $\vec{M}$. In addition, the notation $\langle , \rangle$ means the integration of products of the two functions. The integral equation is constructed by enforcing the continuity of the total tangential magnetic field on the aperture of the crack under slab that separates region 2 from region 3. Thus, we have:

$$\vec{H}_{\tan}^{\text{region1}}(2\vec{M}, \vec{J} = 0) + \vec{H}_{\tan}^{t} = \vec{H}_{\tan}^{\text{region2}}(-\vec{M}, \vec{J} = 0), \tag{2}$$

where H^t is the total tangential magnetic field in the absence of the crack. Equation (2) is broken into a pair of coupled Fredlholm's integral equations of the first kind:

$$\begin{aligned} -H_x^t &= \iint_{s'} ({}_M^C G_{xx}^h + {}_M^D G_{xx}^h) M_x ds' + \iint_{s'} ({}_M^C G_{xy}^h + {}_M^D G_{xy}^h) M_y ds' \\ -H_y^t &= \iint_{s'} ({}_M^C G_{yx}^h + {}_M^D G_{yx}^h) M_x ds' + \iint_{s'} ({}_M^C G_{yy}^h + {}_M^D G_{yy}^h) M_y ds', \end{aligned} \tag{3}$$

where ${}_M^C G_{\alpha\beta=x,y}^h$ and ${}_M^D G_{\alpha\beta=x,y}^h$ are the magnetic green's functions of the crack and the grounded dielectric slab when the source and the observation points are both on the ground plane ($z=0$). Here, a direct approach is used to convert the electric or magnetic integral equations into a simple system of linear equation based on finite part sense integrals [19]. Initially, the behavior of the Green's functions is studied for extraction of the singular terms.

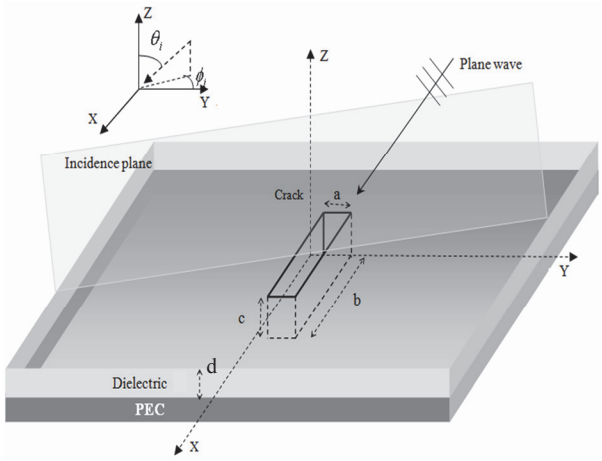

Fig. 1. Geometry of a narrow 3D-dimensional rectangular crack in an infinite ground plane underneath a dielectric layer.

III. DERIVATION OF DGFs

The most common method of deriving the DGFs is by means of Fourier transform and differential methods. Closed-form formulations of the DGFs for multilayered media using complex image method are reported in [21-29]. The well-known TL model is also used in addition to complex image method to find the spectral components of the stratified medium [22]. In Fig. 2, a magnetic current source is assumed on the infinite ground plane underneath the multilayered media. Figure 3 depicts the circuit equivalent transmission line model where the dielectric impedance is terminated by the free space wave impedance. The space domain Green's functions

are obtained by applying the Sommerfeld transformation to the TL model as [26]:

$$G_{xx}(k_\rho,z,z'=0)=-\frac{\cos 2\phi}{\rho}S_1\left\{\frac{Y_t^h-Y_t^e}{k_\rho^2}\right\}-\sin^2\phi S_0\left\{Y_t^h\right\}-\cos^2\phi S_0\left\{Y_t^e\right\}, \quad (4)$$

$$G_{xy}(k_\rho,z,z'=0)=\frac{\sin 2\phi}{\rho}S_1\left\{\frac{Y_t^h-Y_t^e}{k_\rho^2}\right\}-\frac{1}{2}\sin 2\phi S_0\left\{Y_t^h-Y_t^e\right\}, \quad (5)$$

$$G_{yx}(k_\rho,z,z'=0)=G_{xy}(k_\rho,z,z'=0), \quad (6)$$

$$G_{yy}(k_\rho,z,z'=0)=\frac{\cos 2\phi}{\rho}S_1\left\{\frac{Y_t^h-Y_t^e}{k_\rho^2}\right\}-\sin^2\phi S_0\left\{Y_t^e\right\}-\cos^2\phi S_0\left\{Y_t^h\right\}, \quad (7)$$

where $\gamma_i=\sqrt{k_\rho^2-\omega^2\mu_i\varepsilon_i}$ and $k_\rho=\sqrt{k_x^2+k_y^2}$ are cylindrical propagation constant and wave number, respectively. In the above equations, $S_n\{\ \}$ are the Sommerfeld integrals that are solved by the proper selection of branch cuts and integration paths [30].

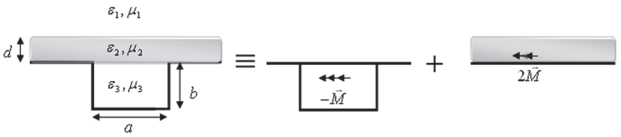

Fig. 2. The equivalence principle and image theory for a crack in an infinite ground plane.

Here, the spectral-domain Green's function is approximated by a pole-residue term plus an asymptotic function [26-28]. Thus,

$$\tilde{G}(k_\rho)\approx\sum_n a_n e^{-b_n k_\rho}+\sum_m\frac{2k_{\rho m}^p\,\mathrm{R}_m(k_{\rho m}^p)}{k_\rho^2-(k_{\rho m}^p)^2}, \quad (8)$$

$\mathrm{R}_m(k_{\rho m}^p)$ represents the residues of $\tilde{G}$ at real poles $k_{\rho m}^p$. The Prony coefficients a_n and b_n are found by using GPOF and choosing the path C by avoiding the poles $k_\rho/k_1=t\left[1+j0.1e^{(1-t)}\right],\ 0\le t\le 1.2k_{\max}/k_1$ shown in Fig. 4 [26]. In our case, the cracks are not only small but also close to the metal surface. Therefore, the lateral wave effects are small. Thus, on the conductor (z=0), we could use the approximation of DGFs. Utilizing Hankel transform,

$$\int_0^\infty e^{-\alpha k_\rho}J_n(k_\rho)(k_\rho)^{1-n}dk_\rho=\frac{n(\alpha^2+\rho^2)^{1/2}+(-1)^n\alpha}{\rho^n(\alpha^2+\rho^2)^{-n+3/2}},\qquad n=0,1. \quad (9)$$

Thus, $S_{0,1}$ in (4)-(7) are approximated as:

$$S_1\approx-\frac{j}{2}\sum_m H_1(k_{\rho m}\rho)R_m+\frac{1}{2\pi}\sum_n a_n\frac{\sqrt{\rho^2+b_n^2}-b_n}{\rho\sqrt{\rho^2+b_n^2}}, \quad (10)$$

$$S_0\approx-\frac{j}{2}\sum_m k_{\rho m}R_m H_0(k_{\rho i}\rho)+\frac{1}{2\pi}\sum_n\frac{a_n b_n}{\sqrt{(\rho^2+b_n^2)^3}}. \quad (11)$$

Since the observation points are close to the source on the ground plane, the surface waves are dominant and the residues must be calculated precisely. The method of [31] is used for extraction of poles and calculation of residues.

For the computation of the Green's functions of the cavity, various approaches such as Ewald's method are available [32- 34]. Here, we used the approach of [34] for deriving the dyadic Green's functions of the cavity because the singular behavior is represented as a sum of infinite

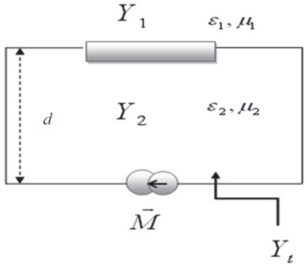

Fig. 3. Transmission line model of a magnetic source on a grounded slab.

harmonics. Since in many applications including NDT, the crack width is much smaller than the wavelength and the crack length, the DGFs are approximated by the lowest order mode of the crack [35]. Thus, the space domain Green's functions on the crack are [36]:

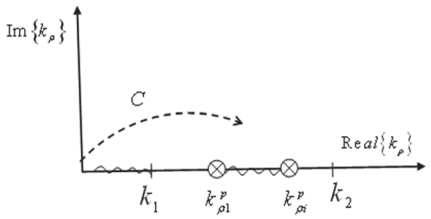

Fig. 4. The integration path in the k_ρ-plane for the sommerfeld integral.

$${}_M^C G_{xx}^h=D(k_3^2-k_x^2)\sin k_x(x'-a)\sin k_x(x-a)\sum_{p=0}^{\infty}n_p\frac{\cos k_y(y'-b)\cos k_y(y-b)}{k_z.\tan k_z c}, \quad (12)$$

$${}_M^C G_{xy}^h=Dk_x\cos k_x(x'-a)\sin k_x(x-a)\sum_{p=1}^{\infty}k_y\frac{\sin k_y(y'-b)\cos k_y(y-b)}{k_z.\tan k_z c}, \quad (13)$$

$${}_M^C G_{yx}^h=Dk_x\sin k_x(x'-a)\cos k_x(x-a)\sum_{p=1}^{\infty}k_y\frac{\cos k_y(y'-b)\sin k_y(y-b)}{k_z.\tan k_z c}, \quad (14)$$

$${}_M^C G_{yy}^h=D\sum_{p=1}^{\infty}\frac{k_3^2-k_y^2}{k_z.\tan k_z c}\sin k_y(y'-b)\sin k_y(y-b), \quad (15)$$

where $k_x=\frac{\pi}{2a}$, $k_y=\frac{p\pi}{2b}$, $k_z=\sqrt{k_3^2-k_x^2-k_y^2}$, $D=2/(j\omega\mu_3 ab)$ and n_p is the Neumann's symbol(1 for $p=0$ and 2 for $p>0$).

IV. SINGULARY EXTRACTION

The singularities in equations (4)-(7) are encountered when the observation point is on the source, *i.e.* $x = x'$ or $y = y'$ By expanding of the Hankel's functions around $y = y'$, display second-order hypersingularity and logarithmic singularity. Next, (4)-(7) are rearranged as:

$$ {}^{D}_{M}G^{h}_{xx} = \frac{f^{1}_{xx}(x,x')}{|x-x'|^{2}} + f^{2}_{xx}(x,x')\log|x-x'| + f^{3}_{xx}(x,x'), \tag{16} $$

$$ {}^{D}_{M}G^{h}_{xy} \approx {}^{D}_{M}G^{h}_{yx} \approx 0, \tag{17} $$

$$ {}^{D}_{M}G^{h}_{yy} = \frac{f^{1}_{yy}(x,x')}{|x-x'|^{2}} + f^{2}_{yy}(x,x')\log|x-x'| + f^{3}_{yy}(x,x'), \tag{18} $$

where $f^{1,2,3}$ are smooth functions obtained by the method of [6]. Note that the above procedure is repeated for all values of y and y' where $x = x'$.

The complete harmonic series of (12)-(15) either converge very slowly or diverge [6, 37]. Additionally, any truncation of the series creates a large error due to the miscalculation of the remainder of the series at $x = x'$ [6]. Therefore, the efficient approach of [37] is used to extract the singular terms of the harmonic series of (12)-(15). Considering a high enough number of modes (*i.e.,* $p > p_0$), the series coefficients are approximated as:

$$ \frac{1}{k_z.\tan k_z c} \cong \frac{1}{p} + o(p^{-3}),\ \frac{k_y}{k_z.\tan k_z c} \cong 1 + o(p^{-2}),\ \frac{k_3^2 - k_y^2}{k_z.\tan k_z c} \cong p + \frac{1}{p} + O(p^{-3}). \tag{19} $$

Finally, by substituting (19) in (12)-(15) and using the analytic simplifications of [6], the crack dyadic Green's functions are derived as:

$$ \begin{aligned} &{}^{C}_{M}G^{h}_{xx} = D(k_3^2 - k_x^2)\sin k_x(x'-a)\sin k_x(x-a) \\ &[\sum_{p=0}^{p_0} n_n \frac{\cos k_y(y'-b)\cos k_y(y-b)}{k_z.\tan k_z c} + g^{1}_{xx}\log|y-y'| + g^{2}_{xx}], \end{aligned} \tag{20} $$

$$ \begin{aligned} &{}^{C}_{M}G^{h}_{yx} \approx {}^{C}_{M}G^{h}_{xy} = Dk_x\cos k_x(x'-a)\sin k_x(x-a) \\ &[\sum_{p=1}^{p_0} \frac{k_y}{k_z.\tan k_z c}\sin k_y(y'-b)\cos k_y(y-b) + \frac{g^{1}_{xy}}{|y-y'|} + g^{2}_{xy}], \end{aligned} \tag{21} $$

$$ {}^{C}_{M}G^{h}_{yy} = D[\sum_{p=1}^{p_0} \frac{k_3^2 - k_y^2}{k_z.\tan k_z c}\sin k_y(y'-b)\sin k_y(y-b) + \frac{g^{1}_{yy}}{|y-y'|^{2}} + g^{2}_{yy}\log|y-y'| + g^{3}_{yy}], \tag{22} $$

where $g^{1,2,3}_{\alpha,\beta=x,y}$ are derivable nonsingular functions [6].

V. SOLUTION OF THE COUPLED INTEGRAL EQUATIONS

Direct integral equation solvers (DIES) straightforwardly solve the Integral equations with logarithmic or hypersingular kernels [38]. This method directly computes the finite part integral by numerical quadrature techniques that avoid the boundary singularities [19-20]. The magnetic currents at the edges of the crack are

$$ M_x(-a,y') = M(a,y) = M_y(x',-b) = M(x',b) = 0. \tag{23} $$

Please note that $M_x(x',b)$, $M_x(x',-b)$, $M_y(-a,y')$ and $M_y(a,y')$ are unknown magnetic currents on the crack and may tend to infinity at edges. By setting $s,s' = x,x'/a$ and $t,t' = y,y'/b$, the integral equation interval is transformed to $t,t',s,s' \in (-1,1)$. Next, the magnetic currents are approximated by finite series of products of two independent basic functions that satisfy the boundary conditions of (23). The first basis is a 'pulse' function and the other is a weighted Chebyshev polynomial of the second kind. Thus,

$$ M_x(s,t) \cong \sqrt{1-s^2}\sum_{m'=1}^{M}\sum_{n'=1}^{N} A_{m'n'}U_{m'-1}(s)P_{\Delta t_{n'}}(t-t_{n'}), \tag{24} $$

and

$$ M_y(s,t) \cong \sqrt{1-t^2}\sum_{m'=1}^{M}\sum_{n'=1}^{N} B_{m'n'}U_{n'-1}(t')P_{\Delta s_{m'}}(s-s_{m'}), \tag{25} $$

where $A_{m'n'}$ and $B_{m'n'}$ are unknown coefficients that must be calculated. P_{Δ} is the pulse basis functions of width $\Delta s_{m'}, \Delta t_{n'}$ where $\Delta s_{m'} = s_{m'} - s_{m'-1}\,(\Delta s_{m'} < 1)$, $\Delta s_{m'} = s_{m'} - s_{m'-1}\,(\Delta s_{m'} < 1)$. Additionally, $U_{m'}$ is the mth degree Chebyshev polynomial of the second kind. Using the zeros of $U_{m',n'}$, t_n and s_m, the surface of the crack is discretized to $M \times N$ non-equal elements. Hence,

$$ s_m = \cos\frac{m\pi}{M+1},\ m = 1,\ldots M \text{ and } t_n = \cos\frac{n\pi}{N+1},\ n = 1,\ldots N. \tag{26} $$

By substituting (24) and (25) in (3) and collocating at each t_n and s_m on the crack we have:

$$ \begin{cases} \frac{H_x(s_m,t_n)}{ab} = \sum_{n'=1}^{N}\sum_{m'=1}^{M} A_{m'n'}\left\langle K_{xx}(s_m,s'|t_n,t').O_{m'n'}(s',t')\right\rangle + \sum_{n'=1}^{N}\sum_{m'=1}^{M} B_{m'n'}\left\langle K_{xy}(s_m,s'|t_n,t').O_{m'n'}(s',t')\right\rangle \\ \frac{H_y(s_m,t_n)}{ab} = \sum_{n'=1}^{N}\sum_{m'=1}^{M} A_{m'n'}\left\langle K_{yx}(s_m,s'|t_n,t').O_{m'n'}(s',t')\right\rangle + \sum_{n'=1}^{N}\sum_{m'=1}^{M} B_{m'n'}\left\langle K_{yy}(s_m,s'|t_n,t').O_{m'n'}(s',t')\right\rangle \end{cases} \tag{27} $$

where $O^{x}_{m'n'}(s',t') = \sqrt{1-s^2}U_{m'-1}(s)P_{\Delta t_{n'}}(t-t_{n'})$ and $O^{y}_{m'n'}(s',t') = \sqrt{1-t^2}U_{n'-1}(t)P_{\Delta s_{m'}}(s-s_{m'})$. Subsequently, the coupled integral equation of (27) is represented in a linear system as:

$$ \begin{bmatrix}[H_x]\\ [H_y]\end{bmatrix} = \begin{bmatrix}[\langle K_{xx}, O^{x}_{m'n'}\rangle] & [\langle K_{xy}, O^{y}_{m'n'}\rangle]\\ [\langle K_{yx}, O^{x}_{m'n'}\rangle] & [\langle K_{yy}, O^{y}_{m'n'}\rangle]\end{bmatrix}\begin{bmatrix}[A]\\ [B]\end{bmatrix}, \tag{28} $$

where A and B are $1 \times MN$ unknown matrices that include unknown coefficients of (28) and are represented as $A = [\underbrace{A_{11},\ldots A_{1N}}, \underbrace{A_{21},\ldots A_{2N}}, \ldots \underbrace{A_{M1}\ldots A_{MN}}]$ and

$B=[\underbrace{B_{11},...B_{1N}}, \underbrace{B_{21},...B_{2N}}, ..., \underbrace{B_{M1}...B_{MN}}]$. An arbitrary incident wave of Fig 1 can be decomposed into a parallel (E) and a perpendicular (H) Polarizations as:

$$\begin{cases} \vec{H}^i = \vec{\phi} e^{jk_1[(x\cos\varphi_i + y\sin\varphi_i)\sin\theta_i + z\cos\theta_i]} & H-Pol. \\ & \varphi_i \in [0, 2\pi] \quad , \theta_i \in [0, \pi/2], \\ \vec{E}^i = \vec{\phi} e^{-jk_1[(x\cos\varphi_i + y\sin\varphi_i)\sin\theta_i + z\cos\theta_i]} & E-Pol. \end{cases} \quad (29)$$

where $k_1 = 2\pi/\lambda_0$ is the free space wave number and φ_i and θ_i are the incidence angles. The tangential magnetic field ($\vec{H}^t = \vec{H}_x\vec{x} + \vec{H}_y\vec{y}$) in the absence of the crack could be calculated by Fresnel's laws [39].

VI. FAR FIELD SCATTERING

Upon solving (3), the equivalent magnetic current on the crack is calculated and then, the far field due to this embedded source in the grounded slab is obtained [13, 40-41]. Following the approach of [41], approximate closed form solution of ${}^f_M\tilde{G}^H_\phi$ and ${}^f_M\tilde{G}^E_\phi$ are found by using the inverse Hankel transform. Thus:

$$r^2\left|(H,E)^s_\phi\right|^2 = \left|{}^f_{M_x}G^{(E,H)}_\phi(\phi_o,\theta_o)P_x(\phi_o,\theta_o) + {}^f_{M_y}G^{(E,H)}_\phi(\phi_o,\theta_o)P_y(\phi_o,\theta_o)\right|, \quad (30)$$

where

$$P_x(\phi_o,\theta_o) = \pi ab\sum_{m'=1}^{M}\sum_{n'=1}^{N} A_{m'n'} m' j^{m'-1}\frac{J_{m'-1}(X)}{X}\Delta t_{n'} e^{jt_{n'}Y}, \quad (31)$$

$$P_y(\phi_o,\theta_o) = \pi ab\sum_{m'=1}^{M-1}\sum_{n'=1}^{N-1} B_{m'n'} n' j^{n'-1}\frac{J_{n'-1}(Y)}{Y}\Delta s_{m'} e^{js_{m'}X}. \quad (32)$$

In derivation of P_x and P_y the following mathematical relation is used.

$$\int_{-1}^{1}\sqrt{1-x^2}U_{m+1}(x)e^{\alpha x}dx = \pi(m+1)j^m\frac{J_m(\alpha x)}{\alpha x}. \quad (33)$$

The α th order Bessel function of the first kind is denoted by J_α and where $X = -k_1 a\cos\phi_o\sin\theta_0$ and $Y = -k_1 b\sin\phi_o\sin\theta_0$.

VII. RESULTS

Here, few numerical examples that demonstrate the validity of this approach are presented. Assuming $a=0.1\lambda,\ b=0.8\lambda,\ c=0.25\lambda,\ h=0.1\lambda,\ \varepsilon_2=3.2-0.1j$ and $\varepsilon_3=1$ in the configuration of Fig. 1, the calculated magnetic currents distribution $|M_x|$ and $|M_y|$ at the center of the crack ($x=0$ and $y=0$) for $\phi_i=0^0$ and $\theta_i=45^0$ are depicted in Fig. 5 and Fig. 6 for parallel (E) and perpendicular (H) polarizations, respectively.

Then, the bistatic polarimetric radar cross sections ($\sigma^{bi}_{HH}, \sigma^{bi}_{VV}, \sigma^{bi}_{VH}$) at a constant observation elevation angle $\theta_o = 45^0$ are compared with the fully numerical approaches of FEM and MoM for a crack with the dielectric cover (WD) and without the dielectric cover (WoD) as shown in Fig. 7.

The dielectric cover causes σ^{bi}_{VV} to rise slightly; however, the other bistatic radar cross sections decrease by 8 dB. Figure 8 represents the same results for a constant observation azimuth angle $\phi_o = 0^0$. σ^{bi}_{VV} is almost constant while the bistatic cross polarizations increase and σ^{bi}_{HH} decreases compared to uncovered crack. As shown, the results are in a good agreement with full numerical approaches.

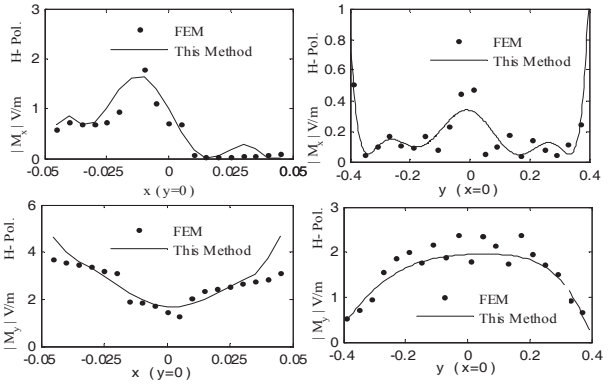

Fig. 5. Comparison between magnetic current of DIES and FEM for the crack of Fig. 1 with $a=0.1\lambda,\ b=0.8\lambda,\ c=0.25\lambda,\ h=0.1\lambda,\ \varepsilon_2=3.2-0.1j,\ \varepsilon_3=1$ for horizontal polarizations (H-Polarization) when $\phi_i=0^o$ and $\theta_i=45^o$.

In the above examples, M = 17 and N=35 with the dielectric cover and M=13 and N=29 without the dielectric cover generated accurate results. When the frequency, the permittivity, or the length of the crack increase, the Hankel's function arguments and the crack propagating modes increase as well and thus, the number of collocation points should increase for adequate accuracy. On the other hand, due to the highly oscillatory integrals, an inappropriate high number of M and N reduce the calculation efficiency without any sensible improvement [42-43].

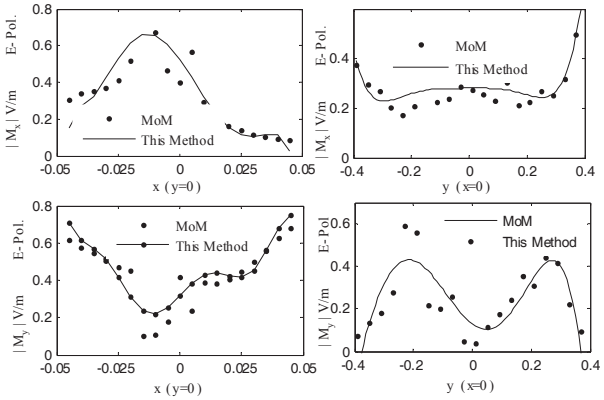

Fig. 6. Comparison between magnetic current of DIES and MoM for the crack of Fig. 1 with: $a=0.1\lambda, b=0.8\lambda,\ c=0.25\lambda, h=0.1\lambda, \varepsilon_2=3.2-0.1j$ and $\varepsilon_3=1$ for vertical polarizations (E-Polarization) at $\phi_i=0^o$ and $\theta_i=45^o$.

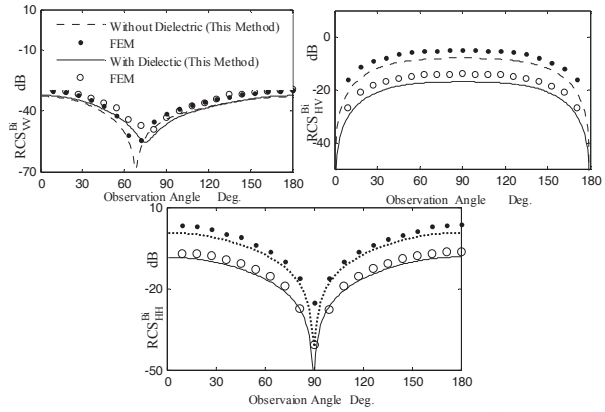

Fig. 7. Bistatic radar cross sections (RCS^{bi}) of the crack in Fig. 1 at various observation angles ϕ_o with $a=0.1\lambda, b=0.8\lambda,\ c=0.25\lambda,\ h=0.1\lambda,$ $\varepsilon_2=3.2-0.1j$ and $\varepsilon_3=1$ at $\phi_i=0^o$.

A rapid convergence of these integrals is very important in minimizing CPU time. For integrals that include Bessel and harmonic functions, an extended Levin's collocation method of [43] is used that approximates the oscillatory integrals. On a 2 GHz Pentium4 PC of 1G RAM, the computation time of FEM (HFSS), MoM (FEKO) and our method (DIES) for the dielectric covered crack of Fig. 6 are 38.136, 32.751, and 18.225 minutes, respectively. Please note that the calculation of oscillatory integrals in (3) is the most time consuming computation of DIES.

Examination of the results shows that the crack dielectric cover alters the RCS signature significantly even for thin layers. Surface waves are also a contributing factor in RCS reduction where the dielectric layer acts as a waveguide that traps the wave and thus reduces the scattered energy.

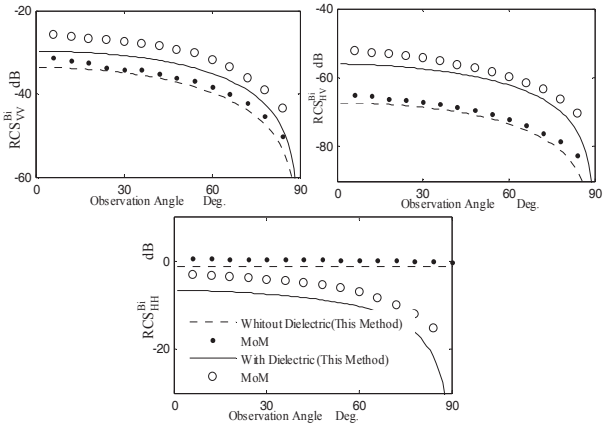

Fig. 8. RCS^{bi} of the crack in Fig. 1 at various observation angles θ_0 with $a=0.1\lambda, b=0.8\lambda,\ c=0.25\lambda,$ $h=0.1\lambda, \varepsilon_2=3.2-0.1j$ and $\varepsilon_3=1$ at $\phi_i=0^o$ and $\theta_i=45^o$.

Table1: Some material with their dielectric constants

material	permittivity
Air	1
Polystyrene	2.2
Epoxy	3.5
Glass,Mica	6
GaAs	13

Figure 9 depicts the variations of RCS^{bi} for various dielectric constants of Table 1 for $a=0.2\lambda$, $b=1\lambda$, $c=0.25\lambda, h=0.1\lambda$ and $\varepsilon_3=1$ at $\phi_i=30^0$ and $\theta_i=30^0$. By increasing the dielectric constant, RCS^{bi} drops down at first and then slowly increases due to an increase in the electrical thickness of the substrate that excites additional surface wave modes. Thus, an increase in the excitation energy in the crack causes RCS^{bi} to rise. On the contrary, as the dielectric constant increases to a large value such as $\varepsilon_2=13$, the high reflectivity at the air-dielectric interface reduces the RCS^{bi}. As the dielectric constant increases, the minimum RCS^{bi} as a function of elevation angle shifts to the left. In addition for $\varepsilon_2\le 6$, the RCS^{bi} is smoother and the scattering beam width widens for high permittivity. Referring to Fig. 9, the

energy density in the forward scattering region ($180^o < \phi_o < 360^o$) is higher than other directions due to specula reflection.

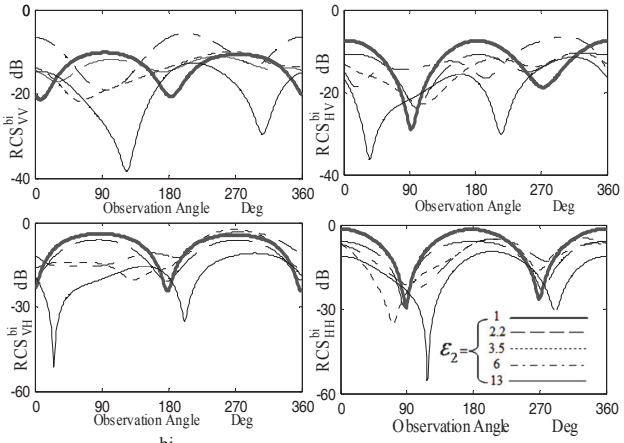

Fig. 9. RCS^{bi} of the crack in Fig. 1 versus observation angles ϕ_o or materials of table 1 where $a=0.2\lambda, b=1\lambda, c=0.25\lambda, h=0.1\lambda$ and $\varepsilon_3=1$ at $\phi_i=30^o$ and $\theta_i=30^o$.

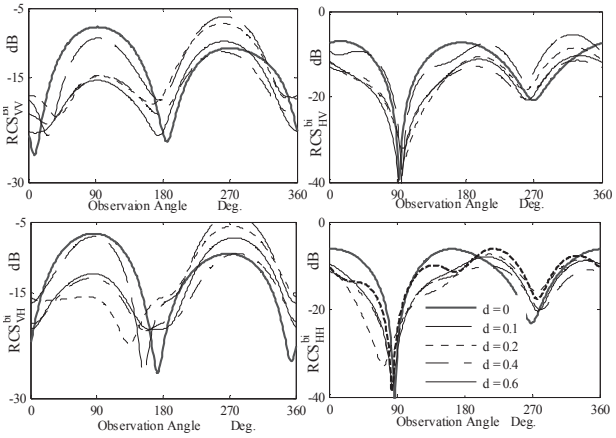

Fig. 10. RCS^{bi} of the crack in Fig. 1 versus observation angles ϕ_o for different dielectric thicknesses where $a=0.2\lambda$, $b=1\lambda$, $c=0.25\lambda, h=0.1\lambda$, $\varepsilon_2=2.5-j0.05$ and $\varepsilon_3=1$ at $\phi_i=45^o$ and $\theta_i=30^o$.

In conclusion, the dielectric constant of the layer does not have a monotonic effect on polarimetric scattering cross sections. In order to study the influence of the substrate thickness, a crack with $a=0.2\lambda$, $b=1\lambda$, $c=0.25\lambda$, $\varepsilon_2=2.5-j0.05$, $\varepsilon_3=1$ and $h=0,\ 0.1\lambda, 0.2\lambda, 0.4\lambda, 0.6\lambda$ is illuminated at $\phi_i=45^o$ and $\theta_i=30^o$ and the RCS^{bi} variations are shown in Fig. 10.

As dielectric thickness increases, the RCS^{bi} in the forward scattering region increases while in the exciting source region ($0^o < \phi_o < 180^o$) decreases. The RCS^{bi} dips for co-polarization at $\phi_o=180^o$ and $\phi_o=360^o$ and for cross-polarization at $\phi_0=90^o$ and $\phi_o=270^o$ are thickness independent. Similar to the influence of the dielectric constant, the dielectric thickness effect is not monotonic as well, noting that the surface waves are more prevalent in this case.

VIII. CONCLUSION

Most approaches in the literature use the electric and the magnetic potential integral equations to solve electromagnetic problems. Here, a direct field method is developed to solve the magnetic integral equations of a three dimensional rectangular crack in a grounded slab covered by a dielectric layer. This invertible solution is in demand in inverse scattering and NDT applications. The approach efficiently solves the integral equation by extraction of the hyper-singular terms and then descritizing the integral equation. The two-dimensional integrals include strong singularities that are approximated by ad hoc quadrature rules leading to a linear system of equations. In addition, the calculation of the oscillatory integrals is expedited by Levin's method that is developed in applied mathematics. A good agreement is observed with MoM and FEM solutions that are full numerical and non-invertible. In addition, the sensitivity of the RCS^{bi} to the permittivity and thickness of overlaying layer is investigated. In general, the dielectric layer alters the polarimetric scattering signatures of a crack in a non-monotonic manner.

Appendix: SOME QUADRATURE RULES

In equations (22-24) and (26-28), hypersingular, logarithmic and ordinary integral are present. An expression for the hypersingular integrals is in the form of [44]:

$$\int_{-1}^{1}(1-t^2)^{1/2}/|s-t|^2\, f(t)dt=\pi\sum_{j=1}^{M+1}w_j(s)f(s_j), \qquad (A.1)$$

where $f(t)$ is a given regular function and M is a integer. Here,

$$s_j=\cos j\pi/(M+2),\ (j=1,2,...,M+1), \qquad (A.2)$$

$$w_j(s) = -\frac{2}{M+2}\sum_{n=0}^{M}(n+1)\sin\left(\frac{j\pi}{M+2}\right)\sin\left(\frac{(n+1)j\pi}{M+2}\right)U_n(s) \quad \text{(A.3)}$$

$$\int_{-1}^{1} U_m(t)(1-t^2)^{1/2}/|s-t|\,dt = -\pi T_{m+1}(s) \qquad m \geq 0 \quad \text{(A.4)}$$

and T_m is the m^{th} degree Chebyshev polynomial of the first kind.

REFERENCES

[1] N. Ida, *Microwave NDT,* vol. 10, Department of Electrical Engineering, University of Akron, Ohio, 1992.

[2] R. Khalaj-Amineh, M. Ravan, S. H. H. Sadeghi, and R. Moini, "Removal of Probe Lift-Off Effects on Crack Detection and Sizing in Metals by the AC Field Measurement Technique," *IEEE Transactions on Magnetics*, vol. 44, no. 8, pp. 2066-2073, Aug. 2008.

[3] C. Huber, H. Abiri, S. Ganchev, and R. Zoughi, "Modeling of Surface Hairline-Crack Detection in Metals under Coatings using an Open-Ended Rectangular Waveguide," *IEEE Trans. on Microwave Theory and Techniques*. vol. 45, no. 11, pp. 2049-57, Nov. 1997.

[4] F. Mazlumi, S. H. H. Sadeghi, and R. Moini, "Interaction of Rectangular Open-Ended Waveguides with Surface Tilted Long Cracks in Metals," *IEEE Transactions on Instrumentation & Measurement*, vol. 55, no. 6, pp. 2191-2197, Dec. 2006.

[5] F. Deek, and M. El-Shenawee, "Microwave Detection of Cracks in Buried Pipes using the Complex Frequency Technique," *Applied Computational Electromagnetic Society* (*ACES) Journal*, vol. 25, no.10, pp. 894-902, Oct. 2010.

[6] M. Bozorgi, A. Tavakoli, G. Monegato, S. H. H. Sadeghi, and R. Moini, "Backscattering from a Two Dimensional Rectangular Crack Using FIE," *IEEE Trans. Antennas Propagat*., vol. 58, no. 2, pp. 552-564, Feb. 2010.

[7] C. M. Knop and G. I. Cohn, "Radiation from an Aperture in a Coated Plane," *Radio Science Journal of Research*, vol. GSD, pp. 363-378, Apr. 1964.

[8] C. P. Wu, "Integral Equation Solutions for the Radiation from a Waveguide through a Dielectric Slab," *IEEE Trans. Antennas Propagat*., vol.17, no. 6, pp. 733-739, Nov. 1969.

[9] R. D. Nevels, "An Analysis of a Two-Dimensional Dielectric Covered Corrugated Antenna Feed Horn," *IEEE Trans. Antennas Propagat*., vol. 32, no. 8, pp. 877-880, Aug. 1984.

[10] R. D. Nevels and C. M. Butler, "Electromagnetic Scattering by a Surface Wave from a Notch in a Ground Plane Covered by a Dielectric Slab," *J. Appl. Phys.,* vol. 52, no. 5, pp. 3145-3147, May 1981.

[11] J. W. Lee, H. J. Eom, K. H. Park, and W. J. Chun, " TM-Wave Radiation from Grooves in a Dielectric- Covered Ground Plane," *IEEE Trans. Antennas Propagat*., vol. 49, no. 1, pp. 104-105, Jan. 2001.

[12] T. F. Eibert and V. Hansen, "On the Calculation of Potential Integrals for Linear Source Distributions on Triangular Domains," *IEEE Trans. Antennas Propagat.*, vol. 43, no. 12, 1499–1502, December 1995.

[13] Yl¨a-Oijala, P. and M. Taskinen, "Calculation of CFIE Impedance Matrix Elements with RWG and n×RWG Functions," *IEEE Trans. Antennas Propagat.*, vol. 51, no. 8, 1837–1846, August 2003.

[14] H. A. Sabbagh, R. K. Murphy, E. H. Sabbagh, J. C. Aldrin, J. S. Knopp, and M. P. Blodgett, "The Joy of Computing with Volume Integrals: Validation and Performance Comparison," *Applied Computational Electromagnetic Society (ACES) Journal*, vol. 25, no. 9, pp. 731-737, September 2010.

[15] J. Hadmard, Lectures on Cauchy's Problem in Linear Partial Differential Equations. Yale University Press, Yale, 1932.

[16] A. M. Lerer and A. G. Schuchinsky, "Full-Wave Analysis of Three-Dimensional Planar Structures," *IEEE Trans. Microwave Theory and Techniques*, vol. 41, no. 11, pp. 2002-2014, 1993.

[17] A. I. Nosich, "The Method of Analytical Regularization in Wave Scattering and Eigenvalue Problems: Foundations and Review of Solutions," *IEEE Antennas and Propagation Magazine*, vol. 41, pp. 34-49, June 1999.

[18] G. Fikioris, "A Note on the Method of Analytical Regularization," *IEEE Transactions on Antennas and Progagation Magazine*, vol. 43, pp. 34-40, April 2001.

[19] G. Monegato, "Definitions, Properties, and Applications of Finite Part Integrals," *J. Comput. Appl. Math*., vol. 229, p. 425, 2009.

[20] G. Monegato, "Numerical Evaluation of Hypersingular Integrals," *J. Comput. Appl. Math.,* vol. 50, pp. 9-31, May 1994.

[21] W. C. Chew, *Waves and Fields in Inhomogeneous Media*, Van. Nostrand Reinhold, New York, 1990.

[22] Ylä-Oijala, P. and M. Taskinen, "Efficient Formulation of Closed Form Green's Functions for General Electric and Magnetic Sources in Multilayered Media," *IEEE Trans. Antennas and Propagation*, vol. 51, no. 8, pp. 2106-2115, 2003.

[23] K. A. Michalski and J. R. Mosig, "Multilayered Media Green's Functions in Integral Equation Formulations," *IEEE Trans Antennas. Propagat,*, vol. 45, no. 3, pp. 508-519, March 1997.

[24] J. Bernal, F. Medina, R. R. Boix, and M. Horno, "Fast Full-Wave Analysis of Multistrip Transmission Lines on MPIE and Complex Image Theory," *IEEE Trans. Microw. Theory Tech.*, vol. 48, no. 3, pp. 445–452, Mar. 2000.

[25] M. I. Aksun and G. Dural, "Clarification of Issues on Closed-Form Green's Functions in Stratified Media *IEEE Transactions on Antennas and Propagation*, vol. 53, no. 11, pp. 3644-3653, Nov. 2005.

[26] R. R. Boix, F. Mesa, and F. Medina, "Application of Total Least Squares to the Derivation of Closed-Form Green's Functions for Planar Layered Media," *IEEE Trans. Microw. Theory Tech.*, vol. 55, no. 2, pp. 268-280, Feb. 2007.

[27] M. T. Yuan, T. L. Sarkar, and Salazar-Palma, "A Discrete Complex Image Method from the Closed-Form Green's Functions in Multilayered Media," *IEEE Trans. Microw. Theory Tech.*, vol. 54, no. 3, pp. 1025-1032, 2006.

[28] J. R. Mosig and Alvarez-Melcon, "Green's Functions in Lossy-Layered Media: Integration Along the Imaginary Axis and Asymptotic Behavior," *IEEE Trans. Antennas Propagat.*, vol. 51, pp. 3200-3208, Dec. 2003.

[29] A. Dreher, "A New Approach to Dyadic Green's Function in Spectral Domain," *IEEE Trans. Antennas Propagat.*, vol. 43, pp. 1297-1302, Nov. 1995.

[30] K. A. Michalski, " Extrapolation Methods for Sommerfeld Integral Tails," *IEEE Trans. Antennas Propagat.*, vol. 46, no. 10, pp. 1405-14182, Oct. 1998.

[31] M. Zhang, L. W. Li, and Y. F. Tian, "An Efficient Approach for Extracting Poles of Green's Functions in General Multilayered Media," *IEEE Trans. Antennas Propagat.*, vol. 56, no. 1, pp. 269-273, Jan. 2008.

[32] D. I. Wu and D. C. Cheng, "**A** Hybrid Representation of the Green's Function in an Overmoded Rectangular Cavity," *IEEE Trans. Antennas Propagat.,* vol. 36, no. 9, pp. 1334-1342, Sep. 1988.

[33] F. Capolino, D. R. Wilton, and W. A. Johnson, "Efficient Computation of the 2D Green's Function for 1D Periodic Arrays Using the Ewald Method,"*IEEE Trans. Antennas Propagat.*, vol. 53, no. 9, pp. 2977-2984, Sept. 2005.

[34] M.-J. Park, J. Park, and S. Nam, "Efficient Calculation of the Green's Function for the Rectangular Cavity," *IEEE Microwave and Guided Wave Letters*, vol. 8, no. 3, March 1998, pp. 124-126.

[35] K. Barkashli and J. L. Volakis," Scattering from Narrow Rectangular Filled Grooves," *IEEE Trans. Antennas Propagat*., vol. AP-39, no.10, pp. 804-810, June 1991.

[36] K. Y. Chow and K. W. Leung, "Theory and Experiment of the Cavity-Backed Slot-Excited Dielectric Resonator Antenna," *IEEE Trans. Electromag. Compat.*, vol. 42, no. 3, pp. 290-297, Aug. 2000.

[37] G. Monegato, R. Orta, and R. Tascone, "A Fast Method for the Solution of a Hypersingular Integral Equation Arising in a Waveguide Scattering Problem," *Int. J. Numer. Methods Eng.* vol. 67, no. 2, pp. 272-297, July 2006.

[38] Y. Chen, "Fast Direct Solver for the Lippmann-Schwinger Integral Equation," *Adv. Comput. Math*., vol. 16, pp. 175-190, 2002.

[39] C. A. Balanis, *Antenna Theory, Analysis and Design*, 3rd Ed., John Wiley & Sons, Hoboken, NJ, 2005.

[40] B. Stockbroeckx and A. Vander Vorst, "Asymptotic Green's Function of a Surface

Magnetic Current Element on a Perfect Electric Conductor Plane Covered by a Lossy Dielectric Substrate," *IEEE Trans. Antennas Propagat*., vol. 47, no. 2, pp. 309-316, February 1999.

[41] B. Wu and L. Tsang, "Fast Computation of Layered Medium Green's Functions of Multilayers and Lossy Media using Fast All Modes Method and Numerical Modified Steepest-Descent Path Method," *IEEE Trans. Microw. Theory Tech.*, vol. 56, pp. 1446–1454, Jun. 2008.

[42] S. Xiang, "Numerical Analysis of a Fast Integration Method for Highly Oscillatory Functions," *BIT Numerical Mathmetics*, vol. 47, pp. 469-482, June, 2007.

[43] A. Molabahrami and F. Khani, "Numerical Solutions of Highly Oscillatory Integrals," *Appl. Math. Comput*., vol. 98, no. 2, pp. 657-664, 2008.

[44] M. Abramowitz and I. A. Stegun, *Handbook of Mathematical functions with formulas, Graphs, and Mathematical Tables,* vol. 55 of Applied Mathematics series, Department of commerce, National Bureau of Standards, 1972.

Mehdi bozorgi was born in Isfahan, Iran on September 4, 1977. He received B.S. and M.S degrees in Electrical Engineering from the Kashan University and the Amirkabir University of technology, respectively. In 2011, He received Ph.D. degree in Electrical Engineering at Amirkabir university of Technology, Tehran, Iran. His research field of interest is scattering of electromagnetic waves, electromagnetic nondestructive testing and optics.

Ahad Tavakoli was born in Tehran, Iran, on March 8, 1959. He received B.S. and M.S. degrees from the University of Kansas, Lawrence, and the Ph.D. degree from the University of Michigan, Ann Arbor, all in Electrical Engineering, in 1982, 1984, and 1991, respectively. In 1991, he joined the Amirkabir University of Technology, Tehran, Iran, where he is currently a Professor in the Department of Electrical Engineering. His research interests include EMC, scattering of electromagnetic waves and microstrip antennas.

An Adaptive Preconditioning Technique using Fuzzy Controller for Efficient Solution of Electric Field Integral Equations

Zhiwei Liu [1], Jiaqi Chen [1], and Rushan Chen [1,2]

[1] Department of Communication Engineering
Nanjing University of Science & Technology, Nanjing, 210094, China
zwliu1982@hotmail.com, cjq19840130@163.com, eechenrs@mail.njust.edu.cn

[2] Science and Technology on Space Microwave Laboratory, Xi'an, 710000, China
eechenrs@mail.njust.edu.cn

Abstract ― For efficiently solving large dense complex linear systems that arise in the electric field integral equation (EFIE) formulation of electromagnetic scattering problems, a new adaptive preconditioning technique using fuzzy controller (FC) is introduced and used in the context of the generalized minimal residual iterative method (GMRES) accelerated with the multilevel fast multipole method (MLFMM). The key idea is to control the choice of the preconditioner to be used in an iterative solver by using fuzzy controller. This approach allows the expert knowledge to be taken into account on the controller design and utilizes feedback to tune the cores of the fuzzy set. Numerical results show that the best preconditioner can be selected while maintaining low cost for adaptive procedures.

Index Terms ― Adaptive preconditioning technique, electric field integral equation, fuzzy controller, multilevel fast multipole method.

I. INTRODUCTION

In electromagnetic wave scattering calculations, a classic problem is to compute the induced currents on the surface of an object illuminated by a given incident plane wave. Such calculations, relying on Maxwell's equations, are crucial to the simulations of many industrial processes ranging from electromagnetic compatibility, antenna design, calculation of radar cross section (RCS), and so on. All of these simulations are very demanding in terms of computer resources, and require fast and efficient numerical methods and approximate solution of Maxwell's equations. Using the equivalence principle, Maxwell's equations can be recast in the form of integral equations that relate the electric and magnetic fields to the equivalent electric and magnetic currents on the surface of the object.

The integral formulation considered in this paper is the electric integral equation (EFIE) [1]. It is widely used for electromagnetic wave scattering problems as it can handle the most general geometries without any assumption. However, the matrix associated with the resulting linear systems is large and dense for electrically large targets in electromagnetic scattering. It is basically impractical to solve EFIE matrix equations using direct methods because they have a memory requirement of $O(N^2)$ and computational complexity of $O(N^3)$, where N refers to the number of unknowns. This difficulty can be circumvented by using Krylov iterative methods, and the required matrix-vector product operation can be efficiently evaluated by multilevel fast multipole mehthod (MLFMM) [2]. The use of MLFMM accelerated Krylov methods reduce the memory requirement to $O(N)$ and the computational complexity to $O(N\log N)$.

It is well-known that EFIE provides a first-kind integral equation which is ill-conditioned and gives rise to linear systems that are challenging to solve by the Krylov methods. Therefore, a variety of preconditioning techniques have been used to improve the conditioning of the system before the iterative solution. Simple preconditioners like the

diagonal or diagonal blocks of the coefficient matrix can be effective only when the matrix has some degree of diagonal dominance [3]. Symmetric successive over-relaxation (SSOR) preconditioner shows good performance in conjugate gradient (CG) iterative method [4], but becomes poor for nonsysmmetric systems. Incomplete LU (ILU) decomposed preconditioners have been successfully used on nonsysmmetric dense systems in [5], but the factors of the ILU preconditioner may become very ill-conditioned. Approximate inverse methods are generally less prone to instabilities on indefinite systems [6], and several preconditioners of this type have been proposed in electromagnetism. It has been shown in [7] that this technique outperforms more classical approaches like incomplete factorizations.

In this paper, we consider the performance of different predonditioners used in different problems. The choice of preconditioning methods suitable for one problem may not be the best for another one [13, 14]. Arbitrary selection in some cases lead to numerical problems like loss of convergence due to those initial choices. As an attempt for a possible remedy, a good choice of the preconditioner is made adaptively by a fuzzy controller after several iterations while maintaining low requirements for computer resources [8]. As a result, the idea of this work is to develop a general framework to dynamically change the parameters by taking into account the modeler knowledge. And the choices related to those preconditioning methods are considered as a control problem.

This paper is organized as follows. Section II gives a brief introduction to the EFIE formulation and MLFMM. Section III describes the construction and implementation of the fuzzy controller in more details. Numerical experiments with a few electromagnetic scattering problems are presented to show the efficiency of the adaptive preconditioner by FC in Section IV. Section V gives some conclusions.

II. EFIE Formulation and MLFMM

The EFIE formulation of electromagnetic wave scattering problems using planar Rao-Wilton-Glisson (RWG) basis functions for surface modeling is presented in [1]. The resulting linear systems from EFIE formulation after Galerkin's testing are briefly outlined as follows:

$$\sum_{n=1}^{N} Z_{mn} a_n = V_m, \qquad \mathrm{m} = 1, 2, ..., N, \quad (1)$$

where

$$Z_{mn} = jk \int_s \mathbf{f}_m(\mathbf{r}) \bullet \int_{s'} (\bar{\mathbf{I}} + \frac{1}{k^2} \nabla\nabla\bullet)[G(\mathbf{r}, \mathbf{r}')\mathbf{f}_n(\mathbf{r}')] ds ds'$$

$$V_m = \frac{1}{\eta} \int_s \mathbf{f}_m(\mathbf{r}) \bullet \mathbf{E}^i(\mathbf{r}) ds \,.$$

Here $G(\mathbf{r}, \mathbf{r}')$ refers to the Green's function in free space and $\{\alpha_n\}$ is the column vector containing the unknown coefficients of the surface current expansion with RWG basis functions. Also, as usual, $\mathbf{r}$ and $\mathbf{r}'$denote the observation and source point locations. $\mathbf{E}^i(\mathbf{r})$ is the incident excitation plane wave, and η and k denote the free space impendence and wave number, respectively. Once the matrix equation (1) is solved by the numerical matrix equation solvers, the expansion coefficients $\{\alpha_n\}$ can be used to calculate the scattered field and RCS. In the following, we use $\mathbf{A}$ to denote the coefficient matrix in equation (1), $\mathbf{x} = \{\alpha_n\}$, and $\mathbf{b} = \{V_m\}$ for simplicity. Then, the EFIE matrix equation (1) can be symbolically rewritten as:

$$\mathbf{Ax = b.} \quad (2)$$

To solve the above matrix equation by an iterative method, the matrix-vector products are needed at each iteration. Physically, a matrix-vector product corresponds to one cycle of iteractions between the basis functions. The basic idea of the fast multipole method (FMM) is to convert the interaction of element-to-element to the interaction of group-to-group. Here a group includes the elements residing in a spatial box. The mathematical foundation of the FMM is the addition theorem for the scalar Green's function in free space. Using the FMM, the matrix-vector product $\mathbf{Ax}$ can be written as:

$$\mathbf{Ax} = \mathbf{A}_N\mathbf{x} + \mathbf{A}_F\mathbf{x}. \quad (3)$$

Here $\mathbf{A}_N$ is the near part of $\mathbf{A}$ and $\mathbf{A}_F$ is the far part of $\mathbf{A}$.

In the FMM, the calculation of matrix elements in $\mathbf{A}_N$ remains the same as in the MoM procedure. However, those elements in $\mathbf{A}_F$ are not explicitly computed and stored. Hence, they are not numerically available in the FMM. It has been shown that the operation complexity of FMM to perform $\mathbf{Ax}$ is $0(N^{1.5})$. If the FMM is implemented

in multilevel, the total cost can be reduced further to $0(N\log N)$ [2].

III. ADAPTIVE PRECONDITIONER USING FUZZY CONTROLLER

In this section, we show how fuzzy logic provides a methodology for representing and implementing the expert knowledge about how to control the process. In particular, we apply this methodology to control the process of the preconditioner of an iterative solver. We first underline the main components and characteristic mechanisms of a FC. Afterwards, we present how to control the choice of the preconditioner using FC.

First of all, the "early steps" is defined as the first several steps of the iterative solver. If the convergence rate of the iterative solver can be evaluated approximately by the early steps. Using this information, we could decide which preconditioner is the most suitable one to accelerate the solution of the linear system. The key problem is how to evaluate the convergence rate from the early steps. In this paper, the residual of the iterative solver and the difference of the residual between two steps are used to evaluate this information.

Generally, a preconditioner corresponding to the smallest residual at the first step can be considered as the best preconditioner. However, the largest difference of the residual between the first two steps can be considered as the best precondioner. High order difference can also be used to describe the property of a preconditioner. Therefore, a fuzzy controller is used and shown in Figure 1. The *process* block is the object to be controlled. $\boldsymbol{u}(t)$ is the process input and $\boldsymbol{y}(t)$ is the process output. $\boldsymbol{r}(t)$ represents the desired target for the output of the process. The *controller* block is for changing the value of $\boldsymbol{u}(t)$ based on the controller input $\boldsymbol{y}(t)$ and the target $\boldsymbol{r}(t)$. The error as well as the rate of change-in-error defined as

$$\boldsymbol{e}(t) = \boldsymbol{r}(t) - \boldsymbol{y}(t), \tag{4}$$

$$\frac{\partial}{\partial t}\boldsymbol{e}(t) = \frac{\boldsymbol{e}(t) - \boldsymbol{e}(t-\Delta t)}{\Delta t}, \tag{5}$$

where Δt is the time between two consecutive data captured by the controller. In particular, Δt is set equal to one in an iterative solver.

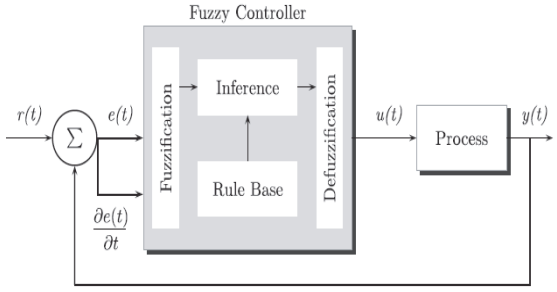

Fig. 1. Block diagram of a feedback fuzzy control.

As a controller for the choice of the preconditioner when solving equation (2), the feedback fuzzy control system takes advantage of residual at each iterative step. $\boldsymbol{u}(t)$ is the preconditioner selected by controller, $\boldsymbol{y}(t)$ is the approximate solution, and $\boldsymbol{r}(t)$ represents the right-hand-side of the equation (2). As a result, $\boldsymbol{e}(t)$ is the residual defined by

$$\boldsymbol{e}(t) = \boldsymbol{b} - \boldsymbol{A}\boldsymbol{x}(t). \tag{6}$$

Therefore, $\partial \boldsymbol{e}(t)/\partial t$ is the rate of change-in-residual which means the difference of residual between two iterative steps.

This fuzzy-logic-based approach allows expert knowledge to be taken into account on the controller design. A preconditioning method is selected by the controller with the principle that the best preconditioner performs highest convergence rate for a given problem. After several iterations, the approximate convergence rate can be defined by using the high order difference of residual which is shown as

$$\boldsymbol{rate} = \boldsymbol{e} + \partial \boldsymbol{e}/\partial t + \frac{1}{2}\partial^2 \boldsymbol{e}/\partial t^2 + \cdots \tag{7}$$

Obviously, if the order equal to the total number of iterations, the rate can describe the convergence exactly. Due to the finite computer resource, we often use two or three iterative steps to compute the approximate rate. The formulations can be defined by

$$\boldsymbol{rate} = \boldsymbol{e} + \partial \boldsymbol{e}/\partial t, \tag{8}$$

$$\boldsymbol{rate} = \boldsymbol{e} + \partial \boldsymbol{e}/\partial t + \frac{1}{2}\partial^2 \boldsymbol{e}/\partial t^2. \tag{9}$$

As a result, we choose the preconditoner with the largest convergence rate as a suitable preconditioning method.

Assume that three preconditioning methods are available ranging from Jacobi, SSOR, and SAI (sparse approximate inverse). The main steps of

this preconditioning method are described as follows:

Step 1: Construct the preconditioners by those three methods separately.

Step 2: Do several iterations by Krylov iterative methods and note the residual and change-in-residual at each step. In this paper, the number of iterations is set to be 3.

Step 3: Apply the FC to choose the best preconditioner.

Step 4: Use the best preconditonier to complete the iteration.

IV. NUMERICAL RESULTS

In this section, we show some numerical results that illustrate the effectiveness of the proposed adaptive preconditioning method for the solution of large dense linear systems arising from the discretization of EFIE formulation in electromagnetic scattering problems. In our experiments, the restarted version of GMRES(m) [9] algorithm is used as an iterative method, where m is the dimension size of Krylov subspace for GMRES. Additional details and comments on the implementation are given below:

(1) Zero vector is taken as initial approximate solution for all examples.

(2) The maximum number of iterations is limited to be 2000.

(3) The iteration process is terminated when the normwise backward error is reduced by 10^{-3} for all examples.

We investigate the performance of the adaptive preconditioner using fuzzy controller on four examples, which are shown in figures 2-5. They consist of an almond with 1815 unknowns at 3GHz, a double ogive with 2574 unknowns at 5GHz, a cube with 3366 unknowns at 350MHz, and a sphere with 3972 at 200MHz. The first two geometries come from [10], the side length of the cube is 1m and the radius of the sphere is also 1m. The numerical results of bistatic RCS for horizontal polarization are also displayed in figures 2-5 for these four geometries. All experiments are performed on a Pentium 4 with 2.66 GHz CPU and 960MB RAM in single precision.

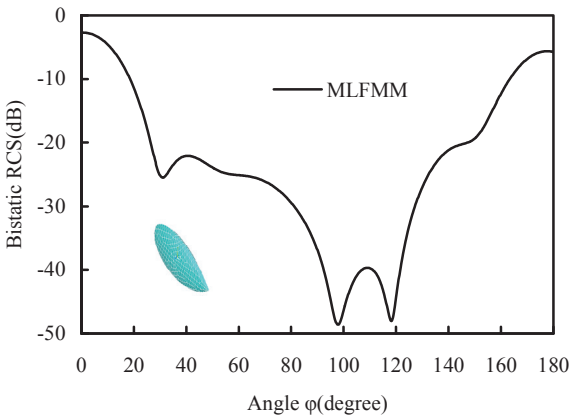

Fig. 2. Bistatic RCS for horizontal polarization at 3GHz for NASA Almond.

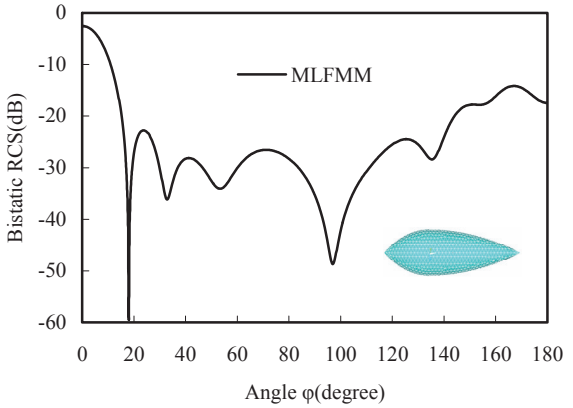

Fig. 3. Bistatic RCS for horizontal polarization at 5GHz for Double-Ogive.

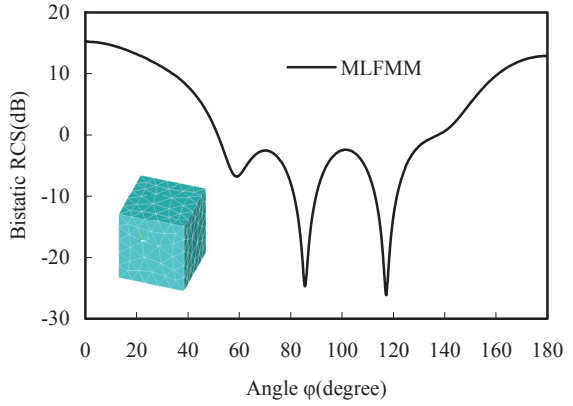

Fig. 4. Bistatic RCS for horizontal polarization at 350MHz for PEC Cube.

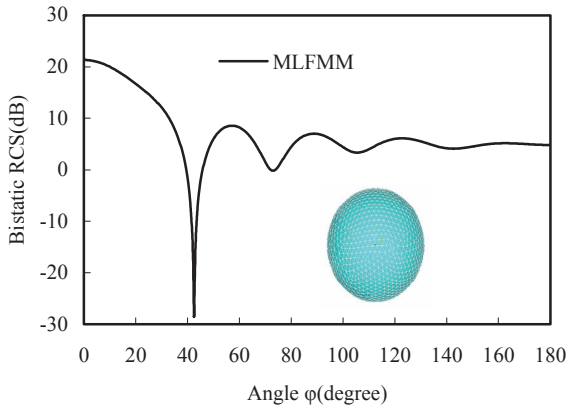

Fig. 5. Bistatic RCS for horizontal polarization at 200MHz for PEC Sphere.

Figures 6 to 9 show the convergence history of GMRES(*m*) algorithms with different preconditioners for all examples. It can be observed that the adaptive preconditioned GMRES has almost the same convergence history as that of the optimal preconditioner.

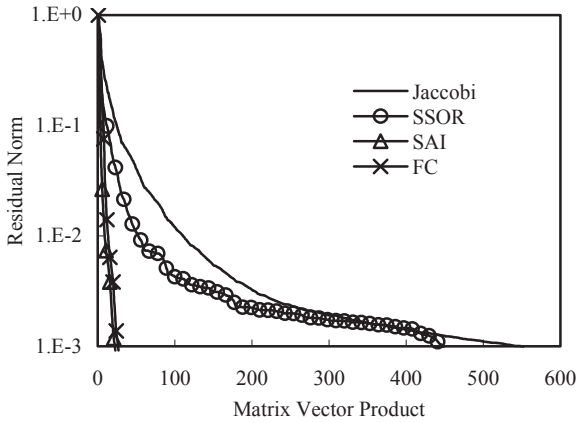

Fig. 6. Convergence history of GMRES algorithms with different preconditioners on the almond example.

Since a good preconditioner depends not only on its effect on convergence but also on its construction and implementation time. Tables 1-4 list the construction time and total solution time of GMRES algorithms with different preconditioners on all examples. According to these results, we can easily find that the proposed adaptive preconditioning method using FC requires more construction time than other preconditioners. As a control method for the choice of preconditioners, the adaptive preconditioner has to prepare all of the preconditioners for choice. Therefore, large time costs during the process of construction of all the preconditioners. However, the new method shows its efficiency on convergence in these examples. Furthermore, the initial time of adaptive preconditioner is negligible when compared with the total CPU time cost in monostatic RCS computation. Therefore, this proposed method is suitable for analysis of monostatic scattering.

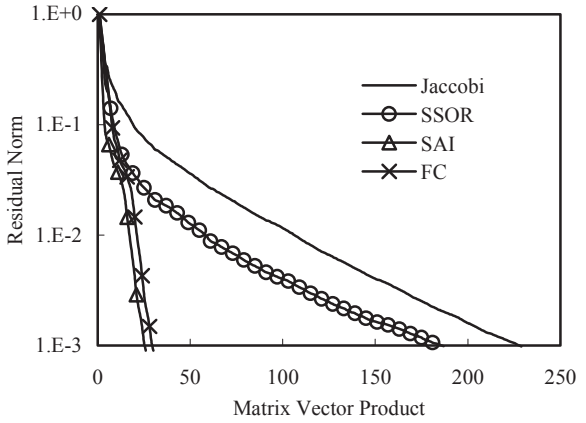

Fig. 7. Convergence history of GMRES algorithms with different preconditioners on the double-ogive example.

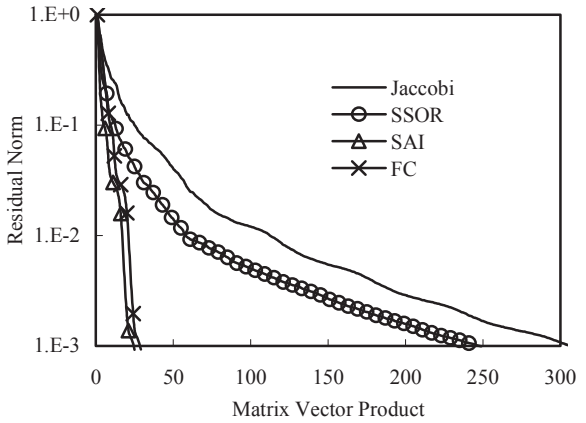

Fig. 8. Convergence history of GMRES algorithms with different preconditioners on the cube example.

V. CONCLUSIONS AND COMMENTS

In this paper, fuzzy controller is presented and used for building robust adaptive preconditioning method for efficiently solving large dense linear systems that arise in EFIE formulation of electromagnetic scattering problems. The main

idea is to make a choice of preconditioners which performs the highest convergence rate. Numerical experiments on several examples are preformed and comparison with general preconditioners are made, which shows the new method is more efficient

ACKNOWLEDGMENT

The authors would like to thank the assistance and support by the National Key Laboratory Foundation of China (No. 9140C5305021006).

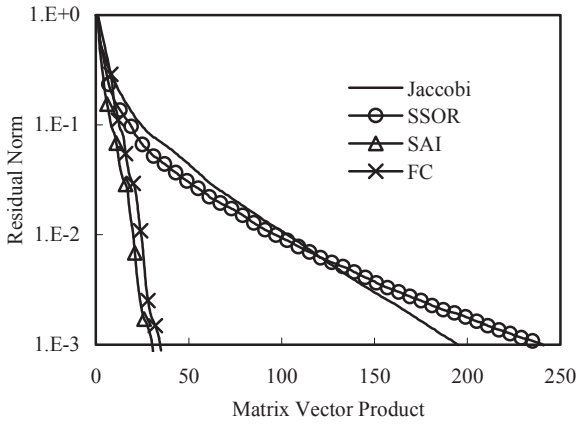

Fig. 9. Convergence history of GMRES algorithms with different preconditioners on the sphere example.

Table 1: Comparison of the cost and performance of different preconditioners on the almond example (Time: Second)

Almond	Construc-time	Number of Iterations	Sol-time	Total -time
Jacobi	/	552	31.73	31.73
SSOR	/	449	28.25	28.25
SAI	18.42	23	1.61	20.03
FC-AP	25.45	27	1.77	27.32

Table 2: Comparison of the cost and performance of different preconditioners on the double-ogive example (Time: Second)

Double ogive	Construc-time	Number of Iterations	Sol-time	Total-time
Jacobi	/	229	22.94	22.94
SSOR	/	187	20.56	20.56
SAI	11.61	26	2.86	14.47
FC-AP	16.77	30	3.19	19.96

Table 3: Comparison of the cost and performance of different preconditioners on the cube example (Time: Second)

Cube	Construc-time	Number of Iterations	Sol-time	Total -time
Jacobi	/	308	33.38	33.38
SSOR	/	249	29.91	29.91
SAI	23.02	31	3.17	26.19
FC-AP	33.45	35	3.48	36.93

Table 4: Comparison of the cost and performance of different preconditioners on the sphere example (Time: Second)

Sphere	Construc-time	Number of Iterations	Sol-time	Total-time
Jacobi	/	195	31.44	31.44
SSOR	/	241	42.02	42.02
SAI	17.33	31	5.48	22.81
FC-AP	24.72	35	5.98	30.70

REFERENCES

[1] S. M. Rao, D. R. Wilton, and A. W. Glisson, "Electromagnetic Scattering by Surfaces of Arbitrary Shape," *IEEE Transactions on Antennas and Propagation*, vol. 30, no. 3, pp. 409-418, 1982.

[2] W. C. Chew, J. M. Jin, E. Midielssen, and J. M. Song, *Fast and Efficient Algorithms in Computational Electromagnetics*. Artech House, Boston, 2001.

[3] J. M. Song, C. C. Lu, and W. C. Chew, "Multilevel Fast Multipole Algorithm for Electromagnetic Scattering by Large Complex Objects," *IEEE Transactions on Antennas and Propagation*, vol. 45, no. 10, pp. 1488-1493, 1997.

[4] S. C. Eisenstat, "Efficient Implementation of a Class of Preconditioned Conjugate Gradient Methods," *SIAM Journal on Scientific and Statistical Computing*, vol. 2, pp. 1-4, 1981.

[5] K. Sertel and J. L. Volakis, "Incomplete LU Preconditioner for FMM Implementation," *Microwave and Optical Technology Letters*, vol. 26, no. 7, pp. 265-267, 2000.

[6] B. Carpentieri, I. S. Duff, L. Griud, and G. Alleon, "Combing Fast Multipole Techniques and an Approximate Inverse Preconditioner for

Large Electromagnetism Calculations," *SIAM Journal on Scientific Computing,* vol. 27, no. 3, pp. 774-792, 2005.

[7] B. Carpentieri, I. S. Duff, and L. Griud, "Sparse Pattern Selection Strategies for Robust Frobenius-Norm Minimization Preconditioners in Electromagnetism," *Numerical Linear Algebra Applications,* vol. 7, no. 7-8, pp. 667-685, 2000.

[8] R. S. Silva and R. C. Almeida, "Using Fuzzy Controller as Adaptive Procedures in the Finite Element Method," *Communications in numerical methods in engineering*, vol. 24, no. 6, pp. 449-465, June 2008.

[9] R. B. Lehoucq, D. C. Sorensen, and C. Yang, *ARPACK User's guide: Solution of large-scale problem with implicitly restarted Arnoldi methods*, SIAM, Philadelphia, 1998.

[10] A. C. Woo, H. T. G. Wang, M. J. Schuh, and M. L. Sanders, "EM Programmer's Notebook-Benchmark Radar Targets for the Validation of Computational Electromagnetics Programs," *IEEE Antennas and Propagation Magazine*, vol. 35, no. 1, pp. 84-89, Feb. 1993.

[11] B. Carpentieri, "An Adaptive Approximate Inverse-Based Preconditioner Combined with the Fast Multipole Method for Solving Dense Linear Systems in Electromagnetic Scattering," *Applied Computational Electromagnetic Society (ACES) Journal*, vol. 24, no. 5, pp. 504-510, October 2009.

[12] J. Lee, J. Zhang, and C. Lu, "Performance of Preconditioned Krylov Iterative Methods for Solving Hybrid Integral Equations in Electromagnetics," *Applied Computational Electromagnetic Society (ACES) Journal*, vol. 18, no. 3, pp. 54-61, November 2003.

[13] D. Loqhin, D. Ruiz, and A. Touhami, "Adaptive Preconditioner for Nonlinear Systems of Equations," *Journal of Computational and Applied Mathematics*, vol. 189, issue 1-2, May 2006.

[14] M. M. Gourary, S. G. Rusakov, S. L. Ulyanov, M. M. Zharov, K. K. Gullapalli, and B. J. Mulvaney, "Adaptive Preconditioners for the Simulation of Extremely Nonlinear Circuits using Harmonic Balance," *Microwave Symposium Digest, 1999 IEEE MTT-S International*, vol. 2, pp. 779-782, 1999.

Zhiwei Liu was born in Jiangxi Province, P. R. China in 1982. He received B.S. degree in Computer Science from Nanjing Univ. of Sci. & Tech. in 2003, M.S. degree in Nanjing Institute of Electro. & Tech. in 2006, and is currently working toward the Ph.D. degree at Nanjing Univ. of Sci. & Tech. His research interests focus on theory of electromagnetic scattering and inverse scattering.

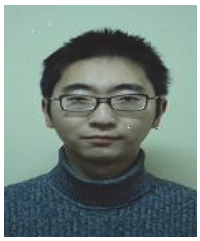

Jiaqi Chen was born in Gansu Province, P. R. China. He received the B.S. degree in Communication Engineering from Nanjing Univ. of Sci. and Tech., China, in 2005, and is currently working toward the Ph.D. degree at Nanjing Univ. of Sci. and Tech. His current research interests include computational electromagnetics, electromagnetic scattering and propagation and synthetic aperture radar imaging.

Rushan Chen (M'01) was born in Jiangsu, P. R. China. He received his B.S. and M.S. degrees from the Dept. of Radio Eng., Southeast University, in 1987 and in 1990, respectively, and his Ph.D. from the Dept. of Electronic Engineering, City University of Hong Kong in 2001. He joined the Dept. of Electrical Engineering, Nanjing Univ. of Sci. & Tech., where he became a Teaching Assistant in 1990 and a Lecturer in 1992. His research interests mainly include microwave/millimeter-wave systems, measurements, antenna, RF-integrated circuits, and computational electromagnetics.

Design Optimization of Microwave Structures Using Low-Order Local Cauchy-Approximation Surrogates

Slawomir Koziel [1] and Mohamed H. Bakr [2]

[1] Engineering Optimization & Modeling Center, School of Science and Engineering
Reykjavik University, 101 Reykjavik, Iceland
koziel@ru.is

[2] Department of Electrical and Computer Engineering, McMaster University
Hamilton, ON, Canada L8S 4K1
mbakr@mail.ece.mcmaster.ca

Abstract ─ A robust and computationally efficient microwave design optimization procedure is presented. This procedure integrates low-order Cauchy-approximation surrogate models with coarse-discretization EM simulations. The optimization engine is space mapping (SM). Instead of setting up a single surrogate model valid for the entire design variable space, a sequence of surrogate models is established in small hyper-cubes containing the optimization path. This allows us to substantially limit the number of training points necessary to create the surrogates and, therefore, reduce the cost of the optimization process. Moreover, our approach eliminates the need for circuit-equivalent coarse models traditionally used by SM algorithms. Our algorithm is successfully illustrated through the efficient design of a number of microwave filters.

Index Terms ─ Cauchy approximation, computer-aided design (CAD), EM optimization, space mapping, surrogate modeling.

I. INTRODUCTION

Accurate evaluation of microwave devices can be realized using CPU-intensive electromagnetic (EM) simulation. These simulators may require extensive simulation time for complex structures. It is, thus, prohibitive to utilize these simulators in optimizing complex structures. On the other hand, analytical models can only be used to yield initial designs that need to be further tuned to meet the given performance specifications. This is particularly true for some emerging classes of circuits such as ultra wideband (UWB) antennas [1] or substrate integrated circuits [2] where no systematic design procedures exist that would lead to designs satisfying the prescribed specifications. Therefore, EM-simulation-driven design optimization becomes increasingly important.

The computational cost of simulation-based optimization can be partially reduced by using co-simulation [3-5], where the EM model is split into smaller parts that are subsequently combined in a circuit simulator. However, the EM-embedded co-simulation model is still subjected to direct optimization. Also, application of this approach is limited and cannot be directly applied in case of radiating structures such as antennas.

Computationally efficient simulation-based optimization can be realized using surrogate-based optimization (SBO) [6, 7], where the optimization burden is shifted to a surrogate model, a computationally cheap representation of the structure being optimized (referred to as the fine model). Probably the most successful approaches of this kind are space mapping (SM) [8-19], simulation-based tuning [20-22] and tuning SM [23-26], and various response correction techniques [27-30], as well as methods utilizing variable-fidelity models [31, 32]. Using these techniques, the direct optimization of expensive (or "fine") EM-based models is replaced by

iterative optimization of less accurate but fast representations ("coarse" models). The coarse model should be physically-based (to have a good prediction capability) and it should be computationally cheap. In practice, equivalent-circuit models or models exploiting analytical formulas are preferred [6]. Unfortunately, reliable equivalent-circuit models may lack accuracy, which is critical for the SM algorithm performance [33-35]. These models may also be difficult to develop for certain types of microwave devices including antennas, substrate integrated circuits, and waveguide structures. Also, an extra simulator is involved in the optimization process.

An alternative way of creating the coarse model for SM algorithm was proposed in [36, 37] using Cauchy approximation [38] of the coarse-discretization EM simulation data of the microwave structure under consideration. The coarse model built in this way is fast and easy to optimize but the approach described in [36] can work efficiently only when the number of design variables n is small (up to 3 or 4). As the number of coarse-discretization simulations necessary to set up the coarse model grows exponentially with n, their computational cost becomes impracticably high for large n. Also, the coarse model of [36] is set up once for the entire optimization process. Thus, it should be valid in the relatively large neighborhood of the initial design which increases the required order of the Cauchy model, and consequently, the number of coarse-discretization simulations necessary to produce the training data [36].

Here, an alternative technique for creating the coarse model is described. This technique extends the work presented in [39] to problems with larger number of parameters. We exploit low-order Cauchy approximation of coarse-discretization simulation data set up in small regions enclosing the optimization path. This allows us to reduce the number of training points necessary to set up the coarse model when compared with [36]. Moreover, as the number of training points is proportional to n^2 (in particular, it does not grow exponentially with n as in [36]), our method can be applied for problems with a larger number of design variables. The efficiency of our approach is demonstrated through the design of three microstrip filters.

II. DESIGN OPTIMIZATION USING CAUCHY-BASED SURROGATES

In this section, we formulate the microwave design optimization problem, recall the standard space mapping optimization technique, and provide some general considerations regarding coarse models – the most important component of the SM algorithm. We also discuss the coarse models created by Cauchy approximation of the coarse-discretization EM-simulation data as well as describe the proposed technique exploiting low-order Cauchy approximation models.

A. Formulation of the design problem

Let $\boldsymbol{R}_f(\boldsymbol{x}) \in R^m$ denotes the response vector of the device of interest (fine model), where $\boldsymbol{x}$ is a vector of design variables (e.g., geometry parameters). $\boldsymbol{R}_f(\boldsymbol{x})$ can be, e.g., S-parameters of a device evaluated over a certain frequency band.

In this paper, a microwave design task is formulated as a nonlinear minimization problem with respect to $\boldsymbol{x}$. Design specifications are translated into a scalar merit function U, so that a better design corresponds to a smaller value of $U(\boldsymbol{R}_f(\boldsymbol{x}))$. Typically, U is a minimax function with upper and/or lower specifications [8].

The goal is to solve the following optimization problem:

$$\boldsymbol{x}_f^* \in \arg\min_{\boldsymbol{x}} U\left(\boldsymbol{R}_f(\boldsymbol{x})\right). \tag{1}$$

Here, $\boldsymbol{x}_f^*$ is the optimal design to be determined. The fine model is assumed to be computationally expensive so that handling the problem (1) directly by employing EM simulator in the optimization loop is impractical.

B. Surrogate-based optimization

Surrogate-based optimization (SBO) [6] avoids solving (1) directly for computationally expensive models. Instead, the following algorithm is considered [14]:

$$\boldsymbol{x}^{(i+1)} = \arg\min_{\boldsymbol{x}} U\left(\boldsymbol{R}_s^{(i)}(\boldsymbol{x})\right), \tag{2}$$

where $\boldsymbol{x}^{(i)}$, $i = 0, 1, \ldots$, is a series of approximate solutions to (1) with $\boldsymbol{x}^{(0)}$ being the initial design. The surrogate model $\boldsymbol{R}_s^{(i)}$ is a representation of $\boldsymbol{R}_f$ created using available fine model data, and updated after each iteration.

The construction of the surrogate model depends on the specific SBO approach. In the case of SM [8, 9], the surrogate model is a composition

of the coarse model $\boldsymbol{R}_c$ (a less accurate but computationally cheap representation of $\boldsymbol{R}_f$) and simple mappings, e.g., $\boldsymbol{R}_s^{(i)} = \boldsymbol{R}_c(\boldsymbol{B}^{(i)}\cdot\boldsymbol{x}+\boldsymbol{c}^{(i)})$ (input SM [8]) or $\boldsymbol{R}_s^{(i)} = \boldsymbol{A}^{(i)}\cdot\boldsymbol{R}_c(\boldsymbol{x}) + \boldsymbol{d}^{(i)}$ (output SM [9]). Other approaches include implicit SM [40, 41] and frequency SM [9]. The mapping parameters are determined to minimize the misalignment between the surrogate and $\boldsymbol{R}_f$, usually in a least-square sense [8].

One of the recent SBO techniques developed for microwave engineering is shape-preserving response prediction (SPRP) [30], where the surrogate model is constructed using a set of so-called characteristic points of the fine and coarse model response as well as corresponding translation vectors that describe the change of the coarse model response that is a result of the model optimization [30]. These translation vectors are subsequently applied to the fine model response at certain reference design (typically, the latest iteration point $\boldsymbol{x}^{(i)}$) in order to predict the $\boldsymbol{R}_f$ response at the current design.

Other SBO techniques, in particular, manifold mapping [27] or adaptive response correction [29], can be considered as generalizations of output SM and construct the surrogate through enhancing the coarse model by a suitable design-variable-dependent additive correction term.

C. Coarse models – general remarks

In order to ensure good performance of the SBO algorithm, regardless of whether it is space mapping, SPRP, or other technique, the coarse model should be physically-based, i.e., describe the same phenomena as the fine model which would ensure good prediction capability of the surrogate [9]. Also, $\boldsymbol{R}_c$ should be computationally cheap so that the numerous coarse model evaluations utilized while optimizing the surrogate model (2) and—in case of space mapping—solving the parameter extraction problem [8] do not seriously affect the computational cost of the algorithm.

For these reasons, the preferred choice for the coarse model is an equivalent circuit. In some cases, however, circuit-based coarse models are not available (antennas, substrate integrated circuits). Also, accuracy of such models is often insufficient, which may affect the performance of the SBO algorithm.

D. Coarse models using Cauchy approximation of coarse-discretization EM simulations

The coarse model can be implemented as a coarsely discretized EM model exploiting the same EM solver as the one used to evaluate $\boldsymbol{R}_f$ [36]. In this case, however, it is difficult to find a satisfactory trade-off between accuracy and evaluation time of $\boldsymbol{R}_c$, as well as to ensure its good analytical properties (e.g., smoothness) [42].

To overcome this problem, the coarse model can be created by approximating the data from the coarsely discretized EM model (referred to here as $\boldsymbol{R}_{f\text{-}c}$) using a suitable approximation technique. It is only necessary to evaluate the coarse EM model at a predefined set of training points. The resulting coarse model is computationally cheap.

In [34], $\boldsymbol{R}_c$ was built using a multi-dimensional Cauchy rational approximation that can be summarized as follows [38]. Let $R_s(\boldsymbol{x})$ be a scalar system response where $\boldsymbol{x} = [x_1\ x_2\ \ldots\ x_n]^T$ is the vector of design variables. The response R_s can be modeled as:

$$\overline{R}_s(\boldsymbol{x}) = \frac{a_0 + a_1x_1 + a_2x_2 + a_3x_1^2 + a_4x_1x_2 + a_5x_2^2 + .}{b_0 + b_1x_1 + b_2x_2 + b_3x_1^2 + b_4x_1x_2 + b_5x_2^2 + ..}, \quad (3)$$

where $\boldsymbol{a} = [a_0\ a_1\ \ldots\ a_M]^T$ and $\boldsymbol{b} = [b_0\ b_1\ \ldots\ b_M]^T$ are the unknown coefficients. The globally-optimal model coefficients can be found using a robust algorithm for the extraction of the parameterized Cauchy model introduced in [38]. This algorithm allows for an error margin in the given response data resulting in a stable formulation that is less sensitive to errors. It also implements safeguard constraints that eliminate spurious solutions. The model coefficients can be found by solving a linear program of the form [38]:

$$\min_{\boldsymbol{v}} \boldsymbol{c}^T\boldsymbol{v} \quad \text{subject to} \quad \boldsymbol{A}(\boldsymbol{\delta})\boldsymbol{v} \le \boldsymbol{d}, \quad (4)$$

where $\boldsymbol{v} = [t\ \ \boldsymbol{a}^T\ \ \boldsymbol{b}^T]^T$ is the vector of unknowns with t being an auxiliary variable introduced by the linear program. The matrix $\boldsymbol{A}$ depends on the set of data pairs S whose cardinality is N_s. The number of rows in the matrix $\boldsymbol{A}$ depends linearly on N_s, the vectors $\boldsymbol{c}$ and $\boldsymbol{d}$ are constant vectors whose dimensions also depend on N_s. The global optimum of the linear program (4) can always be found [38]. The vector $\boldsymbol{\delta} = [\delta_1\ \delta_2\ \ldots\ \delta_{N_s}]^T$ is the vector of tolerances defined as $R_i - \delta_i \le \overline{R}_s(\boldsymbol{x}^i) \le R_i + \delta_i$, where δ_i is the allowed tolerance for the ith data sample. In this work, the tolerances are identical for all samples and preset to a small value (typically 10^{-3}).

Let $X_B = \{\boldsymbol{x}^1, \boldsymbol{x}^2, \ldots, \boldsymbol{x}^N\}$ be a base set and $\boldsymbol{R}_{f\text{-}c}(\boldsymbol{x}) = [R_{f\text{-}c.1}(\boldsymbol{x}) \ldots R_{f\text{-}c.m}(\boldsymbol{x})]^T$. The vector $\boldsymbol{R}_{f\text{-}c}(\boldsymbol{x}^j)$ is known for $j = 1, 2, \ldots, N$.. The coarse model $\boldsymbol{R}_c$ is defined as:

$$\boldsymbol{R}_c(\boldsymbol{x}) = [\bar{R}_{f-c.1}(\boldsymbol{x}) \quad \bar{R}_{f-c.2}(\boldsymbol{x}) \quad \ldots \quad \bar{R}_{f-c.m}(\boldsymbol{x})]^T, \quad (5)$$

where $\bar{R}_{f-c.i}(\boldsymbol{x})$ is the Cauchy model of the ith component of $\boldsymbol{R}_{f\text{-}c}(\boldsymbol{x})$ constructed as described in (5).

III. LOW-ORDER LOCAL CAUCHY-APPROXIMATION SURROGATES

The coarse model (3)-(5) has a number of advantages. It is computationally cheap and easy to optimize, there is no need for a circuit-equivalent model, and the same EM solver can be used to implement both the fine and coarse model. Also, the initial design obtained through optimization of the coarse-mesh EM model is usually better than the initial design that could be possibly obtained using other methods. Unfortunately, the Cauchy-approximation model of Section II. *B* has some practical limitations. To overcome these, we propose low-order local approximation technique described in Section III. *B*.

A. Limitations of the Cauchy-approximation coarse models

The Cauchy-approximation coarse model can be used efficiently only when the number of design variables n is small (up to 3 or 4). For larger n, the required number of evaluations of $\boldsymbol{R}_{f\text{-}c}$ becomes too large (the number of training points increases exponentially with n) so that the computational cost of creating the coarse model is too high. Also, because the coarse model is set up only once for the entire optimization process, it has to have a relatively large region of validity, which results in a high (required) order of the model. This has two consequences: (i) large number of model parameters (which again increases the number of necessary training points), and (ii) difficulty in ensuring the required accuracy of the Cauchy approximation (high order rational-function approximation are highly nonlinear and their generalization capability is limited).

B. Low-order local Cauchy-approximation models

The Cauchy-based coarse model is typically set up in the neighborhood of the initial design defined by 10% to 20% deviation around the initial design. A substantial reduction of the training data can be obtained if the low-order Cauchy models are set up in smaller regions and the additional models are generated as necessary following the optimization path as explained in Fig. 1 for $n = 2$.

More specifically, the proposed approach assumes that $\boldsymbol{R}_c$ is set up locally in the neighborhood of the initial design $\boldsymbol{x}^{(0)}$ (neighborhood size $\delta_1 \times \delta_2$) and the surrogate model optimization is constrained to this neighborhood. If the new design is on the border of this neighborhood, a new $\boldsymbol{R}_c$ is created in the adjacent region. Each (local) $\boldsymbol{R}_c$ requires a small number of training data.

Setting $\boldsymbol{R}_c$ in the region of size $\Delta_1 \times \Delta_2$ enclosing the entire optimization path would require a substantially larger amount of training data (here, coarse-discretization EM simulations). For example, if $\Delta_1 = \Delta_2 = 10\%$ of $\|\boldsymbol{x}^{(0)}\|$ (relative size) and $\delta_1 = \delta_2 = 2\%$ of $\|\boldsymbol{x}^{(0)}\|$, the size of $\Delta_1 \times \Delta_2$ is 25 times larger than the size of $\delta_1 \times \delta_2$.

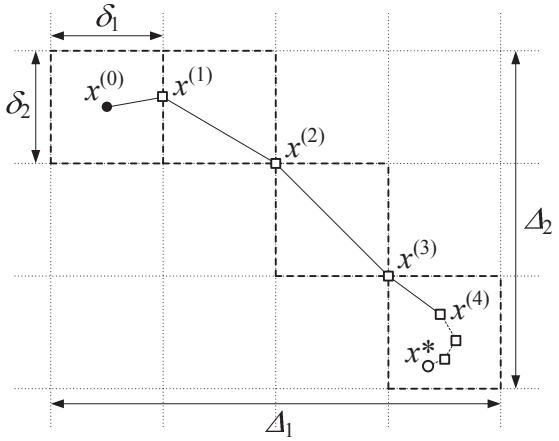

Fig. 1. Local versus quasi-global Cauchy-approximation-based coarse models (two dimensional illustration): the proposed approach assumes that the coarse model is set up locally in the neighborhood of the initial design $\boldsymbol{x}^{(0)}$ (neighborhood size $\delta_1 \times \delta_2$). The surrogate model optimization is constrained to this neighborhood. If the new design reaches the border, a new coarse model is created in the adjacent region. Each (local) coarse model requires small number of training data.

A typical optimization path that spans the entire $\Delta_1 \times \Delta_2$ region contains five $\delta_1 \times \delta_2$ cells so that the number of training points (assuming comparable model accuracy) will be 5 times smaller for the proposed approach than for the original method [36]. For example, at n = 5, the region size ratio would be 625, and the training point number ratio 125 which shows a tremendous savings when using local models. It should also be noted that the proper values of Δ_i are not known beforehand. Therefore, the proposed approach is more flexible as no initial region size estimate is necessary.

In all numerical experiments presented here, we use second-order Cauchy models that only have (n+1)(n+2) unknown coefficients. We choose the number of training points to be also equal to (n+1)(n+2). This is yet another advantage of the proposed technique because the number of unknown parameters (and, consequently, the number of training points) for high-order Cauchy models grows exponentially with n.

IV. VERIFICATION EXAMPLES

The performance of our technique exploiting local low-order Cauchy models is verified using three examples of microstrip filters. The number of design variables in these examples ranges from five to nine and cannot be handled by a "traditional" Cauchy model being set up for the entire search space.

A. 4th-order ring resonator bandpass filter [43]

Consider the fourth-order ring resonator bandpass filter [43] shown in Fig. 2. The design parameters are $\boldsymbol{x} = [L_1\ L_2\ L_3\ S_1\ S_2]^T$ mm. Other parameters are $W_1 = 1.2$ mm and $W_2 = 0.8$ mm. The fine model is simulated in FEKO [44]. The total mesh number (i.e., the total number of mesh elements) for $\boldsymbol{R}_f$ is 1334. Simulation time for $\boldsymbol{R}_f$ is 84 min. The total mesh number for the coarse-mesh FEKO model $\boldsymbol{R}_{f\text{-}c}$ is 180 (evaluation time 112 s). The design $\boldsymbol{R}_{f\text{-}c}$ specifications are $|S_{21}| \geq -1$ dB for 1.75 GHz $\leq \omega \leq$ 2.25 GHz, and $|S_{21}| \leq -20$ dB for 1.0 GHz $\leq \omega \leq$ 1.5GHz and 2.5 GHz $\leq \omega \leq$ 3.0 GHz. The initial design is $\boldsymbol{x}^{init} = [25.0\ 20.0\ 25.0\ 0.12\ 0.1]^T$ mm. The fine model specification error at $\boldsymbol{x}^{(0)}$ is +4.3 dB. The response of the fine model at $\boldsymbol{x}^{init}$ is shown in Fig. 3.

The starting point for space mapping optimization stage, $\boldsymbol{x}^{(0)} = [24.47\ 19.76\ 26.61\ 0.125\ 0.1]^T$ mm, is an approximate optimum of the coarsely discretized model; $\boldsymbol{x}^{(0)}$ is found at the cost of 60 $\boldsymbol{R}_{f\text{-}c}$ evaluations (equivalent to about 1.3 evaluations of $\boldsymbol{R}_f$). The fine model specification error at $\boldsymbol{x}^{(0)}$ is +1.3 dB.

The region size for the local Cauchy model $\boldsymbol{R}_c$ is $\boldsymbol{\delta} = [1.0\ \ 1.0\ \ 1.0\ \ 0.1\ \ 0.1]^T$ mm. We use a second-order model that has 42 coefficients. The model is established using 42 base points allocated with the Latin hypercube sampling (LHS) algorithm [45]. The surrogate model for optimization algorithm (2) is created using frequency SM [8] and output SM [9]. Figure 4 shows the responses of $\boldsymbol{R}_f$, $\boldsymbol{R}_{f\text{-}c}$ and the frequency-space-mapped $\boldsymbol{R}_c$ at $\boldsymbol{x}^{(0)}$.

The design obtained after the first iteration of the SM algorithm, $\boldsymbol{x}^{(1)} = [23.97\ 19.58\ 27.11\ 0.16\ 0.05]^T$ mm, is located at the border of the region $[\boldsymbol{x}^{(0)} - \boldsymbol{\delta}/2,\ \boldsymbol{x}^{(0)} + \boldsymbol{\delta}/2]$. According to the methodology of Section 3.2, the new coarse model is set up in the adjacent region of size $\boldsymbol{\delta}$ with the center at $[23.47\ 19.76\ 27.61\ 0.125\ 0.1]^T$ mm (the last component is not modified because 0.05 mm is set as the lower bound for the design variables S_1 and S_2). The space-mapped coarse model is then optimized. The procedure is continued for four iterations. The final design is $\boldsymbol{x}^{(4)} = [22.97\ 19.81\ 26.78\ 0.166\ 0.05]^T$ mm (specification error – 0.5 dB). Figure 5 shows the fine model response at $\boldsymbol{x}^{(4)}$. Table 1 summarizes the computational cost of the optimization: the total optimization time corresponds to less than 8 evaluations of $\boldsymbol{R}_f$.

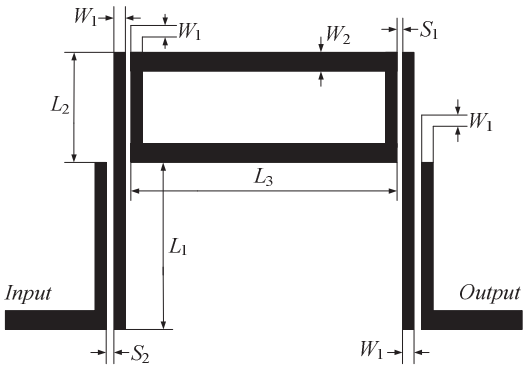

Fig. 2. Fourth-order ring resonator bandpass filter: geometry [43].

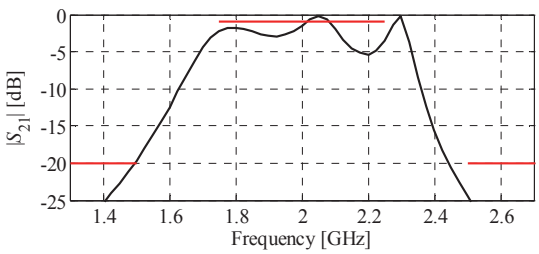

Fig. 3. Fourth-order ring resonator filter: response of the fine model $\boldsymbol{R}_f$ at the initial design $\boldsymbol{x}^{init}$.

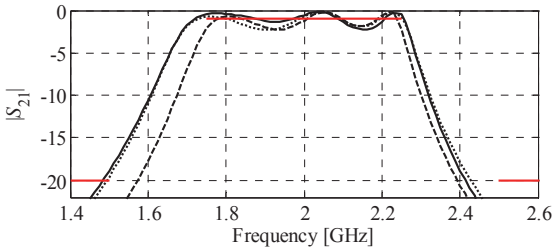

Fig. 4. Fourth-order ring resonator filter: response of the fine model $\boldsymbol{R}_f$ (solid line), coarse-mesh model $\boldsymbol{R}_{f\text{-}c}$ (dashed line) and the frequency-space-mapped coarse model (dotted line) at $\boldsymbol{x}^{(0)}$.

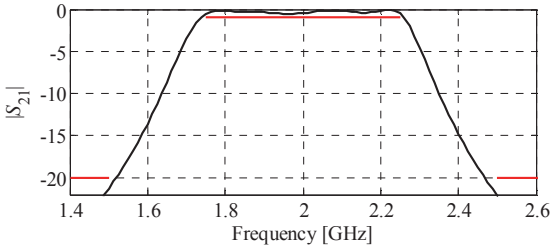

Fig. 5. Fourth-order ring resonator filter: fine model response at the final design.

Table 1: 4th-order ring resonator filter: optimization cost

Algorithm Component	Model Involved	Number of Model Evaluations	Absolute Time	Relative Cost*
Setting up Cauchy model	$\boldsymbol{R}_{f\text{-}c}$	168	5.2 h	3.7
Evaluation of the fine model	$\boldsymbol{R}_f$	4#	5.6 h	4.0
Total cost	-	-	10.8 h	7.7

* Equivalent number of fine model evaluations.
\# Excluding fine model evaluation at the initial design.

B. Bandpass filter using microstrip resonators with open stub inverter [46]

Consider the bandpass microstrip filter with open stub inverter [46] shown in Fig. 6. The design parameters are $\boldsymbol{x} = [L_1\ L_2\ L_3\ S_1\ S_2\ W_1]^T$. The fine model simulated in FEKO [44]. The total mesh number for $\boldsymbol{R}_f$ is 1702. Simulation time for $\boldsymbol{R}_f$ is 132 min. The total mesh number for the coarse-discretization FEKO model $\boldsymbol{R}_{f\text{-}c}$ is 160 (evaluation time 89 s). The design specifications are $|S_{21}| \le -20$dB for 1.5 GHz $\le \omega \le$ 1.9 GHz, $|S_{21}| \ge -1$ dB for 1.98 GHz $\le \omega \le$ 2.02 GHz and $|S_{21}| \le -20$dB for 2.1GHz $\le \omega \le$ 2.5GHz. The initial design is $\boldsymbol{x}^{init} = [25.0\ \ 5.0\ \ 25.0\ \ 1.0\ \ 0.5\ \ 2.0]^T$ mm, which is quite poor (See Fig. 7). The fine model specification error at $\boldsymbol{x}^{(0)}$ is +43.3 dB.

The initial design for space mapping optimization, $\boldsymbol{x}^{(0)} = [23.0\ \ 5.0\ \ 25.0\ \ 0.7\ \ 0.1\ \ 1.0]^T$ mm, is a rough optimum of the coarsely discretized model obtained at the cost of 55 $\boldsymbol{R}_{f\text{-}c}$ evaluations (less than one evaluation of the fine model). The fine model specification error at $\boldsymbol{x}^{(0)}$ is +3.3 dB. The region size for the local Cauchy-approximation-based $\boldsymbol{R}_c$ is $\boldsymbol{\delta} = [0.2\ 0.2\ 0.2\ 0.2\ 0.1\ 0.2]^T$ mm. We use second-order model (56 unknown coefficients) that is established using 56 base points allocated with LHS [45]. As before, the surrogate model is created using frequency SM [8] and output SM [9]. The responses of $\boldsymbol{R}_f$, $\boldsymbol{R}_{f\text{-}c}$ and frequency-space-mapped $\boldsymbol{R}_c$ at $\boldsymbol{x}^{(0)}$ are shown in Fig. 8. For this example, a very good design, $\boldsymbol{x}^{(2)} = [22.90\ 4.915\ 25.10\ 0.799\ 0.139\ 0.826]^T$ mm, is obtained after two iterations with a specification error –0.7 dB. Figure 9 shows the fine model response at $\boldsymbol{x}^{(2)}$. As indicated in Table 2, the computational cost of the optimization is very low and corresponds to only 3.3 evaluations of $\boldsymbol{R}_f$.

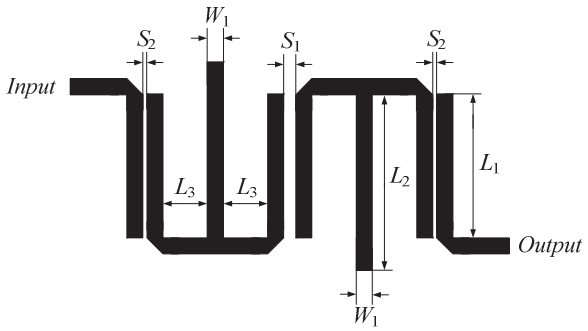

Fig. 6. Bandpass filter using microstrip resonators with open stub inverter: geometry [46].

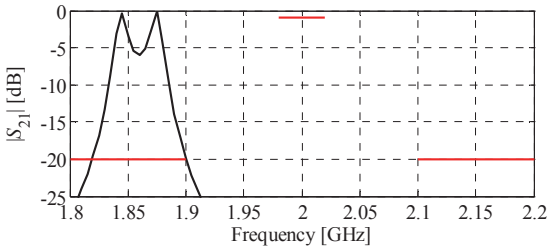

Fig. 7. Bandpass filter using microstrip resonators with with open stub inverter: response of the fine model at the initial design $\boldsymbol{x}^{init}$.

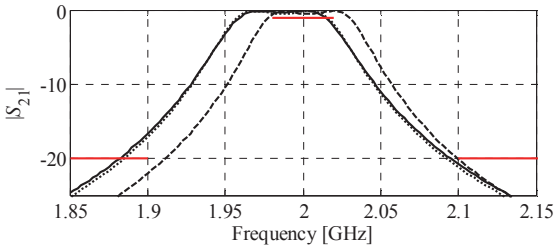

Fig. 8. Bandpass filter using microstrip resonators with with open stub inverter: response of the fine model $\boldsymbol{R}_f$ (solid line), coarse-mesh model $\boldsymbol{R}_{f\text{-}c}$ (dashed line) and the frequency-space-mapped coarse model (dotted line) at $\boldsymbol{x}^{(0)}$.

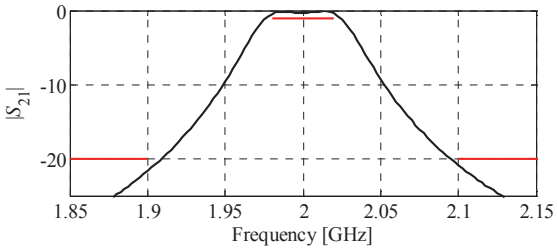

Fig. 9. Bandpass filter using microstrip resonators with with open stub inverter: fine model response at the final design.

Table 2: Bandpass filter using microstrip resonators with open stub inverter: optimization cost

Algorithm Component	Model Involved	Number of Model Evaluations	Absolute Time	Relative Cost*
Setting up Cauchy model	$\boldsymbol{R}_{f\text{-}c}$	112	2.8 h	1.3
Evaluation of the fine model	$\boldsymbol{R}_f$	2#	4.4 h	2.0
Total cost	-	-	7.2 h	3.3

* Equivalent number of fine model evaluations.
\# Excluding fine model evaluation at the initial design.

C. Microstrip hairpin filter [47]

Consider the microstrip hairpin filter [47] shown in Fig. 10. The design parameters are $\boldsymbol{x} = [L_1\ L_2\ L_3\ L_4\ L_5\ L_6\ S_1\ S_2\ d]^T$. The fine model is simulated in FEKO [44]. The total mesh number for $\boldsymbol{R}_f$ is 1424. Simulation time for $\boldsymbol{R}_f$ is 96 min. The total mesh number for the coarse-mesh FEKO model $\boldsymbol{R}_{f\text{-}c}$ is 176 (evaluation time 2 min). The design specifications are $|S_{21}| \le -20$dB for 3.0 GHz $\le \omega \le$ 3.3 GHz, $|S_{21}| \ge -0.2$ dB for 3.6 GHz $\le \omega \le$ 4.3 GHz and $|S_{21}| \le -20$dB for 4.7 GHz $\le \omega \le$ 5.0 GHz. The initial design is $\boldsymbol{x}^{init} = [10.0\ 10.0\ 10.0\ 0.5\ 1.0\ 0.5\ 0.1\ 0.2\ 0.1]^T$ mm. The fine model specification error at $\boldsymbol{x}^{init}$ is +20.6 dB. The response of the fine model at $\boldsymbol{x}^{init}$ is shown in Fig. 11.

Before performing space mapping optimization, an approximate optimum of the coarsely discretized model is found to be $\boldsymbol{x}^{(0)} = [9.9\ 11.2\ 11.35\ 0.875\ 0.75\ 0.5\ 0.125\ 0.2\ 0.8]^T$ mm. This step takes about 200 evaluations of $\boldsymbol{R}_{f\text{-}c}$ (≈ four evaluations of the fine model). The region size for the local Cauchy-approximation-based $\boldsymbol{R}_c$ is $\boldsymbol{\delta} = [0.05\ 0.05\ 0.05\ 0.05\ 0.05\ 0.05\ 0.025\ 0.025\ 0.05]^T$ mm. We use second-order model (110 unknown coefficients) that is established using 110 base points allocated with LHS [45]. Again, the surrogate model is created using frequency and output SM. The responses of $\boldsymbol{R}_f$, $\boldsymbol{R}_{f\text{-}c}$ and frequency-space-mapped $\boldsymbol{R}_c$ at $\boldsymbol{x}^{(0)}$ are shown in Fig. 12. The fine model specification error at $\boldsymbol{x}^{(0)}$ is +1.5dB. An optimized design, $\boldsymbol{x}^{(3)} = [9.9\ 11.2\ 11.325\ 0.925\ 0.7125\ 0.55\ 0.14375\ 0.2063\ 0.90]^T$ mm, is found after three iterations of our algorithm with a specification error of –0.04 dB. Figure 13 shows the fine model response at $\boldsymbol{x}^{(3)}$. The computational cost of the optimization corresponds to 10 evaluations of the fine model (Table 3).

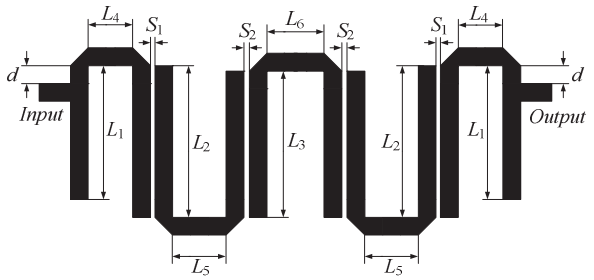

Fig. 10. The geometry of the microstrip hairpin filter [47].

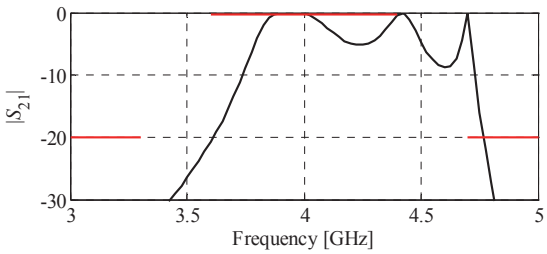

Fig. 11. Microstrip hairpin filter: response of the fine model $\boldsymbol{R}_f$ at the initial design $\boldsymbol{x}^{init}$.

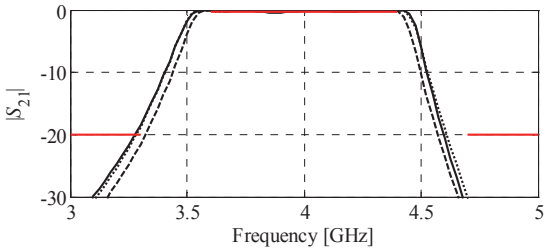

Fig. 12. Microstrip hairpin filter: response of the fine model $\boldsymbol{R}_f$ (solid line), coarse-mesh model $\boldsymbol{R}_{f\text{-}c}$ (dashed line) and the frequency-space-mapped coarse model (dotted line) at the approximate optimum of $\boldsymbol{R}_{f\text{-}c}$, $\boldsymbol{x}^{(0)}$.

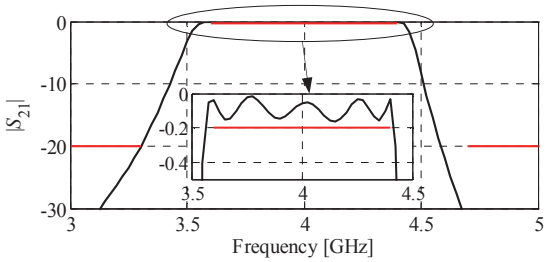

Fig. 13. Microstrip hairpin filter: fine model response at the final design.

Table 3: Microstrip hairpin filter: optimization cost

Algorithm Component	Model Involved	Number of Model Evaluations	Absolute Time	Relative Cost*
Setting up Cauchy model	$\boldsymbol{R}_{f\text{-}c}$	330	11.0 h	6.9
Evaluation of the fine model	$\boldsymbol{R}_f$	3#	4.8 h	3.0
Total cost	-	-	15.8 h	9.9

* Equivalent number of fine model evaluations.
\# Excluding fine model evaluation at the initial design.

D. Discussion

The results presented in Sections IV. *A* through IV. *C* consistently demonstrate that a combination of coarse-discretization EM models, Cauchy approximation and space mapping can make a simulation-driven design very efficient.

It should be noted that the number of space mapping iterations necessary to complete the optimization process is low (no more than four for the presented examples). It is not dependent on the problem size. On the other hand, the cost of creating the Cauchy model is $(n+1)(n+2)$ coarse-discretization model evaluations. The aforementioned facts imply that the total optimization cost scales with n as n^2 (in worst case). This is much better than for the standard approach of [36], where, as explained in Section III, the cost generally grows exponentially with n, and, building a single Cauchy model is impractical for n larger than 4 or 5.

V. CONCLUSION

Computationally efficient design optimization algorithm exploiting space mapping and the coarse model based on local low-order Cauchy approximation of coarse-discretization EM simulation data is presented. The proposed approach does not require equivalent-circuit coarse model and is not limited to problems with small number of design variables. The robustness of our technique is demonstrated through the optimization of three microstrip filters with the number of design variables ranging from five to nine. Satisfactory designs are obtained at the cost of a few EM simulations of the filter structures.

ACKNOWLEDGEMENT

This work was supported in part by the Icelandic Centre for Research (RANNIS) Grant 110034021.

REFERENCES

[1] H. Schantz, *The Art and Science of Ultrawideband Antennas*, Artech House, 2005.

[2] K. Wu, "Substrate Integrated Circuits (SiCs) – A New Paradigm for Future Ghz and Thz Electronic and Photonic Systems," *IEEE Circuits and Systems Society Newsletter,* vol. 3, no. 2, Apr. 2009.

[3] V. Rizzoli, A. Costanzo, D. Masotti, and P. Spadoni, "Circuit-Level Nonlinear/Electromagnetic Co-Simulation of

an Entire Microwave Link," *IEEE MTT-S Int. Microwave Symp. Dig.*, Long Beach, CA, pp. 813-816, June 2005.

[4] S. Shin and S. Kanamaluru, "Diplexer Design using EM and Circuit Simulation Techniques," *IEEE Microwave Magazine*, vol. 8, no. 2, pp. 77-82, Apr. 2007.

[5] R. V. Snyder, "Practical Aspects of Microwave Filter Development," *IEEE Microwave Magazine*, vol. 8, no. 2, pp. 42-54, Apr. 2007.

[6] N. V. Queipo, R. T. Haftka, W. Shyy, T. Goel, R. Vaidynathan, and P. K. Tucker, "Surrogate-Based Analysis and Optimization," *Progress in Aerospace Sciences*, vol. 41, no. 1, pp. 1-28, Jan. 2005.

[7] A. I. J. Forrester and A. J. Keane, "Recent Advances in Surrogate-Based Optimization," *Prog. in Aerospace Sciences*, vol. 45, no. 1-3, pp. 50-79, Jan.-April, 2009.

[8] J. W. Bandler, Q. S. Cheng, S. A. Dakroury, A. S. Mohamed, M. H. Bakr, K. Madsen, and J. Søndergaard, "Space Mapping: The State of the Art," *IEEE Trans. Microwave Theory Tech.*, vol. 52, no. 1, pp. 337-361, Jan. 2004.

[9] S. Koziel, J. W. Bandler, and K. Madsen, "A Space Mapping Framework for Engineering Optimization: Theory and Implementation," *IEEE Trans. Microwave Theory Tech.*, vol. 54, no. 10, pp. 3721-3730, Oct. 2006.

[10] S. Amari, C. LeDrew, and W. Menzel, "Space-Mapping Optimization of Planar Coupled-Resonator Microwave Filters," *IEEE Trans. Microwave Theory Tech.*, vol. 54, no. 5, pp. 2153-2159, May 2006.

[11] J. E. Rayas-Sánchez and V. Gutiérrez-Ayala, "EM-Based Monte Carlo Analysis and Yield Prediction of Microwave Circuits using Linear-Input Neural-Output Space Mapping," *IEEE Trans. Microwave Theory Tech.*, vol. 54, no. 12, pp. 4528-4537, Dec. 2006.

[12] X. J. Zhang and D. G. Fang, "Using Circuit Model from Layout-Level Synthesis as Coarse Model in Space Mapping and its Application in Modelling Low-Temperature Ceramic Cofired Radio Frequency Circuits," *IET Microwaves, Antennas & Propagation*, vol. 1, no. 4, pp. 881-886, Aug. 2007.

[13] L. Encica, J. J. H. Paulides, E. A. Lomonova, and A. J. A. Vandenput, "Aggressive Output Space-Mapping Optimization for Electromagnetic Actuators," *IEEE Trans. Magn.*, vol. 44, no. 6, pp. 1106-1109, 2008.

[14] S. Koziel, Q. S. Cheng, and J. W. Bandler, "Space Mapping," *IEEE Microwave Magazine*, vol. 9, no. 6, pp. 105-122, Dec. 2008.

[15] Y. Cao, L. Simonovich, and Q. J. Zhang, "A Broadband and Parametric Model of Differential Via Holes using Space-Mapping Neural Network," *IEEE Microwave Wireless Comp. Lett.*, vol. 19, no. 9, pp. 533-535, 2009.

[16] T. V. Tran, S. Brisset, P. Brochet, "A New Efficient Method for Global Multilevel Optimization Combining Branch-and-Bound and Space Mapping," *IEEE Trans. Magn.*, vol. 45, no. 3, pp. 1590-1593, 2009.

[17] J. Quyang, F. Yang, H. Zhou, Z. Nie, and Z. Zhao, "Conformal Antenna Optimization with Space Mapping," *J. of Electromagn. Waves and Appl.*, vol 24, no. 2-3, pp. 251-260, 2010.

[18] M. Dorica and D. D. Giannacopoulos, "Response Surface Space Mapping for Electromagnetic Optimization," *IEEE Trans. Magn.*, vol. 42, no. 4, pp. 1123-1126, Apr. 2006.

[19] M. F. Pantoja, P. Meincke, and A. R. Bretones, "A Hybrid Genetic-Algorithm Space-Mapping Tool for the Optimization of Antennas," *IEEE Trans. on Antennas and Propagation*, vol 55, no. 3, Part 1, pp. 777-781, March 2007.

[20] J. C. Rautio, "EM-Component-Based Design of Planar Circuits," *IEEE Microwave Magazine*, vol. 8, no. 4, pp. 79-90, Aug. 2007.

[21] D. Swanson and G. Macchiarella, "Microwave Filter Design by Synthesis and Optimization," *IEEE Microwave Magazine*, vol. 8, no. 2, pp. 55-69, Apr. 2007.

[22] J. C. Rautio, "Perfectly Calibrated Internal Ports in EM Analysis of Planar Circuits," *IEEE MTT-S Int. Microwave Symp. Dig.*, Atlanta, GA, pp. 1373-1376, June 2008.

[23] J. Meng, S. Koziel, J. W. Bandler, M. H. Bakr, and Q. S. Cheng, "Tuning Space Mapping: A Novel Technique for Engineering Design Optimization," *IEEE MTT-S Int. Microwave Symp. Dig.*, Atlanta, GA, pp. 991-994, June 2008.

[24] S. Koziel, J. Meng, J. W. Bandler, M. H. Bakr, and Q. S. Cheng, "Accelerated Microwave Design Optimization with Tuning Space Mapping," *IEEE Trans. Microwave Theory Tech.*, vol. 57, no. 2, pp. 383-394, Feb. 2009.

[25] Q. S. Cheng, J. W. Bandler, and S. Koziel, "Space Mapping Design Framework Exploiting Tuning Elements," *IEEE Trans. Microwave Theory and Tech.*, vol. 58, no. 1, pp. 136-144, 2010.

[26] S. Koziel and J. W. Bandler, "Automated Tuning Space Mapping Implementation for Rapid Design Optimization of Microwave Structures," *International Review of Progress in Applied Computational Electromagnetics*, *ACES 2009*, March 8-12, Monterey, CA, pp. 138-143, 2009.

[27] D. Echeverria, D. Lahaye, L. Encica, E. A. Lomonova, P. W. Hemker, and A. J. A. Vandenput, "Manifold-Mapping Optimization Applied to Linear Actuator Design," *IEEE Trans. Magn.*, vol. 42, no. 4, pp. 1183-1186, Apr. 2006.

[28] P. W. Hemker and D. Echeverría, "A Trust-Region Strategy for Manifold Mapping Optimization," *JCP Journal of Computational Physics*, vol. 224, no. 1, pp. 464-475, 2007.

[29] S. Koziel, J. W. Bandler, and K. Madsen, "Space Mapping with Adaptive Response Correction for Microwave Design Optimization," *IEEE Trans. Microwave Theory Tech.*, vol. 57, no. 2, pp. 478-486, 2009.

[30] S. Koziel, "Efficient Optimization of Microwave Circuits using Shape-Preserving Response Prediction," *IEEE MTT-S Int. Microwave Symp. Dig*, Boston, MA, pp. 1569-1572, 2009.

[31] S. Koziel, "Computationally Efficient Multi-Fidelity Multi-Grid Design Optimization of Microwave Structures," *Applied Computational Electromagnetic Society (ACES) Journal*, vol. 25, no. 7, pp. 578-586, July 2010.

[32] S. Koziel, "Multi-Fidelity Optimization of Microwave Structures using Response Surface Approximation and Space Mapping," *Applied Computational Electromagnetic Society (ACES*) *Journal*, vol. 24, no. 6, pp. 600–608, December 2009.

[33] S. Koziel, J. W. Bandler, and K. Madsen, "Quality Assessment of Coarse Models and Surrogates for Space Mapping Optimization," *Optimization and Engineering*, vol. 9, no. 4, pp. 375-391, 2008.

[34] S. Koziel and J. W. Bandler, "Coarse and Surrogate Model Assessment for Engineering Design Optimization with Space Mapping," *IEEE MTT-S Int. Microwave Symp. Dig*, Honolulu, HI, pp. 107-110, 2007.

[35] S. Koziel and J. W. Bandler, "Space-Mapping Optimization with Adaptive Surrogate Model," *IEEE Trans. Microwave Theory Tech*., vol. 55, no. 3, pp. 541-547, March 2007.

[36] S. Koziel, S. Ogurtsov, M. H. Bakr, and G. S. A. Shaker, "Cauchy Approximation and Coarse-Mesh EM Simulation for Multi-Fidelity Optimization of Microwave Structures," submitted, *International Review of Progress in Applied Computational Electromagnetics*, 2009.

[37] S. Koziel, S. Ogurtsov, and M. H. Bakr, "Computationally Efficient Design Optimization of Wideband Planar Antennas using Cauchy Approximation and Space Mapping," *Microwave and Optical Technology Letters*, vol. 53, no. 3, pp. 618-622, 2011.

[38] G. S. A. Shaker, M. H. Bakr, N. Sangary, and S. Safavi-Naeini, "Accelerated Antenna Design Methodology Exploiting Parameterized Cauchy Models," *J. Progress in Electromagnetic Research (PIER B*), vol. 18, pp. 279-309, 2009.

[39] S. Koziel and M. H. Bakr, "Multi-Fidelity Optimization of Microwave Structures using Low-Order Local Cauchy-Approximation Surrogates," *Int. Symp. Antenna Technology and Applied Electromagnetics*, *ANTEM 2010*, Ottawa, Canada, 2010.

[40] J. W. Bandler, Q. S. Cheng, N. K. Nikolova, and M. A. Ismail, "Implicit Space Mapping Optimization Exploiting Preassigned Parameters," *IEEE Trans. Microwave Theory Tech*., vol. 52, no. 1, pp. 378-385, Jan. 2004.

[41] Q. S. Cheng, J. W. Bandler, and S. Koziel, "An Accurate Microstrip Hairpin Filter Design using Implicit Space Mapping,"

Microwave Magazine, vol. 9, no. 1, pp. 79-88, Feb. 2008.

[42] J. Zhu, J. W. Bandler, N. K. Nikolova, and S. Koziel, "Antenna Optimization Through Space Mapping," *IEEE Transactions on Antennas and Propagation*, vol. 55, no. 3, pp. 651-658, March 2007.

[43] M. H. M. Salleh, G. Prigent, O. Pigaglio, and R. Crampagne, "Quarter-Wavelength Side-Coupled Ring Resonator for Bandpass Filters," *IEEE Trans. Microwave Theory Tech.*, vol. 56, no. 1, pp. 156-162, Jan. 2008.

[44] FEKO® *User's Manual*, Suite 5.4, EM Software & Systems-S.A. (Pty) Ltd, 32 Techno Lane, Technopark, Stellenbosch, 7600, South Africa, 2008.

[45] B. Beachkofski and R. Grandhi, "Improved Distributed Hypercube Sampling," *American Institute of Aeronautics and Astronautics*, paper AIAA 2002-1274, 2002.

[46] J. R. Lee, J. H. Cho, and S. W. Yun, "New Compact Bandpass Filter using Microstrip $\lambda/4$ Resonators with Open Stub Inverter," *IEEE Microwave and Guided Wave Letters*, vol. 10, no. 12, pp. 526-527, Dec. 2000.

[47] D. Brady, "The Design, Fabrication and Measurement of Microstrip Filter and Coupler Circuits," *High Freq. Electronics*, vol. 1, no. 1, pp. 22-30, July 2002.

Slawomir Koziel received the M.Sc. and Ph.D. degrees in Electronic Engineering from Gdansk University of Technology, Poland, in 1995 and 2000, respectively. He also received the M.Sc. degrees in Theoretical Physics and in Mathematics, in 2000 and 2002, respectively, as well as the Ph.D. in Mathematics in 2003, from the University of Gdansk, Poland. He is currently an Associate Professor with the School of Science and Engineering, Reykjavik University, Iceland. His research interests include CAD and modeling of microwave circuits, surrogate-based optimization, space mapping, circuit theory, analog signal processing, evolutionary computation, and numerical analysis.

Mohamed H. Bakr received the B.Sc. and M.Sc. degrees in Electronics and Communications Engineering and Engineering Mathematics from Cairo University, Egypt, in 1992 and 1996, respectively with distinction (honors). He earned the Ph.D. degree in 2000 from McMaster University, followed by a year as NSERC Post Doctoral Fellow with the Computational Electromagnetics Research Laboratory, University of Victoria, Canada. He is currently an associate professor at McMaster University. His research areas of interest include computer-aided design and modeling of microwave and photonic circuits, and bioelectromagnetism. He is a principal contributor to the theories of electromagnetic adjoint sensitivities and space mapping optimization.

Design of Miniaturized Unequal Split Wilkinson Power Divider with Harmonics Suppression Using Non-Uniform Transmission Lines

Khair Al Shamaileh[1], Abdullah Qaroot[2], Nihad Dib[1], and Abdelfattah Sheta[3]

[1] Electrical Engineering Department, Jordan University of Science and Technology
P. O. Box 3030, Irbid 22110, Jordan
khair_ra@yahoo.com, nihad@just.edu.jo

[2]Electrical Engineering Department, King Faisal University
P. O. Box 400, Al-Ahsa 31982, KSA
abd_mazen@hotmail.com

[3] Electrical Engineering Department, King Saud University
P. O. Box 800, Riyadh 11421, KSA
asheta@ksu.edu.sa

Abstract - In this paper, a design of an unequal split Wilkinson power divider (WPD), with high power split ratio, using non-uniform transmission lines (NTLs) is presented. The design is based on using NTLs in each branch of the divider instead of the conventional uniform ones. Besides the achievement of high power split ratio, the size of the designed WPD is reduced. The design procedure is presented for arbitrary design frequency and arbitrary power split ratio. For verification purposes, a 10:1 WPD is designed and fabricated. Good isolation between the output ports, input/output ports matching, and transmission responses are achieved at the design frequency. The experimental and full-wave simulation results show the validity of the designed NTL-WPD. Compared to the conventional design, it is noticed that the proposed divider is more likely suitable for narrowband applications.

Index Terms **-**Non-uniform transmission lines, size reduction, unequal split, Wilkinson power divider.

I. INTRODUCTION

Recently, the design of unequal split Wilkinson power dividers (WPDs) with high power split ratio has attracted much attention and interest. Several different structures have been proposed in the literature to overcome the high characteristic impedance microstrip transmission line required in the WPD with high split ratio. Many papers presented the design of defected ground structures (DGS) and its application in WPDs and branch line couplers [1-6]. In [7], a grooved substrate was proposed for the design of unequal split WPD. The grooves were applied along the strips which required high characteristic impedance which may increase the degree of complexity in fabrication process. A CPW with electromagnetic bandgap was proposed in [8] for designing a transmission line with high characteristic impedance, which was then applied to the design of unequal split WPDs. Nevertheless, the design and realization are even more complex. A 10:1 unequal split WPD using coupled lines with two shorts was presented in [9]. The very thin microstrip transmission line was mitigated using a coupled line with two shorted ends.

In this paper, based on the simple WPD topology proposed in [10], a compact unequal

split WPD with high split ratio is designed and fabricated using non-uniform transmission lines (NTLs) theory [11]. The same theory was used in [12] and [13] to design miniaturized dual-frequency WPD and multi-frequency Bagley polygon divider (BPD), respectively. Recently, equivalent circuits for NTLs were proposed in [14].

II. DESIGN OF COMPACT NTLs [11]

In this section, the theory of designing compact NTLs is briefly presented. Figure 1(a) shows a typical uniform transmission line with a length, characteristic impedance and propagation constant of d_0, Z_0 and β_0, respectively, with an ABCD parameters matrix [15]:

$$\begin{bmatrix} A_0 & B_0 \\ C_0 & D_0 \end{bmatrix} = \begin{bmatrix} \cos(\theta) & jZ_0 \sin(\theta) \\ jZ_0^{-1} \sin(\theta) & \cos(\theta) \end{bmatrix}, \quad (1)$$

where $\theta = \beta_0 d_0$ is the electrical length of the desired uniform transmission line. Figure 1 represents an equivalent non-uniform transmission line of length d, with varying characteristic impedance $Z(z)$ and propagation constant $\beta(z)$. The NTL is designed so that its *ABCD* parameters at a frequency f are equal to those of the uniform transmission line. Moreover, compactness is achieved by choosing the length d to be smaller than d_0.

The general method to design an optimal reduced-length NTLs proposed in [11] is adopted here. First, the NTL is subdivided into K uniform electrically short segments with length of Δz as follows:

$$\Delta z = \frac{d}{K} << \lambda = \frac{c}{f}. \quad (2)$$

The *ABCD* parameters of the whole NTL are obtained by multiplying the *ABCD* parameters of each section as follows:

$$\begin{bmatrix} A & B \\ C & D \end{bmatrix} = \begin{bmatrix} A_1 & B_1 \\ C_1 & D_1 \end{bmatrix} \cdots \begin{bmatrix} A_i & B_i \\ C_i & D_i \end{bmatrix} \cdots \begin{bmatrix} A_K & B_K \\ C_K & D_K \end{bmatrix}, \quad (3)$$

where the *ABCD* parameters of the i^{th} segment are:

$$A_i = D_i = \cos(\Delta\theta), \quad (4.a)$$

$$B_i = Z^2\left(\left(i-0.5\right)\Delta z\right) C_i = jZ\left(\left(i-0.5\right)\Delta z\right)\sin\left(\Delta\theta\right), \quad i = 1, 2, ..., K. \quad (4.b)$$

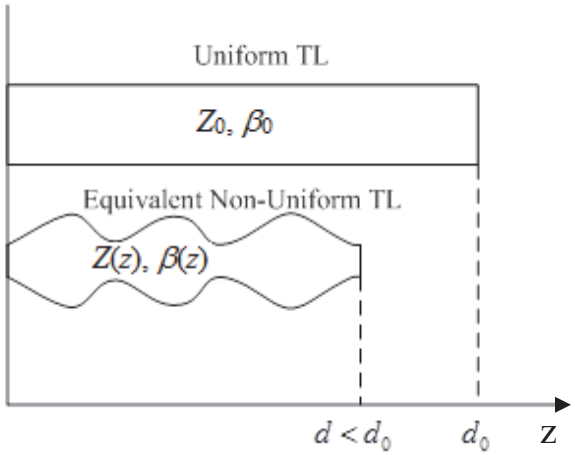

Fig. 1. A typical uniform transmission line (UTL) versus an equivalent non-uniform transmission line (NTL).

The electrical length of each segment is:

$$\Delta\theta = \frac{2\pi}{\lambda}\Delta z = \frac{2\pi}{c} f \sqrt{\varepsilon_{eff}}\,\Delta z. \quad (5)$$

Then, the following truncated Fourier series expansion for the normalized characteristic impedance $\overline{Z}(z) = Z(z)/Z_0$ is considered:

$$\ln\left(\overline{Z}(z)\right) = \sum_{n=0}^{N} C_n \cos\left(\frac{2\pi n z}{d}\right). \quad (6)$$

So, an optimum designed compact length NTL has to have the *ABCD* parameters as close as possible to the *ABCD* parameters of the desired uniform transmission line at a specific frequency. Therefore, the optimum values of the Fourier coefficients C_n's can be obtained through minimizing the following error function [11]:

$$Error = \sqrt{\frac{1}{4}\left(\left|A-A_0\right|^2 + Z_0^{-2}\left|B-B_0\right|^2 + Z_0^2\left|C-C_0\right|^2 + \left|D-D_0\right|^2\right)}. \quad (7)$$

Also, this error function should be restricted by some constraints such as reasonable fabrication and physical matching, as follows:

$$\overline{Z}_{\min} \le \overline{Z}(z) \le \overline{Z}_{\max}, \quad (8.a)$$

$$\overline{Z}(0) = \overline{Z}(d) = 1. \quad (8.b)$$

One should be careful when dealing with such constraints to get the desired performance. The first constraint given in (8.a) guarantees that the resulting non-uniform microstrip line is not too wide, by choosing an appropriate value of $\overline{Z}_{\min}$, and not too thin, by choosing an appropriate value of $\overline{Z}_{\max}$, since the microstrip line width is inversely proportional to its characteristic impedance. The second constraint given in (8.b) guarantees that the widths of the two ends of the resulting non-uniform transmission line will be equal to the width of the uniform ones for matching purposes, and for this constraint to be achieved, the sum of the Fourier coefficients must equal to zero. It is worth mentioning here that the Fourier coefficients are bounded between -1 and 1, i.e., $(-1 \le C_n \le 1)$.

So, the goal is to find the Fourier coefficients values (C_n's) that give a non-uniform transmission line that has its ABCD parameters approximately equal to those of the uniform transmission line by minimizing the error function in (7) at a specific design frequency (with the constraints given in (8)). To solve this constrained minimization problem, the MATLAB function "fmincon.m" is utilized.

III. DESIGN OF UNEQUAL SPLIT WPD

Figure 2 shows the schematic of the unequal split WPD that was proposed in [10]. This WPD topology has the merits of having a simple layout, with the dividing ratio k depending on the electrical lengths of its arms rather than the impedances values. In other words, the power-dividing ratio k is a function of ϕ (< π/2):

$$k = \frac{1}{\cos\phi} = \sqrt{\frac{P_2}{P_3}}. \qquad (9)$$

To achieve a 10:1 dividing ratio, one can obtain ϕ from (9) which gives ϕ=71.57°. So, for a 10:1 WPD operating at 1 GHz and having terminating impedances of Z_0= 50 Ω, the electrical lengths of the uniform transmission lines TL1, TL2 and TL3 are 161.57°, 90°, and 71.57°, respectively, and will share the same characteristic impedance of $\sqrt{2}Z_0 = 70.71\Omega$. For a design frequency of 1 GHz, and considering an FR-4 substrate having a dielectric constant ε_r of 4.6 and a substrate height h of 1.6 mm, the above electrical lengths can be translated into physical lengths of 74.35 mm, 41.41 mm, and 32.94 mm, for the first, second and third uniform transmission lines, respectively. These lengths occupy a large circuit area which will be reduced using NTLs in the next section.

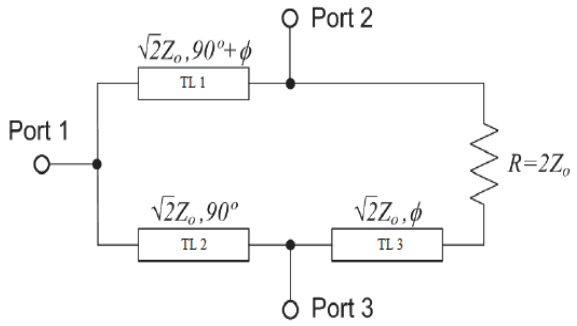

Fig. 2. An unequal split WPD proposed in [10].

IV. DESIGN OF COMPACT UNEQUAL SPLIT NTLs-WPD

An unequal split NTLs-WPD can be realized by substituting each uniform TL in Figure 2 by its equivalent NTL. So, for the uniform transmission line sections of lengths d_{01}= 74.35 mm, d_{02}= 41.41 mm and d_{03}= 32.94 mm, compact NTLs of lengths d_1= 50 mm, d_2= 28 mm, d_3= 25 mm, respectively, have been chosen. The optimization variables K and N are chosen as 50 and 10, respectively. Also, $Z_1(z)$ is bounded between $(0.216 \le \overline{Z}_1(z) \le 1.8)$, whereas $Z_2(z)$ is bounded between $(0.216 \le \overline{Z}_2(z) \le 1.7)$ and $Z_3(z)$ is bounded between $(0.216 \le \overline{Z}_3(z) \le 1.7)$. Figure 3 shows the resulting impedances $\overline{Z}_1(z)$, $\overline{Z}_2(z)$, and $\overline{Z}_3(z)$. The obtained impedances shown in Figure 3 are translated into microstrip line widths variation, as presented in Figure 4. This figure shows that the NTL sections widths are bounded as follows:

$$(0.300\ mm \le W_1(z) \le 15.2\ mm)$$

$$(0.368\ mm \le W_2(z) \le 15.4\ mm)$$

$$(0.335\ mm \le W_3(z) \le 15.2\ mm)$$

Also, the resulting Fourier coefficients and the error values are listed in Table 1.

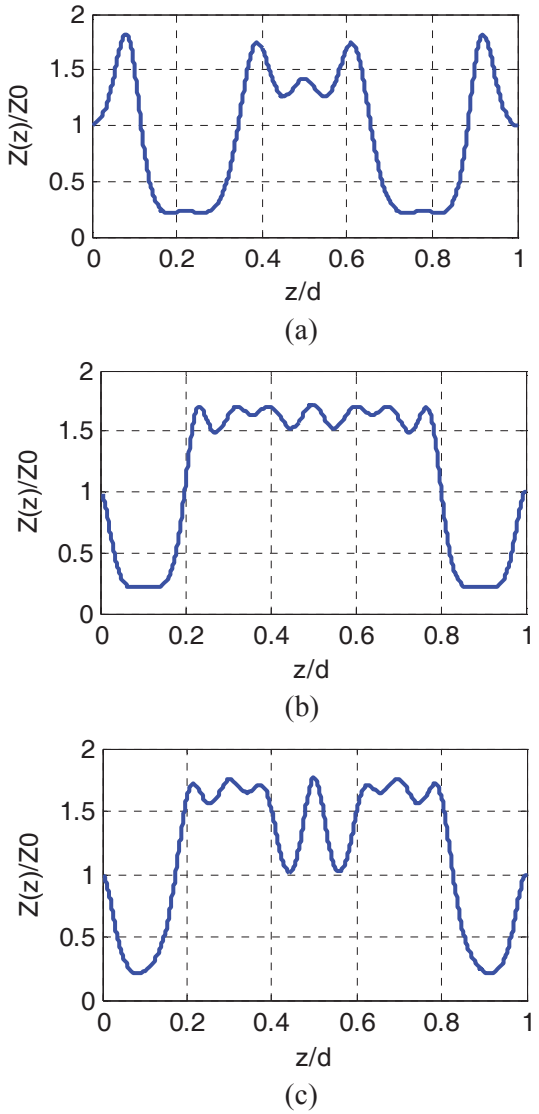

Fig. 3. The normalized impedances for (a) $\overline{Z}_1(z)$, (b) $\overline{Z}_2(z)$, and (c) $\overline{Z}_3(z)$.

For comparison purposes, Figure 5 represents the layout of the conventional 10:1 WPD along with the layout of the proposed NTLs 10:1 WPD. A size reduction of almost 33% is achieved with the use of the NTLs.

V. SIMULATIONS AND MEASURMENTS

The designed 10:1 NTLs-WPD, is first, analyzed using Ansoft Designer [16] (circuit model) by dividing the NTL arms into very short uniform microstrip lines (i.e., a stepped structure

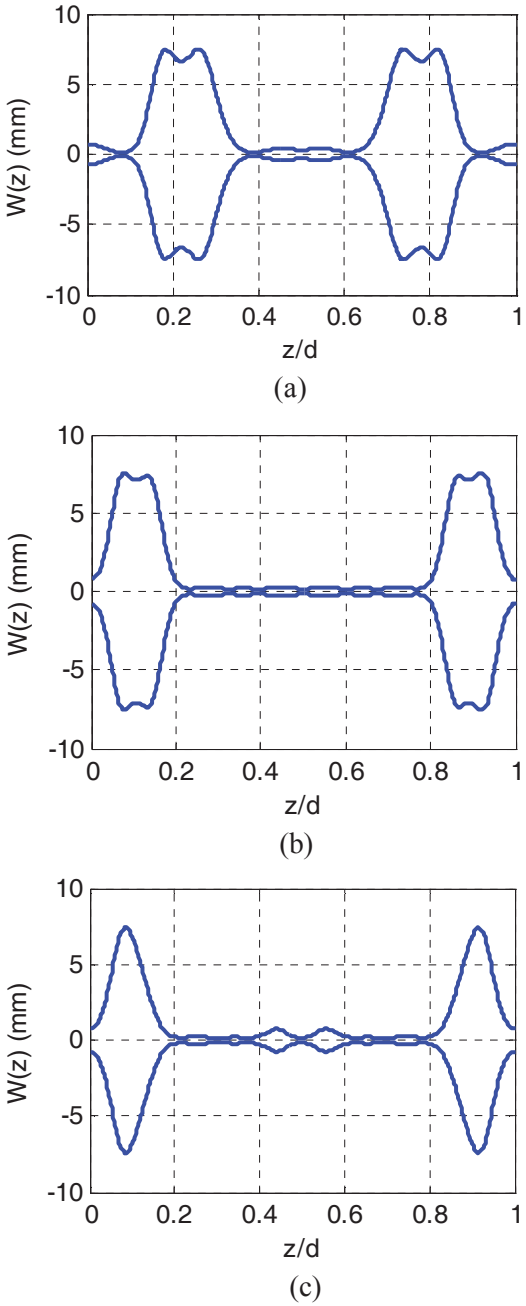

Fig. 4. The variation of the microstrip widths for (a) $W_1(z)$, (b) $W_2(z)$, and (c) $W_3(z)$.

with piecewise constant impedance segments). Then, the designed WPD (using the smooth structure as is) is simulated using the full-wave simulators HFSS [16], and IE3D [17]. Moreover, the NTLs-WPD is fabricated and measured using an Anritsu 37369C network analyzer.

Table 1: The values of the Fourier coefficients for the optimized NTL sections

C_n's	C_0	C_1	C_2	C_3	C_4	C_5	C_6	C_7	C_8	C_9	C_{10}	Error in eq. 7
1st section l_1= 50 mm	**-0.3447**	**-0.2034**	**0.9778**	**0.2848**	**-0.3878**	**-0.0880**	**-0.1722**	**-0.2208**	**0.0562**	**0.0516**	**0.0467**	**$1x10^{-6}$**
2nd section l_2= 28 mm	**-0.1423**	**-0.9494**	**-0.2587**	**0.3139**	**0.4395**	**0.2683**	**0.0491**	**-0.0320**	**0.0737**	**0.1285**	**0.1092**	**$2.6x10^{-7}$**
3rd section l_3= 25 mm	**-0.0419**	**-0.7070**	**-0.4296**	**0.1486**	**0.3324**	**0.3002**	**0.2542**	**-0.0035**	**0.0761**	**-0.0224**	**0.0928**	**$8x10^{-8}$**

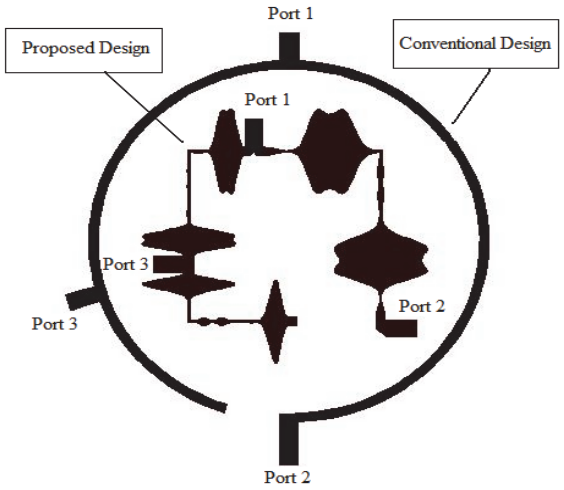

Fig. 5. The conventional WPD layout vs. the proposed NTLs-WPD layout. The 100Ω lumped resistor is not shown in this layout.

Figures 6-8 show the matching parameters at the input/output ports: S_{11}, S_{22}, and S_{33}, respectively. Ansoft Designer result shows that the input port matching S_{11} is around -37; meanwhile, S_{11} obtained using IE3D and HFSS equals -33 dB around the design frequency. The measured matching parameter S_{11} is -27 dB around 0.94 GHz.

Figures 7 and 8 show good matching at the output ports which is below -20 dB at the design frequency. The measurement results equal -28 dB around 0.9 GHz and -18.5 dB at 0.85 GHz for S_{22} and S_{33}, respectively. The differences between the experimental results and the simulation ones could be due to the use of carbon resistor, as well as fabrication process, soldering, and measurement errors. Figure 9 shows the isolation parameter S_{23}. The simulation and measurement results for S_{23} are accepted at the design frequency.

Figures 10 and 11 show the transmission parameters S_{21} and S_{31}, respectively. As expected, Ansoft Designer results are very close to the ideal ones, i.e., S_{21} close to -0.41 dB and S_{31} close to -10.41 dB at the design frequency. Full-wave simulation results and experimental ones are in good agreement, and show an acceptable behavior around the design frequency (keeping in mind that the loss tangent of the FR-4 substrate used in our design is 0.02).

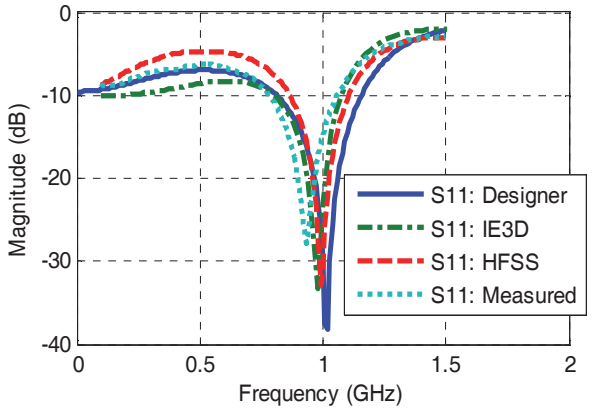

Fig. 6. Matching parameter at port 1.

To demonstrate the odd harmonics suppression for the designed 10:1 NTLs-WPD, Figure 12 shows the frequency response for the proposed NTLs-WPD along with those for the conventional UTL-WPD, in a wider frequency range. It is clearly seen that using the NTLs suppresses the first odd harmonic at 3 GHz. It is worth to point out here that, as shown in Fig.

12(a), the proposed NTLs divider operating bandwidth is narrower than that of the conventional one. Using IE3D results in Fig. 12(a), the 10-dB return loss fractional bandwidth of the proposed divider is about 27.3%, whereas the fractional bandwidth of the conventional one is 97.6%. Thus, the advantages of reducing the overall circuitry area and suppressing the odd harmonics are at the expense of reducing the operating bandwidth. It should be also mentioned that the power handling capability of microstrip lines is restricted by heating caused by ohmic and dielectric losses as well as dielectric breakdown [18]. Step in width, bends, and other discontinuities cause also local concentration of current and thus increase the temperature and decrease the power handling capability. Therefore, it is expected, as given in eq. (10) in [18], that the narrow line width reduces the power handling capability of the structure. On the other hand, the ohmic and dielectric losses depend also on the line length. Since the narrow width sections used in the proposed structure are of limited lengths and the overall structure is small in size with respect to the conventional one, the reduction in power handling capability may not be significant. Figure 13 shows the photograph of the fabricated 10:1 reduced size WPD.

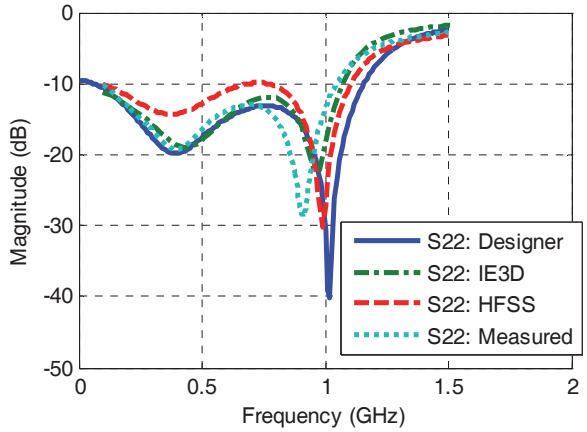

Fig. 7. Matching parameter at port 2.

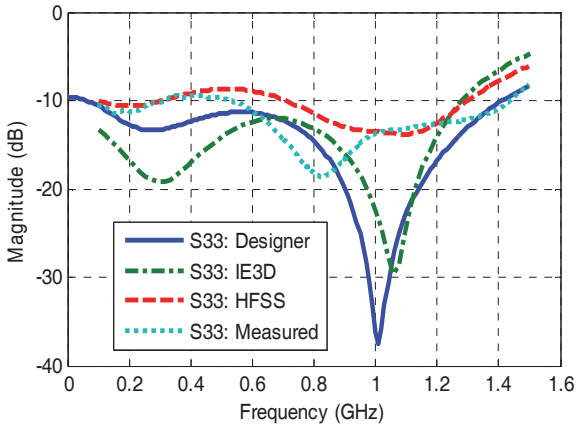

Fig. 8. Matching parameter at port 3.

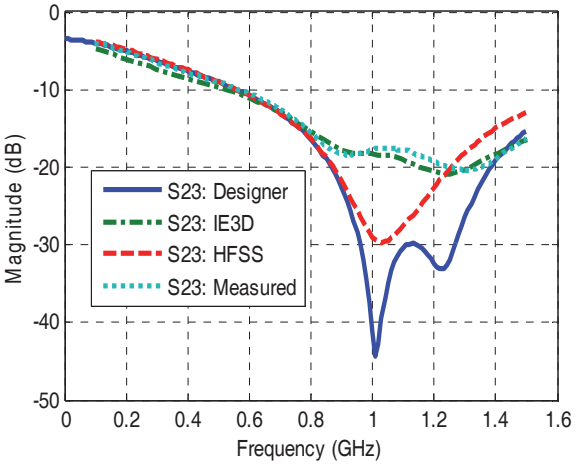

Fig. 9. Isolation parameter S_{23}.

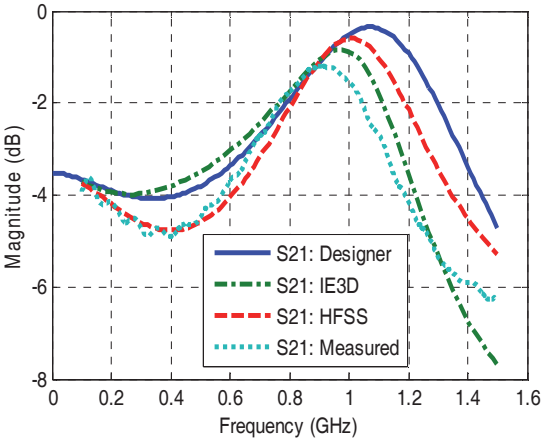

Fig. 10. Transmission parameter S_{21}.

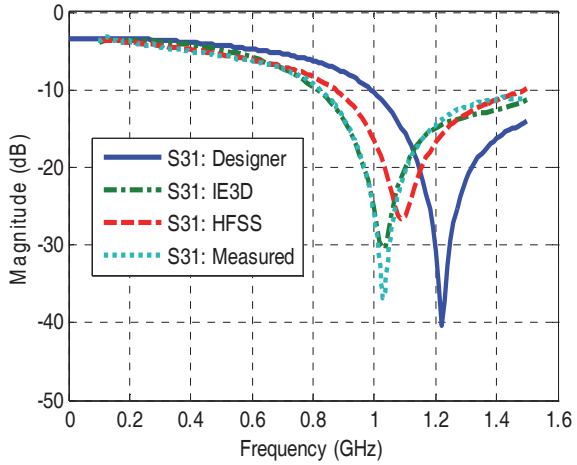

Fig. 11. Transmission parameter S_{31}.

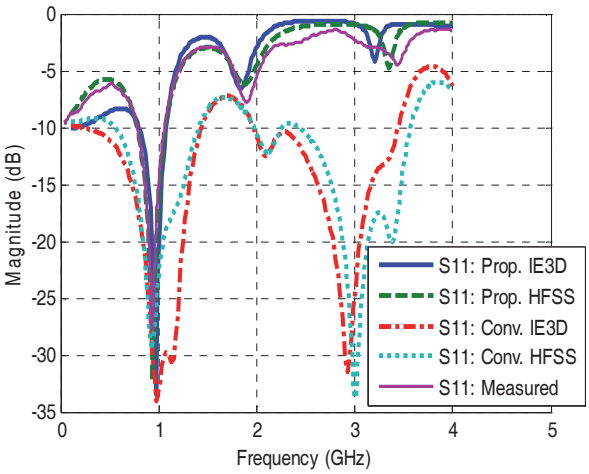

(a)

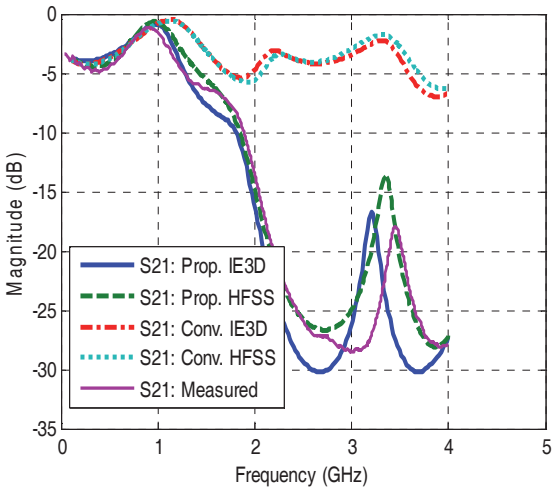

(b)

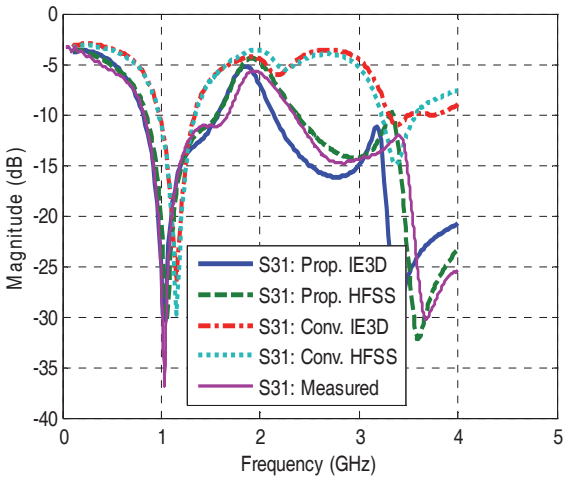

(c)

Fig. 12. Demonstration of odd harmonics suppression (a) S_{11}, (b) S_{21}, (c) S_{31}.

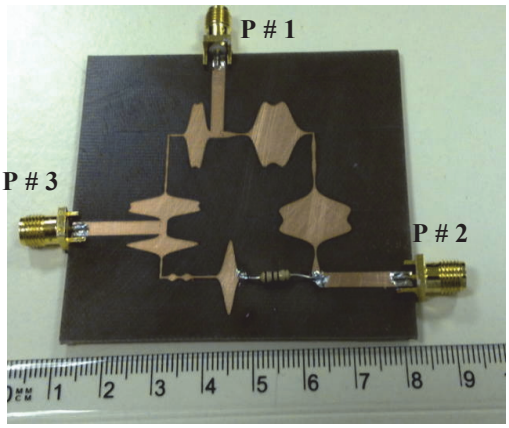

Fig. 13. A photograph of the fabricated 10:1 WPD.

VI. CONCLUSIONS

Based on the theory of non-uniform transmission lines, a compact WPD with a 10:1 split ratio was designed and fabricated. This WPD achieved a size reduction of almost 33% compared to the conventional UTL-WPD. Moreover, the designed WPD suppresses the odd harmonics of the design frequency by enforcing the *ABCD* parameters of the optimized NTLs to be equal to those of the uniform ones at the design frequency only. The agreement between the simulation and experimental results is acceptable, which validates the design procedure.

REFERENCES

[1] J. Lim, C. Kim, J. Park, D. Ahn, and S. Nam, "Design of 10 dB 90^0 Branch Line Coupler Using Microstrip Line with Defected Ground Structure", *Electronics Letters*, vol. 36 (21), pp. 1784-1785, 2000.

[2] J. Lim, G. Lee, Y. Jeon, D. Ahn, and K. Choi, "A 1:6 Unequal Wilkinson Power Divider", *36th European Microwave Conference*, Manchester U.K., pp. 200-203, September 2006.

[3] C. Kim, J. Park, D. Ahn, and J. Lim, "A Novel 1-D Periodic Defected Ground Structure for Planar Circuits", *IEEE Microwave and Guided Wave Letters*, vol. 10, pp. 131–133, 2000.

[4] D. Schlieter, and R. Henderson, "An Etched Ground GCPW 7:1 Unequal Wilkinson Power Divider", *IEEE Radio and Wireless Symposium, RWS '09*, pp. 256-259, 2009.

[5] C. Kim, J. Lim, J. Park, D. Ahn, and S. Nam, "A 10 dB Branch Line Coupler Using Defected Ground Structure", *in Proc. EUMC 2000*, vol. 3, pp. 68–71, 2000.

[6] Y. Sung, C. Ahn, and Y. Kim, "Branch-Line Coupler Using Defected Ground Structure", *IEICE transactions on Communications*, E88-B(4), pp. 1665-1667, 2005.

[7] M. Moradian and H. Oriazi, "Application of Grooved Substrates for Design of Unequal Wilkinson Power Dividers", *Electronics Letters*, vol. 44(1), pp. 1784-1785, 2008.

[8] Y. Ko, J. Park, and J. Bu, "Fully Integrated Unequal Wilkinson Power Divider With EBG CPW", *IEEE Microwave and Wireless Components Letters*, vol. 13(7), pp. 276-278, 2003.

[9] B. Li, X. Wu, and W. Wu, "A 10:1 Unequal Wilkinson Power Divider Using Coupled Lines With Two Shorts", *IEEE Microwave and Wireless Components Letters*, vol. 19(12), pp. 789-791, 2009.

[10] K. –K. M. Cheng, and P. –W. Li, "A Novel Power-Divider Design With Unequal Power-Dividing Ratio and Simple Layout", *IEEE transactions on microwave theory and techniques*, vol. 57(6), pp. 1589-1594, 2009.

[11] M. Khalaj-Amirhosseini, "Non-uniform Transmission Lines As Compact Uniform Transmission Lines", *Progress In Electromagnetics Research C*, vol. 4, pp. 205-211, 2008.

[12] K. A. Shamaileh and N. Dib, "Design of Compact Dual-Frequency Wilkinson Power Divider Using Non-Uniform Transmission Lines", *Progress In Electromagnetics Research C*, vol. 19, pp. 37-46, 2011.

[13] K. Shamaileh, A. Qaroot, and N. Dib, "Non-Uniform Transmission Line Transformers and their Application in the Design of Compact Multi-Band Bagley Power Dividers with Harmonics Suppression", *Progress In Electromagnetics Research*, vol. 113, pp. 269-284, 2011.

[14] J. Izydorczyk, "Equivalent Circuits for Nonuniform Transmission Line Simulation", *Applied Computational Electromagnetics Society (ACES) Journal*, vol. 25(9), pp. 764-779, 2010.

[15] D. M. Pozar, Microwave Engineering. New York: Wiley, 3rd edition.

[16] Ansoft Corporation, www.ansoft.com

[17] www.zeland.com , 2006.

[18] I. J. Bahl and K. C. Gupta, "Average power-handling capability of microstrip lines," *IEEE Proc.H., Microwave, Optics, Acoustics*, vol. 3, pp. 1–4, 1979.

Khair Ayman Al Shamaileh received his B.Sc. in Communications and Electronics Engineering from Jordan University of Science and Technology (JUST), Irbid, Jordan in 2009. In the same year, he joined the Master program in the Electrical Engineering Department at JUST majoring in Wireless Communications. He received his M. Sc. degree in 2011.

His research interests include the analysis and design of compact, planar, passive, and multi-frequency and ultra- wideband microwave components for wireless applications.

Abdullah Mazen Qaroot is a lecturer of Electrical Engineering at King Faisal University, Al-Ahsa, Saudi Arabia. Mr. Qaroot obtained his B.Sc. degree in Communications and

Electronics Engineering with highest honors from the University of Philadelphia, Amman- Jordan in 2008. He got his M. Sc. degree in Electrical Engineering /Wireless Communications from Jordan University of Science and Technology (JUST), Irbid in 2010. His research interests include Microwave circuits, Antennas, and Applied Electromagnetics.

Nihad I. Dib obtained his B. Sc. and M.Sc. in Electrical Engineering from Kuwait University in 1985 and 1987, respectively. He obtained his Ph.D. in EE (major in Electromagnetics and Microwaves) in 1992 from University of Michigan, Ann Arbor. Then, he worked as an assistant research scientist in the radiation laboratory at the same school. In Sep. 1995, he joined the EE department at Jordan University of Science and Technology (JUST) as an assistant professor, and became a full professor in Aug. 2006. His research interests are in computational electromagnetics, antennas and modeling of planar microwave circuits.

Abdel Fattah Sheta graduated from the Communications and Electro-Physics Dept., Alexandria University, Egypt in 1985. He received the M.Sc. degree in the Electrical Engineering Department, Cairo University, in 1991. In 1996, he received the Ph.D degree in microwave circuits analysis and design from ENST, Université de Bretagne Occidentale, France. During 1996-1998, he worked as a researcher in the National Telecommunication Institute, Cairo, Egypt. In 1998, he joined Electrical Engineering Department, Fayoum University. Currently, Dr. Sheta is a full professor at EE Department, King Saud University, Saudi Arabia. His current research interests include reconfigurable RF systems, UWB systems, microstrip antennas, microstrip filters, and planar and uniplanar MIC's and MMIC's.

2011 INSTITUTIONAL MEMBERS

DTIC-OCP LIBRARY
8725 John J. Kingman Rd, Ste 0944
Fort Belvoir, VA 22060-6218

AUSTRALIAN DEFENCE LIBRARY
Northcott Drive
Canberra, A.C.T. 2600 Australia

BEIJING BOOK CO, INC
701 E Linden Avenue
Linden, NJ 07036-2495

DARTMOUTH COLLEGE
6025 Baker/Berry Library
Hanover, NH 03755-3560

DSTO EDINBURGH
AU/33851-AP, PO Box 830470
Birmingham, AL 35283

SIMEON J. EARL – BAE SYSTEMS
W432A, Warton Aerodome
Preston, Lancs., UK PR4 1AX

ENGINEERING INFORMATION, INC
PO Box 543
Amsterdam, Netherlands 1000 Am

ETSE TELECOMUNICACION
Biblioteca, Campus Lagoas
Vigo, 36200 Spain

GA INSTITUTE OF TECHNOLOGY
EBS-Lib Mail code 0900
74 Cherry Street
Atlanta, GA 30332

TIMOTHY HOLZHEIMER
Raytheon
PO Box 1044
Rockwall, TX 75087

HRL LABS, RESEARCH LIBRARY
3011 Malibu Canyon
Malibu, CA 90265

IEE INSPEC
Michael Faraday House
6 Hills Way
Stevenage, Herts UK SG1 2AY

INSTITUTE FOR SCIENTIFIC INFO.
Publication Processing Dept.
3501 Market St.
Philadelphia, PA 19104-3302

LIBRARY – DRDC OTTAWA
3701 Carling Avenue
Ottawa, Ontario, Canada K1A OZ4

LIBRARY of CONGRESS
Reg. Of Copyrights
Attn: 407 Deposits
Washington DC, 20559

LINDA HALL LIBRARY
5109 Cherry Street
Kansas City, MO 64110-2498

MISSOURI S&T
400 W 14th Street
Rolla, MO 56409

MIT LINCOLN LABORATORY
Periodicals Library
244 Wood Street
Lexington, MA 02420

NATIONAL CHI NAN UNIVERSITY
Lily Journal & Book Co, Ltd
20920 Glenbrook Drive
Walnut, CA 91789-3809

JOHN NORGARD
UCCS
20340 Pine Shadow Drive
Colorado Springs, CO 80908

OSAMA MOHAMMED
Florida International University
10555 W Flagler Street
Miami, FL 33174

NAVAL POSTGRADUATE SCHOOL
Attn:J. Rozdal/411 Dyer Rd./ Rm 111
Monterey, CA 93943-5101

NDL KAGAKU
C/0 KWE-ACCESS
PO Box 300613 (JFK A/P)
Jamaica, NY 11430-0613

OVIEDO LIBRARY
PO BOX 830679
Birmingham, AL 35283

DAVID PAULSEN
E3Compliance
1523 North Joe Wilson Road
Cedr Hill, TX 75104-1437

PENN STATE UNIVERSITY
126 Paterno Library
University Park, PA 16802-1808

DAVID J. PINION
1122 E Pike Street #1217
SEATTLE, WA 98122

KATHERINE SIAKAVARA
Gymnasiou 8
Thessaloniki, Greece 55236

SWETS INFORMATION SERVICES
160 Ninth Avenue, Suite A
Runnemede, NJ 08078

YUTAKA TANGE
Maizuru Natl College of Technology
234 Shiroya
Maizuru, Kyoto, Japan 625-8511

TIB & UNIV. BIB. HANNOVER
DE/5100/G1/0001
Welfengarten 1B
Hannover, Germany 30167

UEKAE
PO Box 830470
Birmingham, AL 35283

UNIV OF CENTRAL FLORIDA
4000 Central Florida Boulevard
Orlando, FL 32816-8005

UNIVERSITY OF COLORADO
1720 Pleasant Street, 184 UCB
Boulder, CO 80309-0184

UNIVERSITY OF KANSAS – WATSON
1425 Jayhawk Blvd 210S
Lawrence, KS 66045-7594

UNIVERSITY OF MISSISSIPPI
JD Williams Library
University, MS 38677-1848

UNIVERSITY LIBRARY/HKUST
Clear Water Bay Road
Kowloon, Honk Kong

CHUAN CHENG WANG
8F, No. 31, Lane 546
MingCheng 2nd Road, Zuoying Dist
Kaoshiung City, Taiwan 813

THOMAS WEILAND
TU Darmstadt
Schlossgartenstrasse 8
Darmstadt, Hessen, Germany 64289

STEVEN WEISS
US Army Research Lab
2800 Powder Mill Road
Adelphi, MD 20783

YOSHIHIDE YAMADA
NATIONAL DEFENSE ACADEMY
1-10-20 Hashirimizu
Yokosuka, Kanagawa,
Japan 239-8686

APPLIED COMPUTATIONAL ELECTROMAGNETICS SOCIETY JOURNAL
http://aces.ee.olemiss.edu

INFORMATION FOR AUTHORS

PUBLICATION CRITERIA

Each paper is required to manifest some relation to applied computational electromagnetics. **Papers may address general issues in applied computational electromagnetics, or they may focus on specific applications, techniques, codes, or computational issues.** While the following list is not exhaustive, each paper will generally relate to at least one of these areas:

1. **Code validation.** This is done using internal checks or experimental, analytical or other computational data. Measured data of potential utility to code validation efforts will also be considered for publication.

2. **Code performance analysis.** This usually involves identification of numerical accuracy or other limitations, solution convergence, numerical and physical modeling error, and parameter tradeoffs. However, it is also permissible to address issues such as ease-of-use, set-up time, run time, special outputs, or other special features.

3. **Computational studies of basic physics.** This involves using a code, algorithm, or computational technique to simulate reality in such a way that better, or new physical insight or understanding, is achieved.

4. **New computational techniques** or new applications for existing computational techniques or codes.

5. **"Tricks of the trade"** in selecting and applying codes and techniques.

6. **New codes, algorithms, code enhancement, and code fixes.** This category is self-explanatory, but includes significant changes to existing codes, such as applicability extensions, algorithm optimization, problem correction, limitation removal, or other performance improvement. **Note: Code (or algorithm) capability descriptions are not acceptable, unless they contain sufficient technical material to justify consideration.**

7. **Code input/output issues.** This normally involves innovations in input (such as input geometry standardization, automatic mesh generation, or computer-aided design) or in output (whether it be tabular, graphical, statistical, Fourier-transformed, or otherwise signal-processed). Material dealing with input/output database management, output interpretation, or other input/output issues will also be considered for publication.

8. **Computer hardware issues.** This is the category for analysis of hardware capabilities and limitations of various types of electromagnetics computational requirements. Vector and parallel computational techniques and implementation are of particular interest.

Applications of interest include, but are not limited to, antennas (and their electromagnetic environments), networks, static fields, radar cross section, inverse scattering, shielding, radiation hazards, biological effects, biomedical applications, electromagnetic pulse (EMP), electromagnetic interference (EMI), electromagnetic compatibility (EMC), power transmission, charge transport, dielectric, magnetic and nonlinear materials, microwave components, MEMS, RFID, and MMIC technologies, remote sensing and geometrical and physical optics, radar and communications systems, sensors, fiber optics, plasmas, particle accelerators, generators and motors, electromagnetic wave propagation, non-destructive evaluation, eddy currents, and inverse scattering.

Techniques of interest include but not limited to frequency-domain and time-domain techniques, integral equation and differential equation techniques, diffraction theories, physical and geometrical optics, method of moments, finite differences and finite element techniques, transmission line method, modal expansions, perturbation methods, and hybrid methods.

Where possible and appropriate, authors are required to provide statements of quantitative accuracy for measured and/or computed data. This issue is discussed in "Accuracy & Publication: Requiring, quantitative accuracy statements to accompany data," by E. K. Miller, *ACES Newsletter*, Vol. 9, No. 3, pp. 23-29, 1994, ISBN 1056-9170.

SUBMITTAL PROCEDURE

All submissions should be uploaded to ACES server through ACES web site (http://aces.ee.olemiss.edu) by using the upload button, journal section. Only pdf files are accepted for submission. The file size should not be larger than 5MB, otherwise permission from the Editor-in-Chief should be obtained first. Automated acknowledgment of the electronic submission, after the upload process is successfully completed, will be sent to the corresponding author only. It is the responsibility of the corresponding author to keep the remaining authors, if applicable, informed. Email submission is not accepted and will not be processed.

EDITORIAL REVIEW

In order to ensure an appropriate level of quality control, papers are peer reviewed. They are reviewed both for technical correctness and for adherence to the listed guidelines regarding information content and format.

PAPER FORMAT

Only camera-ready electronic files are accepted for publication. The term **"camera-ready" means that the material is neat, legible, reproducible, and in accordance with the final version format listed below.**

The following requirements are in effect for the final version of an ACES Journal paper:

1. The paper title should not be placed on a separate page.

The title, author(s), abstract, and (space permitting) beginning of the paper itself should all be on the first page. The title, author(s), and author affiliations should be centered (center-justified) on the first page. The title should be of font size 16 and bolded, the author names should be of font size 12 and bolded, and the author affiliation should be of font size 12 (regular font, neither italic nor bolded).

2. An abstract is required. The abstract should be a brief summary of the work described in the paper. It should state the computer codes, computational techniques, and applications discussed in the paper (as applicable) and should otherwise be usable by technical abstracting and indexing services. The word "Abstract" has to be placed at the left margin of the paper, and should be bolded and italic. It also should be followed by a hyphen (—) with the main text of the abstract starting on the same line.

3. All section titles have to be centered and all the title letters should be written in caps. The section titles need to be numbered using roman numbering (I. II. ….)

4. Either British English or American English spellings may be used, provided that each word is spelled consistently throughout the paper.

5. Internal consistency of references format should be maintained. As a guideline for authors, we recommend that references be given using numerical numbering in the body of the paper (with numerical listing of all references at the end of the paper). The first letter of the authors' first name should be listed followed by a period, which in turn, followed by the authors' complete last name. Use a coma (,) to separate between the authors' names. Titles of papers or articles should be in quotation marks (" "), followed by the title of journal, which should be in italic font. The journal volume (vol.), issue number (no.), page numbering (pp.), month and year of publication should come after the journal title in the sequence listed here.

6. Internal consistency shall also be maintained for other elements of style, such as equation numbering. Equation numbers should be placed in parentheses at the right column margin. All symbols in any equation have to be defined before the equation appears or right immediately following the equation.

7. The use of SI units is strongly encouraged. English units may be used as secondary units (in parentheses).

8. Figures and tables should be formatted appropriately (centered within the column, side-by-side, etc.) on the page such that the presented data appears close to and after it is being referenced in the text. When including figures and tables, all care should be taken so that they will appear appropriately when printed in black and white. For better visibility of paper on computer screen, it is good to make color figures with different line styles for figures with multiple curves. Colors should also be tested to insure their ability to be distinguished after black and white printing. Avoid the use of large symbols with curves in a figure. It is always better to use different line styles such as solid, dotted, dashed, etc.

9. A figure caption should be located directly beneath the corresponding figure, and should be fully justified.

10. The intent and meaning of all text must be clear. For authors who are not masters of the English language, the ACES Editorial Staff will provide assistance with grammar (subject to clarity of intent and meaning). However, this may delay the scheduled publication date.

11. Unused space should be minimized. Sections and subsections should not normally begin on a new page.

ACES reserves the right to edit any uploaded material, however, this is not generally done. It is the author(s) responsibility to provide acceptable camera-ready files in pdf and MSWord formats. Incompatible or incomplete files will not be processed for publication, and authors will be requested to re-upload a revised acceptable version.

COPYRIGHTS AND RELEASES

Each primary author must execute the online copyright form and obtain a release from his/her organization vesting the copyright with ACES. Both the author(s) and affiliated organization(s) are allowed to use the copyrighted material freely for their own private purposes.

Permission is granted to quote short passages and reproduce figures and tables from and ACES Journal issue provided the source is cited. Copies of ACES Journal articles may be made in accordance with usage permitted by Sections 107 or 108 of the U.S. Copyright Law. This consent does not extend to other kinds of copying, such as for general distribution, for advertising or promotional purposes, for creating new collective works, or for resale. The reproduction of multiple copies and the use of articles or extracts for commercial purposes require the consent of the author and specific permission from ACES. Institutional members are allowed to copy any ACES Journal issue for their internal distribution only.

PUBLICATION CHARGES

All authors are allowed for 8 printed pages per paper without charge. Mandatory page charges of $75 a page apply to all pages in excess of 8 printed pages. Authors are entitled to one, free of charge, copy of the printed journal issue in which their paper was published. Additional reprints are available for $ 50. Requests for additional re-prints should be submitted to the managing editor or ACES Secretary.

Corresponding author is required to complete the online form for the over page charge payment right after the initial acceptance of the paper is conveyed to the corresponding author by email.

ACES Journal is abstracted in INSPEC, in Engineering Index, DTIC, Science Citation Index Expanded, the Research Alert, and to Current Contents/Engineering, Computing & Technology.